Title

Ceramic Packaging for Wireless Implantable Medical Devices

Author

Shen, Konlin

Publication Date

2020

Peer reviewed|Thesis/dissertation

Ceramic Packaging for Wireless Implantable Medical Devices

by

Konlin Shen

A dissertation submitted in partial satisfaction of the

requirements for the degree of

Joint Doctor of Philosophy
with University of California, San Francisco

in

Bioengineering

in the

Graduate Division

of the

University of California, Berkeley

Committee in charge:

Professor Michel M. Maharbiz, Chair
Professor Jose M. Carmena
Professor Chris J. Diederich
Professor Kristofer S. J. Pister

Spring 2020

Ceramic Packaging for Wireless Implantable Medical Devices

Abstract

Ceramic Packaging for Wireless Implantable Medical Devices

by

Konlin Shen

Doctor of Philosophy in Bioengineering

University of California, Berkeley

Professor Michel M. Maharbiz, Chair

Implantable medical devices have tremendous therapeutic potential for both treatment of disease states as well as monitoring for preventative care. To be effective, implants must perturb host tissue as minimally as possible, while simultaneously being able to withstand the tissue environment for a significant portion of a patient's life. Advances in wireless power transfer technology have made it possible to implant millimeter to sub-millimeter scale devices fully within the body, but these devices have not been demonstrated to work for decadal time spans.

Typical packaging material for medical implants are polymers such as silicone or parylene, or titanium. However, polymers are not chronically hermetic due to their high water vapor permeability and titanium is not easily amenable to electromagnetics-based wireless communication. Ceramic materials, however, have a low water vapor permeability and are transparent to radio-frequency radiation. Furthermore, they have had a long history in medical implants and semiconductor processing methods have greatly increased the compatibility of ceramics processing with other materials.

This thesis explores the use of ceramics as packaging materials for wireless, miniaturized, implantable medical devices. An alumina-titanium hybrid package is first demonstrated for a millimeter-scale ultrasonically-coupled wireless implant. Sound propagation through solids in two different modes is investigated, test packages are assembled, and performance is evaluated. Next, silicon carbide is explored as a potential packaging material for wireless radio-frequency identification tags. A system for rapidly testing and aging silicon carbide thin-films is designed and demonstrated, and progress towards building chronic silicon-carbide encapsulated radio-frequency identification tags is shown.

To my family

Contents

List of Figures

List of Tables

Acknowledgments

First and foremost, I am indebted my adviser, Prof. Michel M. Maharbiz, whose support and guidance have been invaluable to my growth as a researcher. Michel's mentorship has allowed me to explore my interests and become independent without losing sight of the big picture.

I am extremely grateful for the opportunity to work in the Maharbiz lab, in which I worked alongside many amazing individuals. My labmates have been a constant source of friendship, inspiration, advice, and light. Dr. Dongjin (DJ) Seo and Dr. Travis Massey, mentored me during my early years as a grad student and always seemed to have the answers to whatever technical problems I encountered. I owe them tremendously for all the lab skills they have taught me. I had a lot of fun collaborating with David Piech and Dr. Soner Sonmezoglu, who are not only great to work with, but are also extremely inspiring in their scientific rigor and dedication. Oliver Chen, Mauricio Bustamante, and Jordan Edmunds were frequently my Nanolab buddies during late nights and weekends. I thank Dr. Tom Zajdel, Dr. Amy Liao, and Dr. Monica Lin for helping me find my bearings in the lab when I was starting out and their continued advice throughout the years. Dr. Camilo Diaz-Botia and Dr. Bochao Lu taught me a great deal about silicon carbide and germanium processing respectively, and much of the work done in Chapter 6 of this thesis was based off the work done by Camilo. Alyssa Zhou and Kyoungtae Lee were my go-to circuits experts whenever I had questions. I thank the rest of the Maharbiz group: Dr. Maysam Chamanzar, Dr. Tim Hanson, Dr. Wei Li, Arda Ozilgen, and Wentian Mi for making the lab a great place to work in. I treasure all the great conversations and experiences we've had together; hats off to Soner for putting up with all the banter Oliver and I made in our shared cubicle.

Being at Berkeley allowed me to meet, work with, and learn from many amazing individuals outside of the Maharbiz group. I would like to thank Dr. Gabriel Dunn from the Zettl group whom I collaborated with on investigating carbon nanotubes as electrodes for a neural probe; Dr. Alison Walker and Dr. Ben Sorum from the Miller lab and Brohawn lab, respectively, for helping me and working with me while we explored the acoustic properties of neurons and nerves; Dr. Benjamin Johnson and Meraj Ghanbari of the Muller lab and Dr. Ryan Neely of the Carmena lab, who collaborated with me on Neural Dust and Stim Dust projects; Gabriele Lodi, who worked with me to develop a process for putting gold bumps on singulated ASICs; and Kyrollos Yanny of the Waller group, who gave me the opportunity to help build test samples for a head-mounted fluorescence microscope.

I was also fortunate to work with several talented undergraduate researchers: Tran Nguyen, Kiely Smith, Saarang Panchavati, Annabel Yau, and Averal Kandala. Saarang and Annabel helped tremendously with the work presented in this thesis. I thank them for their patience, dedication, and excellent work.

I want to thank my crewmates: Rahul Doraiswami, Laura Freeman, Louis Li, Lou Lin, and Yuyang Mei. Their support, encouragement, and friendship helped me keep my sanity during my PhD.

Most importantly, I would like to thank my family. My mother, FenAnn, raised me and instilled in me the importance of education, hard work, and perseverance. My father, Tsung-Cheng, is my earliest role-model and his curiosity and insatiable appetite for science taught me how to ask the right questions and stay hopeful, even when nothing seems to be working. Finally, I am most indebted to my sister, Koning, whose footsteps I have followed since we were kids. She has provided me with endless support and advice, both in academia and out. My family provided me with tremendous support through my PhD and none of this would have been possible without them.

Chapter 1

Packaging Implantable Medical Devices

1.1 Implantable medical devices

We are often told to "listen to our bodies", but very rarely do we hear, much less are we able to translate, what our bodies have to say into actionable tasks. The ability to interface with the body, then, would provide tremendous therapeutic benefit. Since the invention of the pacemaker in 1958, enormous strides have been made in developing implantable medical devices. Neuromodulatory devices, for example, promise to treat a wide range of conditions ranging from motor dysfunction (Parkinsonian tremor, tetraplegia, Meige syndrome, etc.), to psychiatric disorders (depression, OCD, etc.) [26, 142], to peripheral nerve applications [145, 14, 16, 130] and more. Bidirectional implants allow for continuous monitoring and modulation of organ targets, such that preventative actions can be taken to slow or even halt the progression of disease [48, 116, 110]. Commercial efforts to deploy these types of interventions through the use of implantable medical devices (IMDs)[1] is growing rapidly; an oft-cited estimate shows that the neuromodulation device industry was valued at 8.4 billion dollars in 2018 and is expected to grow to 13.3 billion dollars by 2022 [20].

1.2 Challenges for chronic clinical implants

Despite the market enthusiasm behind IMDs, clinical translation of IMDs is still rather slow. Part of this can be attributed to the relatively short lifetime (on the order of years)

A part of this chapter is adapted from an unpublished manuscript: "Ceramic Packaging for Neural Implants" by K. Shen and M. M. Maharbiz

[1] Often a distinction is made between passive IMDs and *active* IMDs (AIMDs) in which AIMDs are those requiring external power. In this dissertation, we focus on AIMDs but will use IMD as a general term.

of most IMDs. Due to the invasiveness of implantation surgery, IMDs must be reliable throughout their patient's lifespan which may spans several decades. In general, an implantable medical device consists of:

- transducers which sense or act on the tissue such as electrodes, strain gauges, or thermistors.
- microelectronics which modify sensed signals or generate stimulatory signals, typically in the form of an integrated circuit (IC).
- a battery, antenna coil, wires and/or other means to provide power to the implant.

Percutaneous connections can serve as routes for infection, so ideally all four components of the neural implant are fully implanted within the body. Depending on the application, emerging implants may need to interface with hundreds or thousands of channels [21, 91, 19, 153, 22, 33]. For most applications, the implantation is expected to be performed once (i.e. no explantation is needed) and would remain functional for the patient's lifetime. Viewed from the perspective of implant mechanical design and material choices, both the tissue reaction to the implant (biotic) and the implant's response to the tissue environment (abiotic) must be considered to achieve a long lifetime in-vivo.

Biotic Reaction

Once the device is implanted, the body mounts an immune response against the device. This has been well-studied and covered by numerous reviews [81, 109, 111, 143]. A hallmark event of the immune response to implanted foreign body is gliosis in the central nervous system [160, 119, 87, 149] and fibrosis in the peripheral nervous system [115, 60, 31]. While fibrosis can occasionally be useful to stabilize implants, the presence of scar tissue in both the central nervous system and peripheral nervous system reduces the efficacy of implanted devices by walling off healthy tissue from the electrodes. However, smaller implants have been found to have reduce scar tissue encapsulation around the device [126]. Furthermore, large implants require more invasive surgeries and can also result in discomfort for the patient, or worse, skin erosion [103]. Thus, miniaturizing implants is highly desirable to increase the efficacy of chronic implants.

Abiotic Reaction

In parallel, the effect of the tissue environment on the implant material stack is also critical. The tissue environment is aqueous, saline, and both chemically rich and chemically aggressive. The immune response mounted by the body in response to an implant releases reactive oxidative species (ROS) which attack and degrade the implant [102, 144]. Corrosion of exposed metals is a major concern, with mitigation strategies heavily relying on material choices. Due to the saline environment of the tissue, galvanic corrosion between exposed metals can occur both in dissimilar metals and between identical metals in different

environments (crevice corrosion) [56, 78]. Corrosion can also be exacerbated by electrical stimulation due to electrolysis, which reduces the pH around the implant [42, 69].

The consequence of these abiotic failure modes is eventual loss of hermeticity. This can result in moisture entering the packaging, shorting and corroding microelectronics. Simultaneously, non-biocompatible materials from the packaged microelectronics may leach into tissue, causing cell death and/or exacerbating the foreign body response [150]. Additionally, the packaging must be a good molecular barrier beyond water vapor since diffusion of mobile ions such as Na^+, K^+, and Cl^- into the integrated circuits within the housing can cause premature failure of the implant [131].

Putting the aforementioned requirements together, the ideal implant is capable of high channel counts while being extremely miniaturized, wireless, biocompatible, biostable, and ultimately hermetic for timescales commensurate with a patient's lifetime. The technology limitation is not in the microelectronics or the interface, as many miniaturized devices with hundreds of channels have been demonstrated [167, 75, 112, 153, 136], but rather in the packaging of the implant components.

1.3 Packaging materials for IMDs

Previous iterations of IMDs have generally relied on polymeric potting (i.e. insulation and mechanical protection) or metal housings. For example, the original pacemakers were encapsulated in thick epoxy before titanium housing became the standard housing for implants (although the leads between internal pulse generators and their electrodes are still potted in silicone). Many researchers have long seen the choice between polymeric encapsulation and metal housing as equivalent to using a conformal material vs the manufacturing of an impermeable envelope [43]. Unfortunately, while polymer encapsulation materials (including silicone, parylene, polyimide, and epoxy) have the advantage of being highly conformal, inexpensive, and easy to apply, polymeric materials are not good long lifetime materials due to their relatively high water vapor permeabilities [146]. The permeation of water vapor can be modeled as:

$$t = \frac{VL}{A}\frac{1}{P}\frac{1}{RT}\ln\left[\frac{p_{external} - p_{initial}}{p_{external} - p_{final}}\right] \tag{1.1}$$

Where

- $p_{initial}$ is the initial water vapor pressure in the package
- p_{final} is the final water vapor pressure in the package
- $p_{external}$ is the water vapor pressure outside the package
- t is the time to reach p_{final} from $p_{initial}$
- V is the free volume of the package

- L is the length of the shortest path needed to diffuse through the material
- P is the permeability of the material
- A is the exposed area of material
- R is the universal gas constant
- T is the temperature

This equation can be separated into three parts:

- a geometric term: $\frac{VL}{A}$
- a material properties term: $\frac{1}{P}$
- and an environmental term: $\frac{1}{RT} \ln \left[\frac{p_{external} - p_{initial}}{p_{external} - p_{final}} \right]$

Our intuition is formalized that highly permeable organic materials result in shorter water-vapor saturation times than less permeable materials such as ceramics and metals (Fig. 1.1).

To compensate for this, larger polymer-encapsulated implants increase their package thicknesses to many millimeters (or more) but it is not a viable strategy for very thin layers in miniaturized devices. In addition, the ROS species discussed earlier are well-known to participate in the breakdown of polymer coatings. For example, parylene is known to crack after months of implantation in the body [7, 144]. Additionally, polymers such as parylene and liquid crystal polymers will undergo material property changes at high temperatures, which prevents the use of steam autoclaves, which generally operate at 120 °C. While ethylene oxide (EtO) sterilization can be used at much lower temperatures, the permeability of polymeric potting materials can allow both EtO and moisture to be stored in the material bulk and a degassing step is required [138].

Due to their very low water vapor permeabilities, metals have been the industry standard for housing implantable microelectronics. In particular, titanium has been the material of choice for IMD housings due to the formation of a stable and inert oxide passivation layer [17]. While titanium housings have been an excellent workhorse during the past 50+ years, they have some limitations. For example, metals alone cannot be used in packaging, as the electrical feedthroughs which connect the electrodes to the microelectronics must be electrically isolated from each other. More conspicuously, the use of metal-only housings generally precludes the ability to efficiently transfer energy wirelessly using electromagnetics without undue heating of the package caused by eddy currents.

In contrast to metals, ceramic materials not only have low water vapor permeabilities, are transparent to RF, can be rendered optically transparent, and, recently, have been shown to be amenable to ultrasonic power transfer [63]. Many ceramics are also chemically inert, biocompatible, electrically insulating, and harder and stronger than most metals [107, 154].

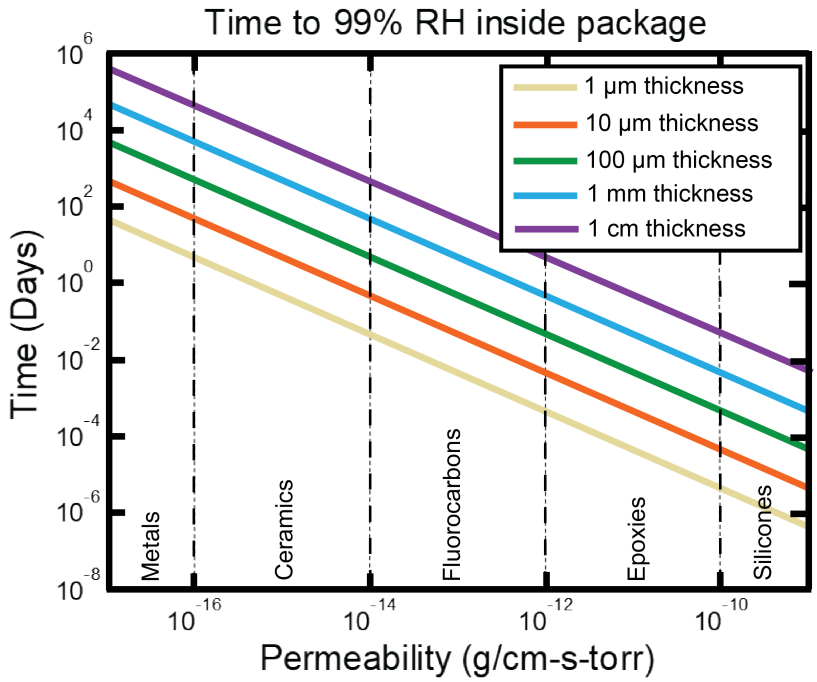

Figure 1.1: Time to 99% humidity based off equation 1.1. Here we assume a sealed rectangular package as a function of diffusion path length and permeability. The typical ranges of permeabilities for different material classes is shown. We can see that ceramics and metals can enable millimeter and sub-millimeter scale chronic implants over polymers. Adapted from [146]

Due to these favorable properties, ceramics have had a long history as implant materials both alone and in conjunction with titanium housing. As implants become more ubiquitous and continue to shrink, ceramics will play an increasingly important role in the development of active implantable medical devices.

1.4 Classic applications and methods of ceramics in medical device packaging

Currently, the major application of ceramics in IMDs is in hermetic feedthroughs, which provide pathways for electrical signals to be routed into and out of the implant housing. The development of the alumina-titanium feedthrough for the cardiac pacemaker significantly increased the longevity of IMDs from months to years and the hermetic alumina-titanium paradigm has been a mainstay of the IMD industry ever since [117]. Ceramics have also been used to improve wireless transmission in titanium housings, acting as windows with some

degree of RF transparency [15, 12]. As a clinical example, the Axonics sacral nerve stimulator utilizes a hybrid titanium-ceramic package for the implantable pulse generator (IPG) which allows for high efficiency electromagnetic coupling [45]. This unique construction allows for an extremely small charging coil, enabling the Axonics IPG to be as small as 5 cm^3. In contrast, other IPGs housed solely in titanium are on the order of tens of cm^3. While completely ceramic housings have been explored, particularly in cochlear implants in which wireless communication is essential, the brittleness of ceramic has been a reliability concern. In cochlear implants, all-alumina housing was explored by Cochlear Ltd, MED-EL, and Neurolec, but due to the large amount of exposed area, the housings were vulnerable to failure due to mechanical impact [140]. Similarly, the first generation BION microstimulator used a glass housing to enhance RF transparency, but found that the housing was prone to fracture after repeated bending stress due to muscle contraction [89]. Careful mechanical design was able to improve the strength of the BION glass housing; subsequent versions of the implant utilized a ceramic housing with a 7x improvement in bending strength [76]. Arguably, the reason glass worked at all for the BION was the small size and relatively thick glass walls. For larger implants, titanium housings remain the preferred solution. Thus, while ceramics may not comprise the majority of modern implant packages, they are an essential component. To this end, whether the ceramic part acts as a communication window, substrate, or feedthrough, it must be shaped and then joined to the rest of the implant.

1.4.1 Ceramic forming

Conventionally, ceramic parts are created from powder, which is consolidated and shaped into a "green body", then fired to densify the final part (Fig. 1.2). Shaping of the green body can be done in a variety of ways but is dominated by "wet-forming" and "dry-forming" methods. In wet-forming methods, the ceramic powder is added to a liquid medium to form a slurry in which binders and plasticizers can be added. This slurry can then be poured into a mold (injection molding) to form a complex shape; tapecast into a sheet for green machining; or slipcast to form a hollow shape; among other methods [165]. In dry-forming methods, the ceramic powder is simply pressed to form the desired shape using methods like uniaxial die pressing or cold isostatic pressing [117]. When forming ceramics, the major concern is avoiding structural defects, such as cracks. These cracks tend to occur during drying processes, such as the drying step needed to remove organic binders and solvents from ceramic slurries. Dry-forming does reduce the risk of cracking, but particle packing homogeneity and shape complexity are worse than for wet-forming methods. Injection molding allows for complex parts with high precision and have been used to form the "comb" style alumina feedthroughs used in cochlear implants. However, injection molding can be limited; particularly complex geometries may result in short shots (incomplete filling of the mold) or knit-lines (improper mixing of the slurry from multiple injection points resulting in stress-lines) [32]. The main method of forming ceramic substrates, particularly for electronics, has been tape-casting; this method can create ceramic substrates with sub-mm thickness [148]. With this method,

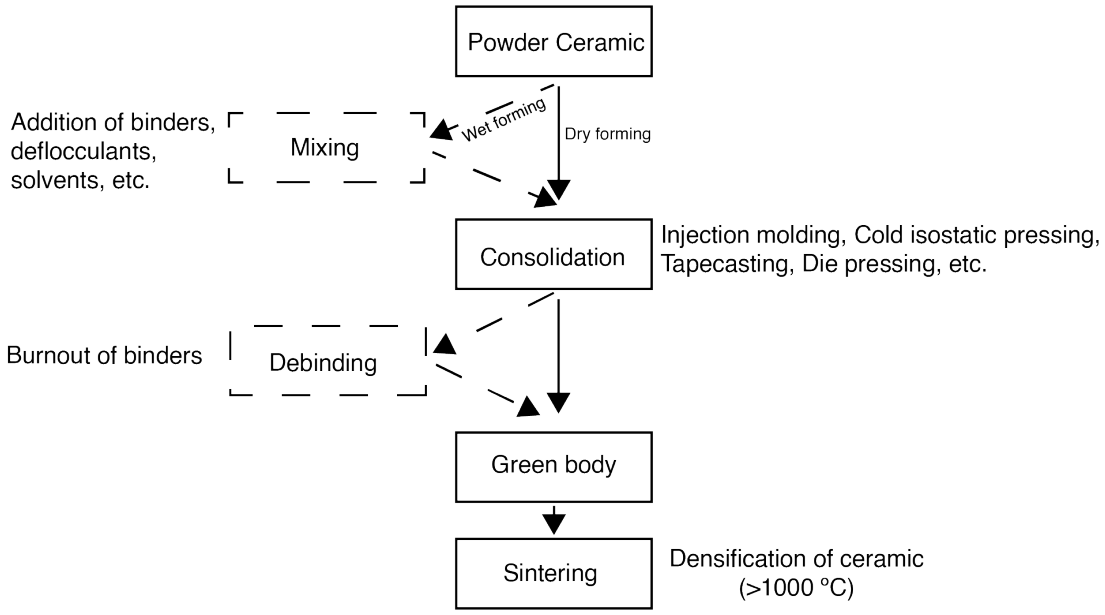

Figure 1.2: Flowchart of the conventional ceramic forming process. Powder ceramic powder is shaped during the consolidation step, with the method of consolidation depending on whether the powder has been mixed into a slurry (wet forming) or not (dry forming). Post consolidation, binders are burned out to form a green body. The green body is then sintered, in which the ceramic particles enlarge and join together to form a dense final product.

a ceramic slurry is doctor-bladed across a surface with a controlled velocity and height to achieve a green sheet with a target thickness. This sheet can then be machined and fired to form the final substrate. 3D printed ceramics are also a promising new technology, allowing for very rapid and cheap manufacturing since they do not require tooling. However, in its current state, 3D printing cannot achieve the same thin substrates as tapecasting; additionally, dimensional accuracy, surface finish and high porosity remain issues [147]. As in many material domains, the prospect of being able to rapidly and cheaply manufacture ceramic parts with high geometric complexity is accelerating the development of 3D printed ceramics; with improvements, additive manufacturing may soon replace techniques like injection molding and cold isostatic pressing [27].

1.4.2 Ceramic joining

Once the ceramic part is formed, it must be hermetically joined to the housing material to form feedthroughs, windows or seals. In a feedthrough, one or more metal pins are also joined to the ceramic body to create conductive paths between the outside and the inside of the package; the ceramic body is then joined to the metal housing of the implant. The

most common method of joining ceramic is brazing, in which two materials are joined with a filler material at a temperature exceeding 450 °C (differentiating it from soldering, which occurs at lower temperatures). Brazing fillers can be either passive or active. In an active braze alloy, the paste generally contains an active element such as Ti or Zr which promotes the adhesion and wetting of the ceramic material [5]. As such, brazing with active braze alloys (ABA) generally requires a vacuum furnace, capable of pumping down to at least 10^{-5} torr. ABAs are widely used hermetic joining of feedthroughs and housing sealing. A classic example is the Ti-Cu-Ni brazing alloy used in alumina-titanium bonding process; the Ti content promotes wetting of the braze alloy on the alumina, and endows the joint with high biocompatibility and corrosion resistance. Partially because of objections to the cytotoxicity of copper, copper-free braze alloys have been explored. Ti-Ni brazes have been shown to hermetically seal zirconia-to-titanium [72] and pure Ni itself was found to be able to hermetically seal the same materials because the titanium from the part was able to diffuse into the nickel to form a eutectic alloy [71]. Both gold and silver ABAs have been utilized to hermetically seal polycrystalline diamond (PCD) packages; the high gold content of the gold-ABA arguably promotes biocompatibility [86]. In the last example, it was found that the gold-ABA did not wet the PCD well, but the silver-ABA could be used as an intermediate layer, with the silver layer not exposed to the tissue environment after encapsulation by the gold layer.

In contrast, passive braze alloys do not contain reactive elements to promote wetting, which allows them to be used in low vacuum environments. Typically, these braze materials are noble metals such as gold or platinum [128]. Unfortunately, passive alloy joints are generally mechanically weaker and somewhat porous [2, 36]. Furthermore, the poor wetting of these alloys to ceramic materials requires a metal interlayer. This can be achieved through physical vapor deposition, chemical vapor deposition, screen printing, or other methods [120].

Co-fired ceramic

While hermetic brazed feedthroughs have had much success, they are limited in pin (conductor) density due to the risk of the ceramic cracking as the conductors are brought closer together [77]. The density limit can be increased integrating metal parts or metal pastes with the ceramic green body and simultaneous firing, a method also known as co-firing [121]. Platinum is used for this due to its high melting temperature, low resistivity, and ability to form solid-state bonds with alumina [3, 62]. Solid Pt wires can be cofired with the ceramic, in which wires are placed between "loaves" of green sheet, compressed together, and fired [57]. This method has been able to create 10 x 10 arrays of feedthroughs with pitches between 400 and 450 μm. When using metal pastes, slurries containing metal particles are screen printed into vias machined into the green body and sintered along with the ceramic [58]. Afterwards, the ceramic substrate with metal vias can be metallized again to form interconnects. Substrates with $\sim$1000 feedthroughs and pitches on the order of 40 μm have been demonstrated. To date, no other method has been able to provide such high feedthrough densities.

Low-Temperature Sealing

One drawback of brazing and co-firing is the high temperature required. During high temperature excursions, thermal expansion coefficient mismatches between different parts can result in cracking or loss of hermeticity. Furthermore, due to the use of organic binders in metal paste feedthroughs, sintering of these pastes can result in void formation which also compromises the hermeticity of the via. Finally, where hermetic sealing of the housing is concerned, high temperature joining is often incompatible with the microelectronic components within the housing. Thus, low temperature methods of joining ceramic are highly desirable.

A relatively new method for low temperature feedthrough formation is to form extruded metal vias with stud bumping [127, 83]. In this method, vias are machined into a ceramic substrate and subsequently metallized. Gold bumps are placed over the vias using an ultrasonic ball bonder to alloy the gold with the via metallization, then coined. In this way, extremely dense hermetic feedthroughs in a ceramic substrate can be made at a low temperature, with a theoretical density up to 2500 feedthroughs/cm^2. While the feedthroughs themselves have been found to be hermetic, to date, substrates with over 100 feedthroughs have been found to be non-hermetic due to misalignment between the gold stud and the via. In published attempts, studs were manually bonded, which contributed to misalignment error. Further work illustrating that automation of the stud placement to improve alignment also improves hermeticity is needed to validate this technique.

Other approaches for sealing packages at low temperature have been explored. Schuettler et al. developed a 360-channel vision prosthetic on a ceramic substrate sealed to a metal cup with low temperature solder in a custom hermetic sealing chamber [123, 122]. While this method yielded devices with excellent hermeticity, the use of solder and the requirement of a solderable housing material left biocompatibility an open question. That work utilized a brass cup for solderability, as titanium is essentially impossible to solder (due to its surface oxide) but brass is cytotoxic as a copper-zinc alloy.

The standard practice for low temperature sealing of titanium housings is laser welding [163, 54]. Laser welding allows for very localized deposition of heat to melt and fuse materials together. This is advantageous for sealing housing without thermal damage to internal components. However, local heating is problematic for joining ceramics due to thermomechanical stresses generated by the large temperature gradient between the laser affected zone (LAZ) and the areas outside of it[2] [161]. Early efforts to circumvent this issue have been to reduce the gradient by preheating the part prior to welding with an oven or a secondary laser [37, 113, 46]. Alternative methods to utilize laser welding include the use of a filler material such as glass frit to aid joining [162]; this enables a form of "laser brazing" proposed for hermetic vision prostheses as well as to seal the previously described PCD implants [152, 86]. More recently, ultrafast laser welding has been introduced as a method for crack-free ceramic joining without needing to preheat the parts [104, 158, 168]. An in-depth explanation behind the interaction between ultrashort laser pulses and matter can be found in

[2]We will see this in chapter 3.

both Miyamoto et al. and Penilla et al. [96, 104]. Briefly, ultrashort laser pulses stimulate non-linear absorption processes in material and can result in embedded molten pools within the bulk material. Because of the short pulse time, the material outside the molten pool remains its original temperature. The embedded molten pool then acts as an elastic body and thus does not generate thermomechanical stresses during cooling. Ultrafast laser welding for ceramic joining is a significant milestone for enabling all-ceramic housing and promises hermetic seals formed without heat-damage to the packaged components. Ultrafast laser welding does have material constraints, but careful engineering or tailoring of the ceramic microstructure can circumvent these issues [104].

1.5 Hermiticity Testing

Ultimately, a package must protect the internal microelectronics from the body environment and prevent compounds from the microelectronics components from leaking into the body environment. Thus, after forming and joining, the package must be leak tested to ensure hermiticity. Hermeticity testing generally occurs in two phases – gross testing and fine testing. A gross leak is defined by the military standard MIL-STD-883 as a package with a standard air equivalent leak rate greater than 10^{-5} atm-cc/sec [59]. A common gross-leak test is the bubble test, in which a detector liquid with a low boiling point is forced into the package by 'bombing.' Bombing is injection of the detector medium into the package by immersing the sealed package in the detector and pressurizing the fluid to drive it into the package. Post-bombing, the package is placed in an indicator liquid which has a much higher boiling temperature. The temperature of the indicator liquid is then raised above the boiling temperature of the detector liquid but below the boiling point of the indicator. This condition is maintained for at least 30 seconds. If bubbles are observed, the package is declared to be a "gross leaker". Presuming the package passes the gross leak test, it is then tested for fine leaks. The current standard method of fine leak testing is to use helium (He) because of its small atomic size and rarity in the ambient environment. Two methods exist for helium leak testing: bombing and backfilling. In bombing, sealed packages are placed into a high pressure He environment, which drives He into the package. The bombed packages are then placed into a chamber with a mass spectrometer and the rate of helium leakage is measured. Alternatively, backfilling may be used in which packages are sealed in a helium environment and then transferred to a mass spectrometer to measure helium leakage. The leakage of He, of course, is not the same as the leakage of water vapor; to predict the water leakage rate, Graham's Law of Effusion is used [151]:

$$L_{water} = \sqrt{\frac{M_{He}}{M_{water}}} L_{He} \tag{1.2}$$

Where L_{water} and L_{He} are the leak rates for water and helium and M_{He} and M_{Water} are molar masses for helium and water. For reasons which will be explored in Chapter 4, it is difficult to pin down a He leak rate that guarantees hermiticity.

1.6 Dissertation Organization

This dissertation explores ceramics as a material for miniaturized, chronic, wireless, implantable medical devices. We investigate the use of ceramics for both ultrasonic and electromagnetic wireless power transfer. In **Chapter 2** we introduce ultrasound as a method for wireless power transfer in the body. We derive and verify models for ultrasound propagation through solids using bulk modes and flexural modes. In **Chapter 3** we build millimeter-scale wireless implants for recording electrical signals, packaged in an alumina-titanium hybrid housing. We introduce and demonstrate passive ultrasonic backscatter communication through the package. Finally, we assess the lifetime of these packages through reactive accelerated aging (RAA) and suggest methods of improvement. In **Chapter 4**, we discuss the use of thin-films as a method of micron-scale packaging. We design and demonstrate a system for rapid RAA of thin-films with in-situ testing. In **Chapter 5** we discuss progress towards chronic-thin film encapsulation of radio-frequency identification ICs and present preliminary work on that front. Finally, in **Chapter 6** we conclude with a summary of major results and discuss future work, uniquely enabled by ceramics and state-of-the-art ceramic processing.

Chapter 2

Ultrasound for medical devices

2.1 Delivering power to miniaturized, wireless implants

As discussed in the previous chapter, completely implanted devices are highly desirable to allow for full closure of surgical sites. This minimizes infection risk at the expense of necessitating wireless power transfer and communication to relay information to and from the implant. Simultaneously, miniaturization of implants reduces tissue perturbation caused by the implant [126, 139]. Unfortunately, energy transfer efficiency and device size tend to scale inversely with each other. As devices get smaller, the amount of available space for energy harvesting decreases, reducing the overall amount of energy harvested by the device. With this in mind, traditional wireless power transfer modalities such as RF or inductive coupling are less effective than ultrasonic power transfer at millimeter to sub-millimeter scales, due to the higher efficiency of ultrasonic propagation in tissue over electromagnetic propagation [39, 24, 8]. In the past decade, acoustic power transfer, in particular at ultrasonic frequencies (frequencies above 20 kHz), has been gaining popularity as a method for powering medical devices; the number of papers discussing acoustic power transfer for IMDs has increased from roughly 6 published papers between the years 2000-2009 to almost 300 published papers between 2010-2018 (Fig.2.1).

2.2 Ultrasonic transmission through solids

The majority of packaging for ultrasonically-coupled implants have utilized polymers as encapsulation materials. For example, Seo et al. packaged an ultrasonically-coupled neural

A part of this chapter is adapted from: Shen, K. and Maharbiz, M.M., 2019. Design of Ceramic Packages for Ultrasonically Coupled Implantable Medical Devices. IEEE Transactions on Biomedical Engineering.

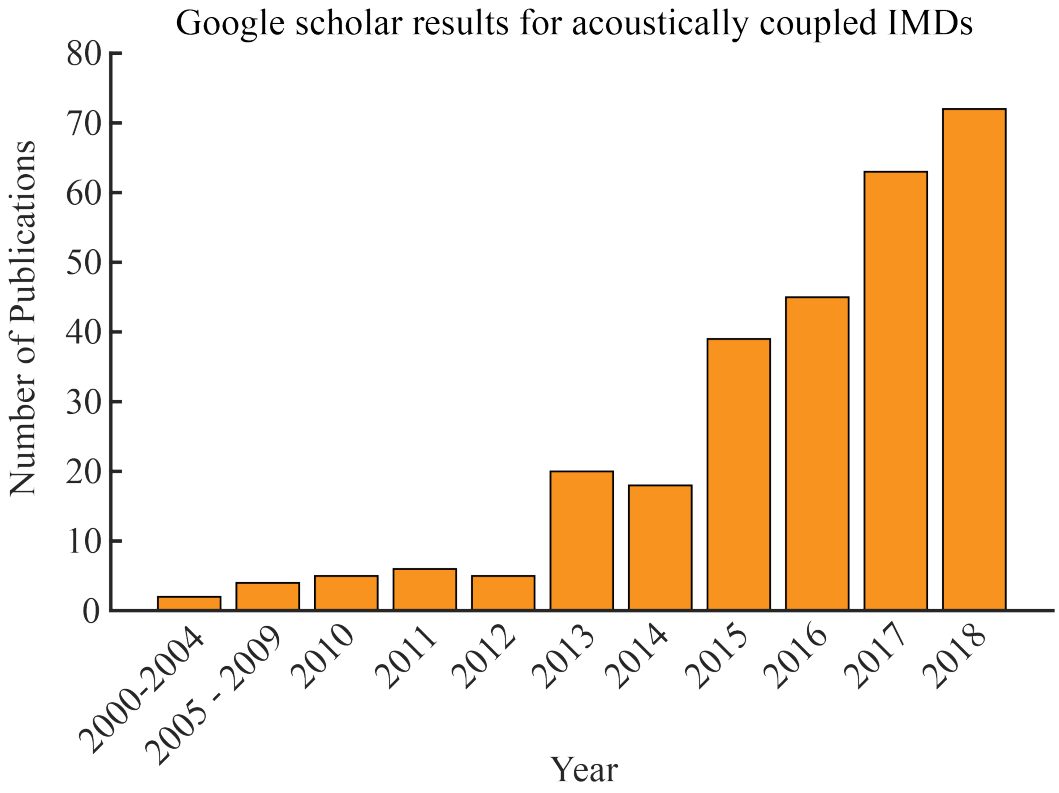

Figure 2.1: Trend in the number of published academic papers on acoustically coupled implantable medical devices (IMDs) over the past two decades. Interest in the use of acoustics for wireless energy transfer has increased significantly since the early 2000s. Results were pulled from google scholar results using the keywords: wireless implantable medical device "acoustic power transfer" OR "ultrasonic power transfer" OR "ultrasonic energy harvesting" OR "acoustic energy harvesting"

probe with a medical-grade UV-curable epoxy, and Piech et al. packaged an ultrasonically-coupled nerve stimulator with parylene-C [125, 108]. While polymeric packaging is suitable for proof-of-concept, it is not appropriate for chronic (and thus clinically-relevant) implantation due to the instability of polymers as molecular barriers. As discussed previously, ceramics and metals are preferred package materials due to their low water vapor permeability and high biostability. However, compared to polymers, ceramics and metals have much greater specific acoustic impedances than that of tissue, which poses a problem for housing acoustic receivers. Naively, the acoustic reflection coefficient for an incoming wave normal to the interface between two media is expressed as:

$$R = \left| \frac{Z_2 - Z_1}{Z_2 + Z_1} \right| \tag{2.1}$$

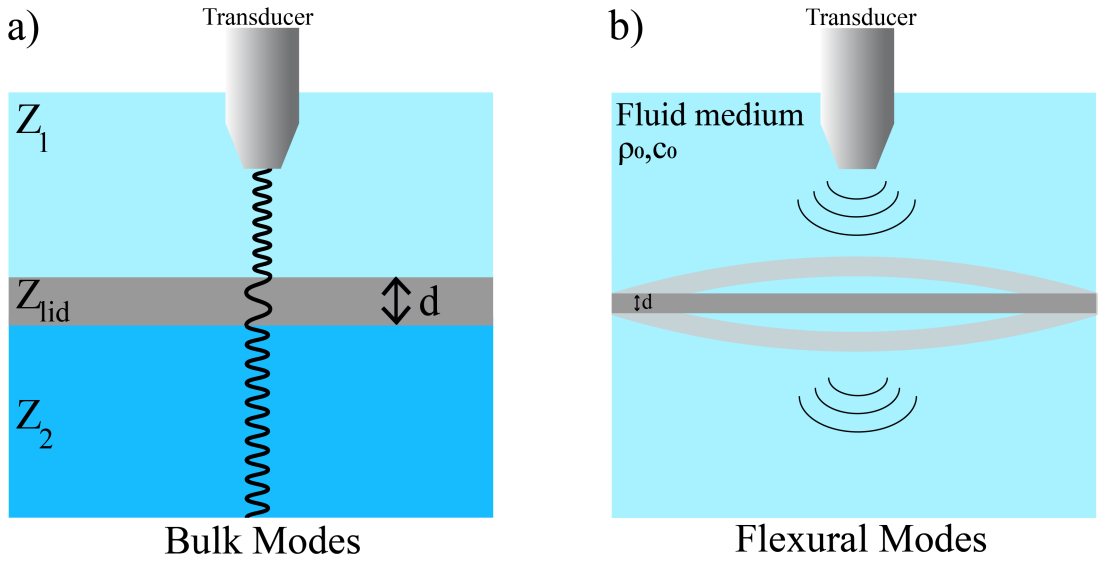

Figure 2.2: Cartoon of sound propagation through two different package lid designs. (a) Bulk mode propagation utilizes longitudinal pressure waves to transmit energy through the package material. (b) Flexural mode propagation relies on exciting resonance modes in the package, radiating acoustic energy through the medium.

Where Z_1 and Z_2 are the acoustic impedances of the two media. Thus, if the acoustic impedances between the two media are very different, we expect that most of the acoustic energy will reflect off the interface rather than penetrating through. However, this model assumes the layers are infinitely thick. As we will see in the following subsections, careful package design can allow for high acoustic transmission at interfaces with drastically different acoustic impedances.

Here we develop two models for the transmission of ultrasonic energy through solids. In the first model, we examine the transmission coefficient of ultrasound utilizing bulk modes to travel through a very thin layer. In the second model, we examine the transmission coefficient of ultrasound using flexural-modes induced in a diaphragm [155] (Fig. 2.2).

Before we begin, let us first consider the sound-structure interaction. When a pressure wave is incident on a solid, the resulting solid behavior is a combination of longitudinal (compression) and transverse (shear) waves propagating through the thickness of the solid. If the structure is surrounded by a fluid medium, energy can be radiated into the medium through flexural vibrations. To maximize transmission using bulk modes, layers which are

thin relative to the ultrasound wavelength can appear acoustically transparent. To maximize transmission using flexural modes, the goal is to design the membrane to have a resonance frequency close to the frequency of the impinging ultrasound. To demonstrate this, we will derive and plot analytical expressions for the transmission coefficient for both coupling schemes in the following subsections.

2.3 Model Derivation

2.3.1 Bulk mode propagation

Let us assume that the primary form of energy transfer is through longitudinal waves traveling through an infinite medium with characteristic acoustic impedance Z_1, going through the bulk of a finite-thickness package lid with characteristic acoustic impedance Z_{lid}, and exiting into another infinite medium with characteristic acoustic impedance Z_2 (Fig 2.2a). We can calculate the transmission coefficient using the wave approach to solve for the input impedance of the combined lid and exiting medium. To do this, we follow the derivation described by Brekhovskikh [18].

We describe a pressure wave going through the package lid at depth z as a combination of forward going and backwards going waves:

$$P(z) = A_+ exp(ik_0 z) + A_- exp(-ik_0 z) \tag{2.2}$$

where k_0 represents the wavenumber of the pressure wave in the package lid. The velocity can be calculated from $v(z) = \frac{-1}{j\omega\rho}\frac{dP}{dz}$; we obtain a velocity expression:

$$v(z) = -\frac{2\pi}{Z_{lid}}(A_+ exp(ik_0 z) - A_- exp(-ik_0 z)) \tag{2.3}$$

We then define the input impedance at the top interface of the package lid (including the infinite medium below it) as:

$$Z_{input} = Z(0) = \frac{P(0)}{v(0)} = -\frac{Z_0}{2\pi}\frac{A_+ + A_-}{A_+ - A_-} \tag{2.4}$$

Because pressure and velocity must be continuous through the media, the interface impedance at the bottom interface of the lid, $Z(d)$, must be identical to the characteristic impedance of the infinite medium Z_2. Then:

$$Z_2 = Z(d) = \frac{P(d)}{v(d)} = \frac{Z_0}{2\pi}\frac{A_+ exp(ik_0 d) + A_- exp(-ik_0 d)}{A_+ exp(ik_0 d) - A_- exp(-ik_0 d)} \tag{2.5}$$

We can rearrange this equation to express Z_2 as a ratio of the forward and backwards amplitudes:

$$\frac{A_+}{A_-} = \frac{Z_2 exp(-ik_0 d) + Z_{lid} exp(-ik_0 d)}{Z_2 exp(-ik_0 d) - Z_{lid} exp(ik_0 d)} \tag{2.6}$$

Plugging Eq. 2.6 into Eq. 2.4 we get:

$$Z_{input} = \frac{Z_{lid}(Z_2 cos(k_0 d) - iZ_{lid} sin(k_0 d))}{Z_{lid} cos(k_0 d) - iZ_2 sin(k_0 d))} \tag{2.7}$$

We can then determine the transmission coefficient through the whole stack as:

$$|T| = \frac{2\sqrt{Z_{input} Z_1}}{Z_{input} + Z_1} \tag{2.8}$$

2.3.2 Flexural mode propagation

Modeling the transmission coefficient of a radiating finite plate has been studied both analytically as well as through numerical methods such as finite-element methods, boundary-element methods, and statistical energy analysis [93, 135]. While numerical methods can be more accurate than analytical methods, they are computationally expensive and time-consuming, especially at high frequencies [34]. Historically, these models were built to predict sound transmission through relatively large structural panels such as windows or building walls, in which the frequency range of interest is on the order of kHz or less. In contrast, we seek an expression for very small panels on the order of millimeters, for which resonance frequencies are on the order of 100s of kHz or higher. Thus, to reduce computational complexity, we sought an analytical expression for the transmission coefficient of a finite plate undergoing flexural vibration. Here, we loosely follow the derivation for sound transmission described by Liu et al. [88]. However, Liu's derivation is for finite plates in air; we account for fluid loading by utilizing results from Cheng et al. as well as Lomas and Hayek [28, 90]. Finally, we use the expression for radiation efficiency derived by Wallace in order to solve for sound transmission over the entire frequency spectrum [156].

Assume a simply supported plate with thickness h, and lateral dimensions L_x,L_y. The incident pressure wave, P_i, is a plane wave normal to the plate with magnitude P_{in}. The equation of motion for this plate can be expressed by Kirchhoff-Love theory:

$$(D\nabla^4 - m_p\omega^2)W = 2P_i - 2P_t \tag{2.9}$$

Where:

- W is the normal displacement of the plate
- ω is the angular frequency of the driving pressure wave
- P_t is the transmitted wave
- m_p is the area mass density of the plate given by: $m_p = \rho_p h$

- $\widetilde{D}$ is the complex bending stiffness given by: $\widetilde{D} = D(1 + j\eta) = \frac{Eh^3}{12(1-\nu^2)}(1 + j\eta)$, where η is the damping loss factor (intrinsic to material). In this derivation, we assume the damping loss factor for Ti is similar to that of Al (η=0.02).

We can use modal expansion to express the displacement, incident pressure, and transmitted pressure as a sum of mode shapes. The mode shapes of a simply supported plate are given by:

$$\phi_{mn}(x, y) = \frac{2}{\sqrt{L_x L_y}} sin\left(\frac{m\pi}{L_x}\right) sin\left(\frac{n\pi}{L_y}\right) \tag{2.10}$$

Then expanding the displacement, incident pressure, and transmitted pressure:

$$W(x, y) = \sum_{m,n} w_{mn}\phi_{mn}(x, y) \tag{2.11}$$

$$P_i(x, y) = \sum_{m,n} p^i_{mn}\phi_{mn}(x, y) \tag{2.12}$$

$$P_t(x, y) = \sum_{m,n} p^t_{mn}\phi_{mn}(x, y) \tag{2.13}$$

Where w_{mn}, p^i_{mn}, p^t_{mn} are modal coefficients. Rewriting the equation of motion with modal expansion:

$$(\widetilde{D}\nabla^4 - m_p\omega^2)\sum_{m,n} w_{mn}\phi_{mn} = 2\sum_{m,n} p^i_{mn}\phi_{mn} - 2\sum_{m,n} p^t_{mn}\phi_{mn} \tag{2.14}$$

From here, we will consider each mode separately. Without loss of generality:

$$(\widetilde{D}\nabla^4 - m_p\omega^2)w_{mn}\phi_{mn} = 2p^i_{mn}\phi_{mn} - 2p^t_{mn}\phi_{mn} \tag{2.15}$$

First, let us use the biharmonic operator on the mode shape:

$$\begin{aligned}\nabla^4\phi_{mn} &= \frac{d^4}{dx^4}\phi_{mn} + 2\frac{d^2}{dx^2}\frac{d^2}{dy^2}\phi_{mn} + \frac{d^4}{dy^4}\phi_{mn} \\ &= \left(\frac{m\pi}{L_x}\right)^4\phi_{mn} + 2\left(\frac{m\pi}{L_x}\right)^2\left(\frac{n\pi}{L_y}\right)^2\phi_{mn} + \left(\frac{n\pi}{L_y}\right)^4\phi_{mn}\end{aligned} \tag{2.16}$$

Plugging this back in we get:

$$\left(\widetilde{D}\left[\left(\frac{m\pi}{L_x}\right)^4 + 2\left(\frac{m\pi}{L_x}\right)^2\left(\frac{n\pi}{L_y}\right)^2 + \left(\frac{n\pi}{L_y}\right)^4\right]\phi_{mn} - m_p\omega^2\phi_{mn}\right)w_{mn} = 2p_m n^i\phi_{mn} - 2p^t_{mn}\phi_{mn} \tag{2.17}$$

We can simplify out the common ϕ_{mn} term and expand $\widetilde{D}$ to yield:

$$\left(D(1 + j\eta)\left[\left(\frac{m\pi}{L_x}\right)^4 + 2\left(\frac{m\pi}{L_x}^2\right)\left(\frac{n\pi}{L_y}\right)^2 + \left(\frac{n\pi}{L_y}\right)^4\right] - m_p\omega^2\right)w_{mn} = 2p^i_{mn} - 2p^t_{mn} \tag{2.18}$$

Now, let us make some definitions. First, let us define the modal wavenumber as:

$$k_{mn} = \sqrt{k_m^2 + k_n^2} = \sqrt{\left(\frac{m\pi}{L_x}\right)^2 + \left(\frac{n\pi}{L_y}\right)^2} \tag{2.19}$$

Next, let us define the modal angular frequency as:

$$\omega_{mn} = \sqrt{\frac{D}{m_p}} k_{mn}^2 \tag{2.20}$$

Then, if we pull out the m_p term and substitute the modal angular frequency we can write:

$$m_p(\omega_{mn}^2(1 + j\eta) - \omega^2)w_{mn} = 2p_{mn}^i - 2p_{mn}^t \tag{2.21}$$

With some rearrangement we get:

$$\frac{m_p}{2}(\omega_{mn}^2 - \omega^2 + j\eta\omega_{mn}^2)w_{mn} = p_{mn}^i - p_{mn}^t \tag{2.22}$$

We can determine the pressure transmitted from the plate also by considering the normal velocity of the plate and multiplying it by the acoustic impedance of the plate:

$$p_{mn}^t = \sum_p q Z_{mn,pq} V_{mn} \tag{2.23}$$

Note that here, our acoustic modal impedance is defined by two pairs of modes; for completeness, we are describing the effects of intermodal coupling on the pressure. Previous work on the radiation efficiency of submerged plates has shown that the effect of mutual coupling (i.e. $mn \neq pq$) is negligible [28], so we will ignore mutual-impedance and only focus on self-impedance:

$$p_{mn}^t = Z_{mn} V_{mn} \tag{2.24}$$

Now, note that $V_{mn} = j\omega w_{mn}$ so we can rewrite the modal displacement as:

$$w_{mn} = V_{mn}/j\omega \tag{2.25}$$

Plugging in our expression for the modal displacement along with our expression for the modal transmitted pressure into the modal equation of motion:

$$\frac{m_p}{2}(\omega_{mn}^2 - \omega^2 + j\eta\omega_{mn}^2)\frac{V_{mn}}{j\omega} = p_{mn}^i - Z_{mn}V_{mn} \tag{2.26}$$

Now rearranging for V_{mn}

$$V_{mn} = [\frac{m_p}{2j\omega}(\omega_{mn}^2 - \omega^2 + j\eta\omega_{mn}^2) + Z_{mn}]^{-1} p_{mn}^i \tag{2.27}$$

The modal impedance is a complex term:

$$Z_{mn} = \theta_{mn} + j\chi_{mn} \tag{2.28}$$

Where the real part, θ, is often referred to as the modal radiation efficiency and the imaginary part, χ, represents the radiation reactance, which is the result of virtual mass loading due to the surrounding fluid. There is not yet a complete solution for both of these terms, but various approximations have been given over the years. The modal radiation efficiency has been solved for all frequencies by Wallace [156] and can be expressed as:

$$\Theta_{mn} = \rho_0 c_0 \sigma_{mn}, \sigma_{mn} = \frac{64 k_0^2 L_x L_y}{\pi^6 m^2 n^2} \int_0^{\pi/2} \int_0^{\pi/2} \left\{ \frac{sin^{cos}(\frac{\alpha}{2}) sin^{cos}(\frac{\beta}{2})}{\left[(\frac{\alpha}{m\pi})^2 - 1\right]\left[(\frac{\beta}{n\pi})^2 - 1\right]} \right\}^2 sin\theta d\theta d\psi \tag{2.29}$$

Where $\alpha = k_0 L_x sin(\theta) cos(\psi)$, $\beta = k_0 L_y sin(\theta) sin(\psi)$, and the use of cos or sin in the integrand depends on whether m is odd ($cos(\alpha/2)$) or even ($sin(\alpha/2)$) and whether n is odd ($cos(\beta/2)$) or even ($sin(\beta/2)$).

The radiation reactance is a strong function of frequency. A completely analytical expression over all frequencies has not been determined, but an approximation used by Lomas and Hayek can be used to good accuracy [90]:

$$\chi_{mn} = \rho_0 c_0 \begin{cases} k_0/k_{mn} & k_0/k_{mn} \leq 1 \\ 0 & k_0/k_{mn} > 1 \end{cases} \tag{2.30}$$

This expression essentially takes into account that at high frequencies, the effect of water loading is negligible. To simplify the expressions, we will use the symbolic radiation impedance for the rest of the analysis.

Substituting the components of the modal impedance:

$$V_{mn} = \left[\frac{m_p}{2j\omega}(\omega_{mn}^2 - \omega^2) - \frac{\chi}{j} + \frac{m_p \eta \omega_{mn}^2}{2\omega} + \Theta \right]^{-1} p_{mn}^i$$

$$V_{mn} = \left[\frac{m_p}{2j\omega}\left(\omega_{mn}^2 - \frac{2\omega\chi}{m_p} - \omega^2\right) + \frac{m_p \eta \omega_{mn}^2 + 2\omega\Theta)}{2\omega} \right]^{-1} p_{mn}^i$$

$$V_{mn} = \frac{2j\omega}{m_p}\left[\left(\left(\omega_{mn}^2 - \frac{2\omega\chi}{m_p}\right) - \omega^2 \right) + j\omega_{mn}^2 \left(\eta + \frac{2\omega\Theta}{m_p \omega_{mn}^2}\right) \right]^{-1} p_{mn}^i$$

Now let us define:

$$(\omega_{mn}^e)^2 = \omega_{mn}^2 - \frac{2\omega\chi}{m_p} \tag{2.31}$$

$$\eta^e = \eta + \frac{2\omega\Theta}{m_p \omega_{mn}^2} \tag{2.32}$$

We can then write:

$$V_{mn} = \frac{2j\omega}{m_p}[((\omega^e_{mn})^2 - \omega^2) + j\omega^2_{mn}\eta^e]^{-1}p^i_{mn} \tag{2.33}$$

Frequently the modal amplitude of the plate velocity is expressed in terms of an admittance:

$$V_{mn} = Y_{mn}p^i_{mn} \tag{2.34}$$

Where the modal admittance is:

$$Y_{mn} = \frac{2j\omega}{m_p}[((\omega^e_{mn})^2 - \omega^2) + j\omega^2_{mn}\eta^e]^{-1} \tag{2.35}$$

Recall the formula for acoustic power is given by:

$$\Pi = \frac{1}{2}Re\{\int_S Pv^* ds\} \tag{2.36}$$

Where S is the area being integrated over. The incident power can be given by :

$$\Pi_i = \frac{L_x L_y |p_i|^2}{2\rho_0 c_0} \tag{2.37}$$

To solve for the transmitted power, we can rewrite this expression in terms of modes:

$$\Pi_t = \frac{1}{2}Re\{\sum_{m,n} Z_{mn}V_{mn}V^*_{mn}\} = \frac{1}{2}Re\{\sum_{m,n} Z_{mn}|V_{mn}|^2\} = \frac{1}{2}Re\{\sum_{m,n} Z_{mn}|Y_{mn}|^2|p^i_{mn}|^2\} \tag{2.38}$$

The power transmission coefficient can then be given by:

$$|T|^2 = \Pi_t/\Pi_i \tag{2.39}$$

The pressure transmission coefficient can be determined by taking the square root of equation 2.39.

Both the model and our experimental validation (see section 2.3) are plotted in Fig. 2.3. Model parameters can be found in Table 2.1.

2.4 Model Validation

Sound transmission models were verified experimentally by building samples out of titanium sheet that utilized bulk or flexural modes, applying a sinusoidal continuous-wave ultrasonic pressure wave with single-element transducers (Olympus, Waltham, MA), and measuring the received pressure with a hydrophone (ONDA Corp, Sunnyvale, VA) in a water tank. The transmission coefficient was determined by taking the ratio of the peak-to-peak pressure at the hydrophone with a sample in the acoustic path to the peak-to-peak pressure at the hydrophone without anything blocking the acoustic path. The hydrophone was placed relative to the transducer so that it would be in far-field. Alignment was performed by maximizing the receive voltage of the hydrophone with no sample in the acoustic path – the samples were carefully added without moving any part of the system once aligned. An acoustic absorber was placed in the back of the water tank to prevent reflection. In all cases, we drove the transducers with a 40 V peak-to-peak voltage.

Longitudinal Transmission Model Parameters	
Acoustic Impedance	
Ti (Z_{Ti})	27.32 MRayl
Water (Z_1)	1.5 MRayl
PDMS (Z_2)	0.99 MRayl
Speed of Sound in Ti	6070 m/s
Flexural Transmission Model Parameters	
Density	
Water (ρ_0)	1000 kg/m^3
Titanium	4506 kg/m^3
Speed of Sound	
Water (C_0)	1500 m/s
Titanium	6070 m/s
Poisson Ratio of Ti (ν)	0.31
Young's Modulus of Ti	120 GPa
Dampling Loss Factor (η)	0.02
Plate Length (L_y)	2 mm
Plate Width (L_x)	1 mm
Plate Thickness (h)	0.1 mm

Table 2.1: Values for model parameters used to simulate transmission efficiency through a titanium plate in longitudinal and flexural modes. The model results are plotted in Fig. 2.3

2.4.1 Bulk-mode validation

To validate our bulk-mode model, we examined the transmission coefficient as a function of both titanium foil thickness and interrogation frequency. We built samples out of printed circuit boards (PCBs) with 6 mm diameter circular vias. The size of this via was chosen so that the largest fundamental flexural-mode resonance frequency of a membrane would be less than 100 kHz, ensuring that any flexural mode contribution would be minimal. The via was first filled with PDMS plug and pressure measurements were taken to obtain a "no-sample" reference. To determine how transmission changes as a function of thickness, we then sealed sheets of titanium of varying thickness to the PDMS plug with silicone, applied 2 MHz ultrasound with a 2.25 MHz center frequency single-element transducer, and measured the received voltage at the hydrophone. For frequency sweep tests, we bonded a 10 μm sheet of titanium over the PDMS plug with silicone and swept the frequency between 100 kHz and 7 MHz. To accommodate for the frequency response of the transducer we used four different transducers with center frequencies 500 kHz, 1 MHz, 2.25 MHz, and 5 MHz to cover the frequency range of interest. In these measurements, the PDMS plug served as a backing layer for the titanium sheets to minimize flexural vibrations and the hydrophone was placed

in contact with the PDMS backing.

2.4.2 Flexural-mode validation

To validate our flexural-mode model, we built titanium membranes from 100 μm thick titanium sheet soldered to custom printed circuit boards (PCB, Bay Area Circuits, Fremont, CA). The PCBs acted as the frame of the diaphragm, with internal slots matching the diaphragm dimensions (2 mm x 1 mm) drilled through the board. A 1 cm x 1 cm pad was placed around the internal slot for the titanium to be soldered to. Due to the poor wetting of solder on the native titanium oxide, a thick copper layer (2 μm) was sputtered onto the titanium sheet. To assemble the membrane, solder paste was applied to the pad of the PCB and a flip chip bonder (finetech, Berlin, Germany) was used to align the PCB to the titanium sheet and reflow the solder.

To test transmission through the membrane, we performed frequency sweeps between 100 kHz and 7 MHz, identical to how we performed the transmission versus frequency experiment for the bulk-mode samples.

2.5 Results

From the bulk-mode transmission model in equation 2.8 we see that in the limit k_0 d approaches 0, Z_{input} approaches Z_2. Written another way, $2\pi d/\lambda_0$, we can conclude that as the thickness of the lid becomes small relative to the interrogation wavelength, the lid becomes acoustically transparent at ultrasonic frequencies. Note that this implies that if the medium underneath the package lid has a significantly mismatched acoustic impedance to that of the medium above the package lid, there will still be large reflections and low transmission.

Based on the empirical results in Fig. 2.3, we observe the following: in bulk-mode coupling, a 10 μm thick titanium lid can preserve nearly 90% of the transmitted pressure given an impinging wavelength of about 3 mm in Ti. This corresponds to a lid thickness-to-wavelength ratio of roughly 0.003. At 1% of the wavelength, we obtain a pressure transmission coefficient of roughly 0.8. This implies that even if we were to use a 20 MHz operation frequency (approximately the bulk-mode resonance of a 100 μm PZT ceramic) a 3 μm sheet of titanium would be sufficient for 80% transmission. Furthermore, from Fig. 4b, it is apparent that this transmission coefficient is purely a function of relative thickness-to-wavelength, and that longer wavelengths preserve high transmission coefficients.

Flexural modes, on the other hand, exhibit strong transmission at resonance, but quickly drop off outside resonance. The construction of our membrane likely results in clamped boundary conditions rather than simply supported boundary conditions. To account for this, we implemented a frequency-dependent correction factor to predict transmission for clamped rectangular panels. For frequencies below the half the critical frequency (f_c), which is the frequency at which the wavelength of sound in water is equivalent to the bending

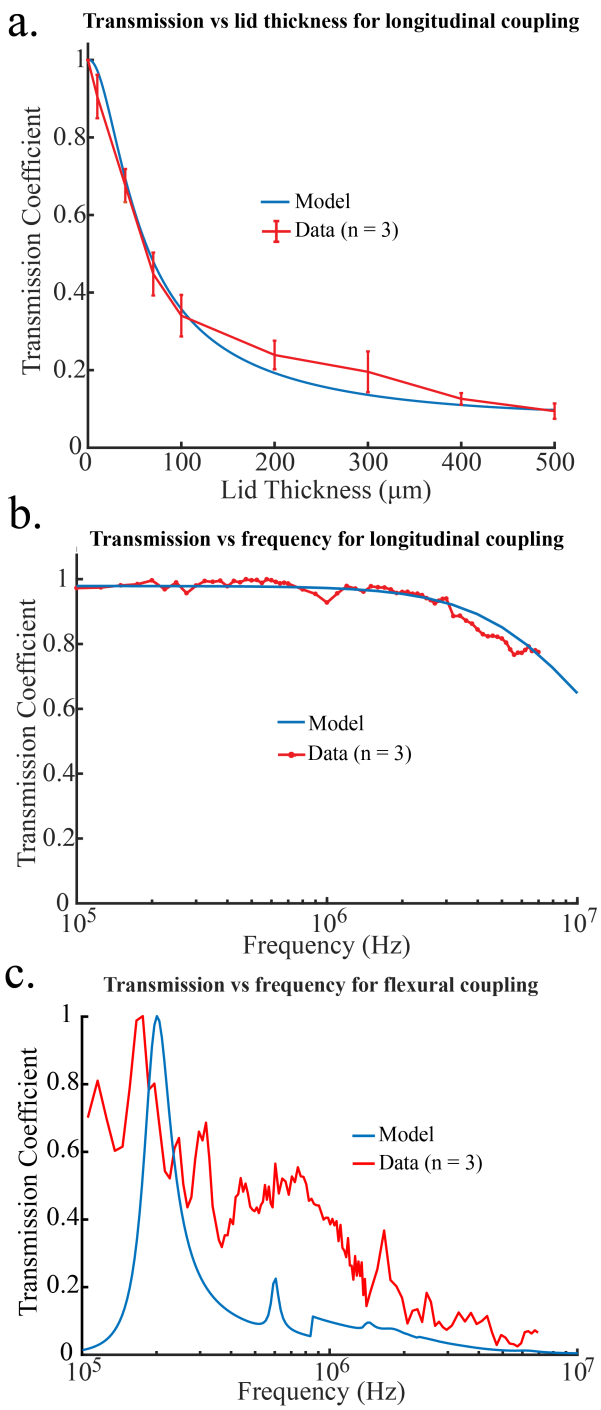

Figure 2.3: Transmission coefficients for the bulk and flexural modes. (a) transmission coefficients for bulk mode transmission as a function of layer thickness. PDMS is used as a backing layer. (b) Transmission coefficient for longitudinal mode transmission as a function of frequency for a 10 μm thick Ti layer. (c) Transmission coefficient for flexural mode transmission as a function of frequency for a 2 mm x 1 mm x 100 μm panel of Ti.

wavelength of the panel, the radiation power of the clamped boundary is double that of the simply-supported boundary. Between $0.5f_c$ and f_c the correction factor approaches unity, and for frequencies greater than f_c there is no difference between the clamped and simply supported panel [93, 47].

2.6 Discussion

We do note that there are deviations from the modeled transmission coefficient in our measured data. The shift in the main resonance peak is likely due to sample-to-sample construction. We built a total of 4 membranes and found that while 3 of these membranes had resonance peaks slightly shifted to the left of the model, one membrane was slightly shifted to the right of the model. Furthermore, due to the size of the drill available from the commercial board house used, it was not possible to get a perfectly rectangular slot in the PCB. Finally, spurious peaks may be present in the frequency response due to the resonances in the set-up. The model assumes an infinite baffle, but the PCB was held in the set-up by an L-shaped kinematic rectangular optics mount (Thorlabs Inc, Newton, NJ), which may have contributed additional resonance peaks. Regardless, the general trend of strong transmission at a single fundamental mode and a rapid drop-off outside of resonance is still preserved

Based on this analysis, we can make the conclusion that while relying on flexural modes will optimize transmission, we can still obtain high (> 0.8) transmission coefficients with bulk-modes. Since the bulk-mode response is more lenient with respect to frequency than flexural-modes, building packages based on bulk-modes may be more effective than packages based on flexural-modes. It is worth pointing out that the piezoelectric efficiency is higher when the medium surrounding it is fluid rather than solid due to damping of the packaged receiver. As mentioned in section 2.3, to minimize flexural modes during bulk-mode transmission characterization, we used PDMS as a backing material. To examine the effect of PDMS encapsulation on a real system, we packaged a cubic 750 μm lead-zirconate titanate (PZT) coupon in PDMS and compared the voltage harvest to a bare PZT coupon when interrogated in castor oil. The effect of PDMS encapsulation on a packaged PZT receiver results in roughly a 50% decrease in voltage harvest compared to a bare piezo (Fig.2.4). Thus, while bulk-modes enable a wider bandwidth, flexural-modes may be more appropriate for applications requiring higher harvested powers.

2.7 Conclusion

In this chapter, we introduced ultrasound-based wireless power transfer as a competitor to traditional EM-based wireless power transfer due to its high efficiency in traveling through the body. Although, the use of ultrasound as an energy transfer modality appears to be incompatible with ceramic or metal packaging due to the stark difference in acoustic

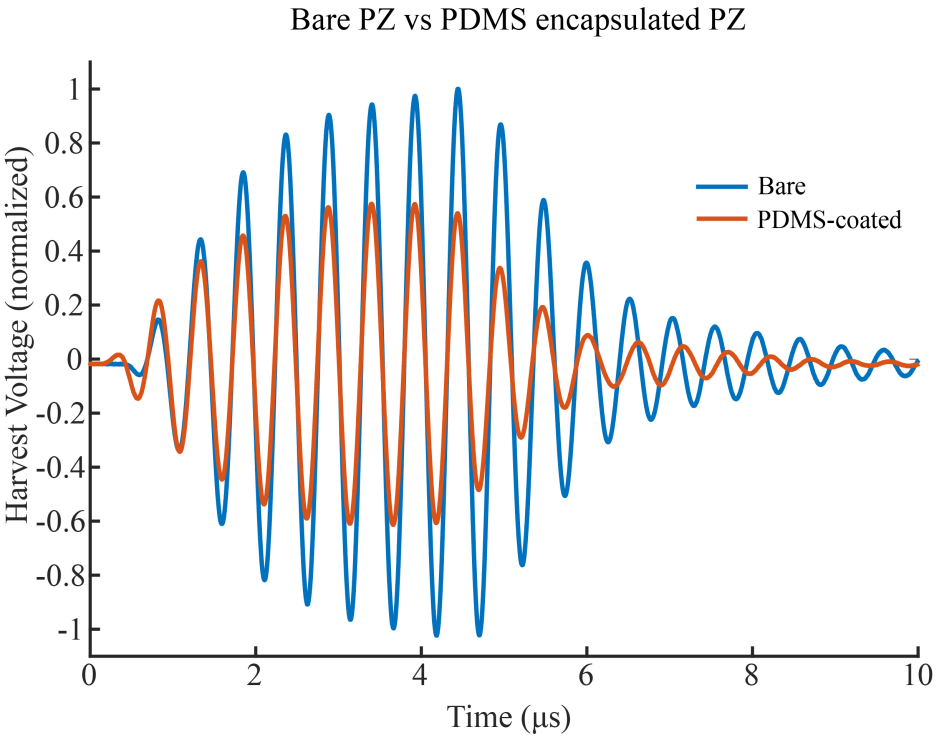

Figure 2.4: PZT coupons potted in PDMS are significantly more damped than bare piezos. The reduction in harvested voltage due to PDMS encapsulation is roughly 50%. Both bare and PDMS-coated PZT samples were mounted on FR-4 PCBs and tested with an 8-cycle pulse-train at roughly 2 MHz in castor oil.

impedance, we show that high efficiency ultrasonic transmission through these materials is possible. We derive analytical models for acoustic transmission coefficients using bulk-modes and flexural-modes and validate them experimentally. These results are promising, as they illuminate a path towards chronic, clinically-relevant, ultrasonically-coupled IMDs. We will use these results to build a packaged system in the next chapter.

Chapter 3

Assembly and testing of a ceramic-metal hybrid package for ultrasonically coupled implants

3.1 Ultrasonic backscattering implants

In the previous chapter, we demonstrated that a material could be designed to appear acoustically transparent for subset of frequencies. This enables the use of metals and ceramics as a packaging material for ultrasonically-coupled implants, which could extend in-vivo implant lifetime to decades. As proof of principle, we sought to build ceramic housing for an ultrasonic, wireless, electrophysiology implant.

We utilize the sensor architecture of the "neural dust" platform, which is envisioned as a distributed sensor network which could be scattered throughout the nervous system performing local neuromodulation for clinical applications. Because the implants (also known as "motes") are meant to be distributed not only in the peripheral nervous system but also the central nervous system, these motes must be as small as possible, hence the desire for ultrasonic wireless power transfer. In particular, if devices are able to minimized to cellular dimenions (on the order of 10s of microns per side), the neuroinflammatory response will be significantly reduced [126]. To reach this goal, the neural dust concept utilizes

A part of this chapter is adapted from:

- Shen, K. and Maharbiz, M.M., 2019. Design of Ceramic Packages for Ultrasonically Coupled Implantable Medical Devices. IEEE Transactions on Biomedical Engineering.
- Shen, K. and Maharbiz, M.M., 2019, March. Ceramic Packages for Acoustically Coupled Neural Implants. In 2019 9th International IEEE/EMBS Conference on Neural Engineering (NER) (pp. 847-850). IEEE.

passive backscatter communication to reduce the number of components necessary such as rectifiers and voltage regulators [124]. In this communication scheme, implanted wireless sensors (motes) are periodically queried by a pulse of ultrasound transmitted by an external transceiver, analogous to radio frequency identification. A piezoelectric receiver converts the impinging ultrasound into electrical energy to "wake up" the mote. Information from the mote can then be encoded in the returning echo, reflected off the mote, and received by the external transceiver. This information is encoded by modulating some property of the incoming pulse, such as amplitude, frequency, or phase. In the simplest implementation of passive backscatter communication, amplitude modulation (AM) can be achieved by changing the load across the piezoelectric receiver. Neural dust used ultrasonic AM-backscatter communication in both electrical recording implants [125, 55] as well as stimulation implants [73], and ultrasonic AM-backscatter communication has also been demonstrated for temperature measurements as well as oxygen detection [100, 133].

By utilizing ultrasonic powering and backscatter communication, the Neural Dust implants have been shrunk to millimeter-scales and have been theoretically shown to scale to sub-millimeter scales. However, to become acceptable for clinical translation, these devices will require robust packaging to yield acceptable device lifetimes. Previous versions of Neural Dust utilized traditional polymeric encapsulants, such as parylene, PDMS, and medical-grade epoxies. While these encapsulation materials are easy to deposit conformally, as we have mentioned previously, they are prone to water vapor transmission, delamination, and degradation in the body environment [17]. As one example of many, Barrese et al. noted cracking in parylene-coated implants as early as 37 days in-vivo [7]. Bioinert ceramics and metals such as alumina, SiO_2, titanium, and gold are orders of magnitude less permeable to water vapor and are also much better at withstanding aqueous saline environments [137]. To underscore this point, Fang et al. explored the moisture barrier properties of a host of materials, including polyimide, SU-8, PDMS, and parylene, and found that even 100 nm of ceramic (thermally grown SiO_2) was a superior moisture barrier to microns-thick polymer coatings [49]. Metallic and ceramic housings have been used extensively in previous work [123, 166, 76, 97], however the combination of ultrasonic power transfer and ceramic or metallic packaging has not been reported on in the academic literature. Properly packaged ultrasonic backscattering implants could enable body sensor networks, in which millimeter and sub-millimeter implants report critical biometrics upon queries from external ultrasound transducer on the skin (Fig. 3.1).

In this chapter, we will describe the design and assembly of a ceramic package for ultrasonically coupled IMDs. We build and package an ultrasonically powered and backscattering sensor for electrophysiological studies and characterize packaged device performance. Finally, we expose packaged devices to a reactive accelerated aging test, characterize device lifetime, and discuss possible failure modes and solutions.

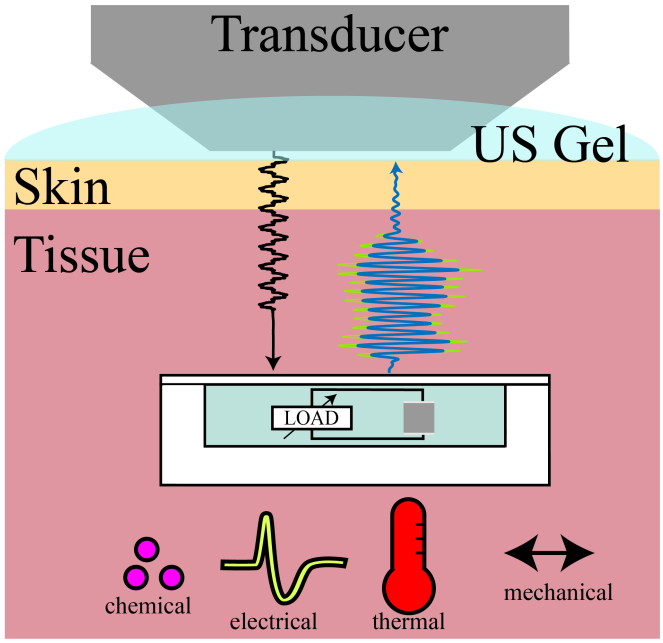

Figure 3.1: System overview for ultrasonically coupled implantable medical devices (IMDs) utilizing ultrasonic backscatter communication. Information from many different energy domains can be encoded in the amplitude of the backscatter (green/blue waves). For these devices to be clinically useful, packaging must be designed that both protects the devices and also allows for ultrasonic coupling.

3.2 Device Assembly

Material selection for these packages is important to ensure biocompatibility and prevent corrosion. Both alumina and titanium, as discussed previously, have had extensive history as biomedical implants due to their inertness and biostability. Dissimilar metals were avoided as much as possible to prevent galvanic corrosion. The metals in use (Au, Pt, Ti) were chosen due to their similar standard electrode potential, which prevents spontaneous galvanic corrosion when submerged in electrolyte [50].

The packaging of ICs and piezoelectrics imposes a relatively low temperature budget on the process. The piezoelectric properties of ceramics are endowed by asymmetry in the crystal lattice of the material. Above the Curie temperature of the material, the atomic structure experiences a ferroelectric-to-nonferroelectric transition, losing its piezoelectric properties. As a rule of thumb, processes should be held below half the Curie temperature to avoid loss of polarization [25]. For PZT, the Curie temperature is ~350 °C, which places an upper limit on process temperatures to ~180 °C. While other piezoelectric materials with higher Curie temperatures could be used, such as aluminum nitride (AlN) or lithium niobiate ($LiNbO_3$), they have worse electromechanical coupling coefficients and there is still an upper limit on

	PZT (APC 841)	$BaTiO_3$	$LiNbO_3$	PVDF
Thickness mode coupling coefficient (k_t)	0.68	0.42	0.162	0.19
Acoustic Impedace (MRayl)	30.5	31.5	34.1	3.92
Mechanical Q	"High"	"Medium"	"Very High"	"Low"
Curie Temperature (°C)	320	1120	1133	110 (melts at 177)

Table 3.1: Physical properties of various piezoelectric materials

temperature set by the IC. A table detailing different piezoelectric materials is found in Table 3.1. Conventionally, ICs cannot tolerate thermal processes above 400-450 °C without permanent damage. The use of PZT rules out many conventional bonding techniques such as Au-Au thermocompression or Au-Sn eutectic bonding. In order to obtain a good seal, but not depole the piezo, we utilized laser microwelding, which delivers heat locally and thus can be used in proximity to heat-sensitive components.

The packaging process is shown schematically in Figure 3.2a. Custom unmetallized 99.8% purity alumina packages were 3D printed (Ceramco Inc., Center Conway, NH). First, 400 μm platinum pins were brazed into the cavity vias at 1060 °C in a vacuum environment ($\sim 10^{-5}$ Torr) with a gold active-braze alloy (ABA) (Wesgo, Hayward, CA), which is an alloy composed primarily of gold (96.4%) and contains trace amounts of Ti which help the alloy wet onto the unmetallized alumina. Once the platinum pins were brazed into the cavity, the cavity was masked off with Kapton tape and a 200 nm thick gold-seal ring was evaporated onto the alumina package with a 10 nm Ti adhesion layer. This seal ring serves as a filler material during the laser welding process. Next, the internal PCB was prepared. PZT samples were cut from commercially purchased pre-metallized bulk-ceramic discs (APC 841, APC International, Mackeyville, PA) with a wafer dicing saw. The PZT and modulation IC were mounted to the PCB using silver epoxy and cured at 150 °C for 15 minutes and wirebonded to complete the circuit. The populated PCB was placed inside the package cavity and connected to the Pt-feedthroughs with silver epoxy. The package was then carefully filled with PDMS as an acoustic coupling medium. To minimize shrinkage during curing, the PDMS filled packages were cured at room temperature over 48 hours. Finally, a 10 μm sheet of titanium was bonded over the package cavity with an additional thin PDMS layer and a 3D printed alumina frame was clamped over it to provide mechanical support during laser welding. The entire ensemble was then welded together with an Nd:YAG laser (LaserStar, Riverside, RI). The device is shown in Fig. 3.2b,c.

3.3 Characterization Methods

The strength of the alumina weld joint was evaluated by a tensile pull-test using a linear tensiometer (Mark-10, Copiague, NY). Two commercially available alumina LCC packages were welded together. Due to the small size of the package, handles were epoxied onto the top and bottom of the package, taking care not to get epoxy over the weld seam. The

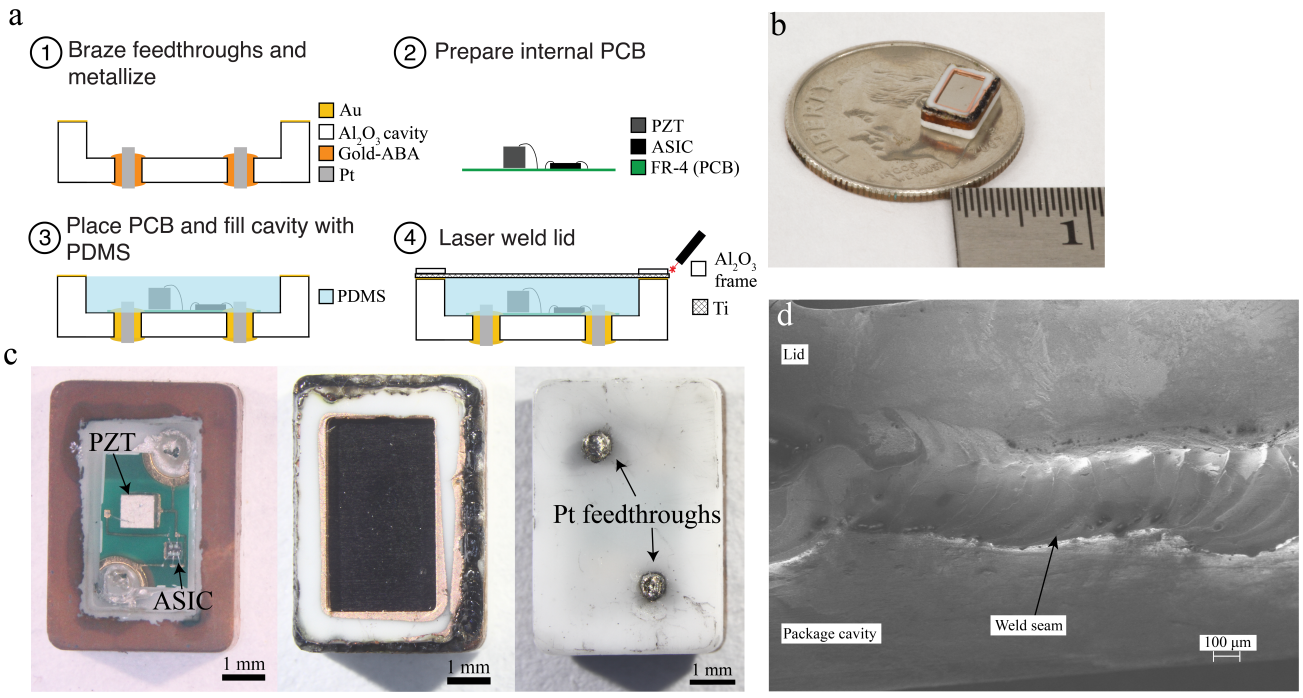

Figure 3.2: a) Packaging steps b) picture of a sealed package on a dime. c) Micrographs of the package prior to lid sealing, post lid sealing, and from the backside. d) SEM of weld-seam where the alumina frame is welded to the package cavity. A continuous weld can be seen, joining the two pieces together.

package handles were then pulled until the package broke apart while measuring the applied force. To determine the strength, the applied force was divided by area of the weld seam.

Link efficiency measurements were made by taking the ratio of the harvested power from the packaged PZT and mechanical output power of the transducer, measured by hydrophone. To calculate the harvested electrical power, we measured the harvested voltage across the piezo terminals and used:

$$P = \frac{V_{rms}^2}{Z_{pz}} \tag{3.1}$$

Where Z_{pz} is the electrical impedance of the piezo at resonance.

Power harvesting penalty with respect to misalignment was characterized for both in-plane translation as well as out-of-plane rotation. To characterize in-plane translational misalignment, the transducer was mounted on two orthogonal manual translational stages. To characterize the rotational misalignment, the mote was mounted to a goniometer such that the axis of rotation passed through the centerline of the piezo. This was important in order to avoid possible translational offsets due to the rotation of the piezo.

To characterize the backscatter circuit, we used a sourcemeter (Keithley, Cleveland, OH) to obtain I-V curves by applying a 100 mV supply voltage while measuring the drain-source current. The gate voltage was swept from 0 to 500 mV.

To determine how the amplitude of the reflected signal modulates with respect to input voltage, we swept the input voltage of the device from 0 to 500 mV in 1 mV increments while interrogating the mote with ultrasound and measuring the backscattered signal. In order to find the mote, a 300 mV, 1 Hz square wave was applied, and the transducer was steered until modulation in the backscatter signal was maximized. At each input voltage, we collected 50 backscatter pulses and averaged over them. Total modulation was determined by taking the difference between the averaged backscatter pulse at the input voltage of interest and the averaged backscatter pulse with a 0 V input. The difference signal was then rectified and a region of interest (ROI) with the largest modulation was identified. The rectified ROI in the difference signal was integrated over to provide a single value characterizing the modulation for the given input voltage. In this way, a calibration curve converting between backscatter modulation and input signal could be created. The ROI was kept constant for all input voltages during a single calibration run. MATLAB code for generating the calibration curve can be found in Appendix A.

Wireless demodulation of the input signal was performed by determining the modulation value for each received waveform in the same manner as calibration and running it against the calibration curve to back out the input value.

The projected lifetime of the packaged device was determined using a reactive accelerated aging (RAA) test [144]. The devices were placed in PBS with 20 mM H_2O_2 to simulate the body environment after implantation. The aging set-up consisted of a jacketed flask with a flexible heater on a hot plate, a temperature controller (Omega Engineering, Norwalk, CT), and a peristaltic pump (Longer Peristaltic Pump Co., Hebei, China). The hot plate was used to provide the bulk of the heat, whereas the flexible heater was controlled by the temperature controller to provide fine control over the temperature of the flask. The pump was necessary to continuously perfuse the solution due to the short half-life of H_2O_2 at high temperatures. The pump speed was set to completely replace all solution in the flask in roughly 20 minutes, corresponding to the half-life of H_2O_2 at 90 °C (the highest temperature utilized). We monitored the performance of the device by performing device calibration daily and ended the experiment when backscatter modulation could no longer be detected. RAA was performed at both 90 °C and 80 °C. To predict the mean time to failure (MTTF) at physiological temperatures, lifetime data was fit to an Arrehnius model defined by [4]:

$$MTTF(T) = R_0 exp(\frac{E_a}{k_B T}) \tag{3.2}$$

3.4 Results

Fig. 1.2d shows an SEM image of the weld seam. The scalloped features show the overlap of the pulses and the seam shows that the two pieces of ceramic have fused into a single piece

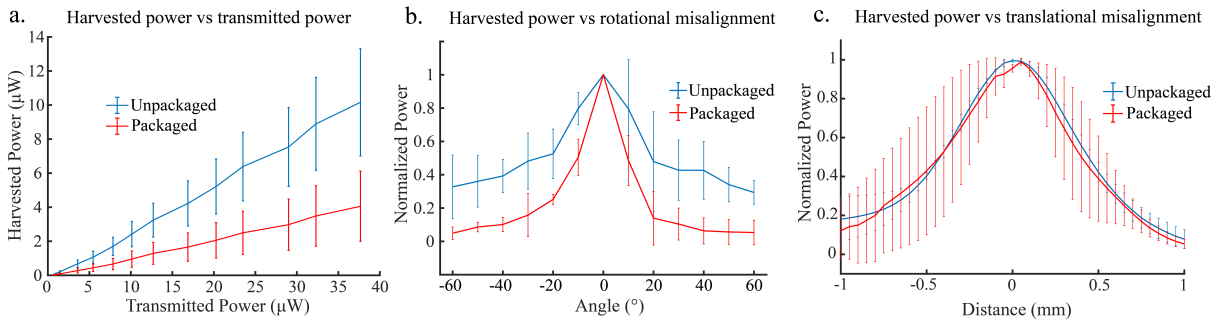

Figure 3.3: Power harvesting performance of packaged mote with unpackaged mote as a control. a) Received power as a function of transducer amplitude. b) Angular misalignment effect on power harvest. c) Effect of translational misalignment on power harvest

rather than melting the gold-seal ring as a filler. During tensile pull tests, out of the three tested weld seams, we were only able to separate one package. The measured bond strength was roughly 26 MPa. In the other two packages, the handles broke off prior to the weld breaking, implying that the weld strength is at least 8 MPa. These values are similar to those of Au-Si eutectic bonding [98], indicating that the laser welded lids are robust.

Figure 3.3 shows the effects of the packaging on power harvesting and misalignment penalty compared to an unpackaged device. The unpackaged mote has a link efficiency of roughly 25% when perfectly aligned; the packaged mote efficiency is roughly 10% with perfect alignment. Thus, the mean penalty in power harvest, as shown in Fig. 3.3a., due to packaging is roughly 40%. The effect of packaging on translational misalignment is minimal (Fig. 3.3c), but due to the walls of the package, there is a substantial penalty due to angular misalignment for the packaged mote as opposed to the unpackaged mote (Fig. 3.3b). We note that the 3 dB point for the unpackaged mote occurs when roughly 20 degrees off axis, while the 3 dB point for the packaged mote occurs roughly 10 degrees off-axis.

Figure 3.4a shows the calibration curves used to demodulate input signals from ultrasonic backscatter plotted against the IV characteristics of the modulation circuit. There is good agreement between the IV behavior of the modulation circuit and the backscatter modulation, demonstrating that amplitude-modulated backscatter communication can be used with the packaged devices. Figure 3.4b shows that we are capable of wirelessly reconstructing input signals of varying amplitude and frequency with good fidelity (correlation coefficient R = 0.88). Here, we input a varying square wave pattern consisting of 1 Hz 500 mV square waves, 2 Hz 500 mV square waves, 1 Hz 450 mV square waves, and 2 Hz 400 mV square waves.

Figure 3.5 shows an example reconstruction from an aged device at 90 °C for 3 days. The reconstruction is still faithful to the input signal, with a correlation coefficient of 0.95. We found that devices failed after aging for 4 days at 90 °C and 8 days at 80 °C. Fitting this to Equation 3.2, we predict a lifetime at 37.5 °C to be roughly 158 days.

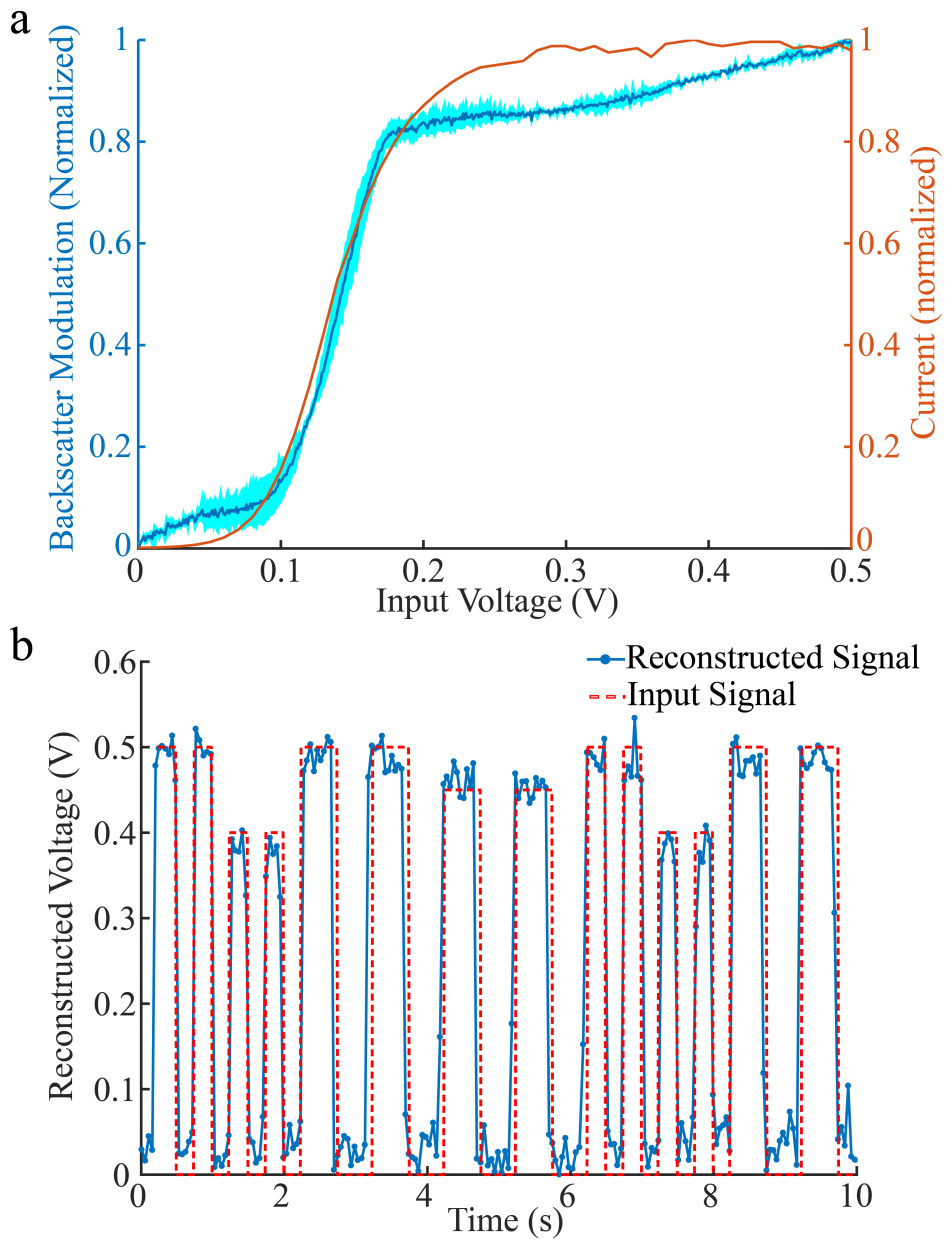

Figure 3.4: Demonstration of wireless backscatter communication in packaged motes. a) Backscatter modulation shows a good agreement with the IV characteristics of the modulation circuit (dark blue indicates the mean, light blue indicates the standard deviation, n = 3). b) The blue traces show the signal demodulated from the backscatter, which is in agreement with the input signal (red). As shown, signals of various frequency and amplitude can be reconstructed.

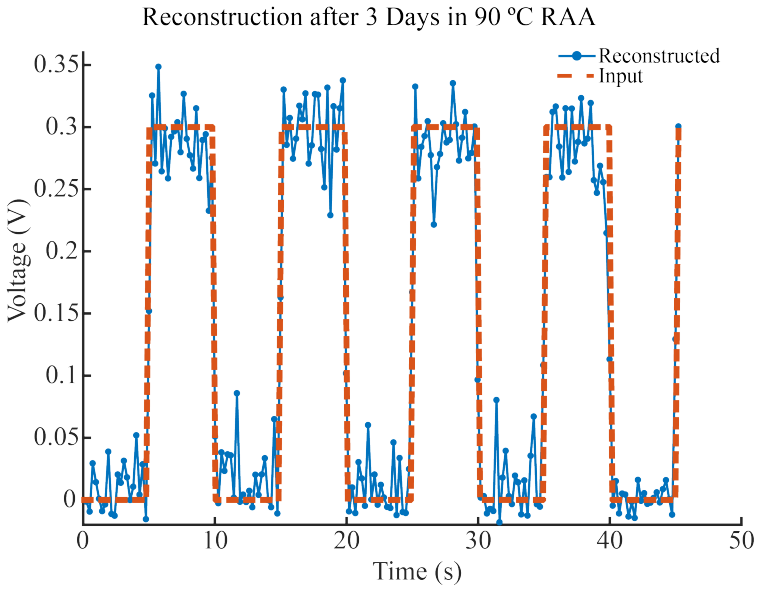

Figure 3.5: Wireless reconstruction of 100 mHz, 300 mV square waves after 3 days of RAA at 90 °C and 20 mM H_2O_2 concentration demonstrating that the device can continue to operate and communicate after aging.

3.5 Discussion

Our results show that thin Ti lids and laser welding can enable ceramic and metal packaging of ultrasonically coupled implantable devices. By utilizing bulk modes in the 10 μm Ti sheet induced by 2 MHz ultrasound, we were able to attain 10% link efficiency as well as effective backscatter communication. While our ultrasound transmission model and experimental data suggest higher efficiency transmission with flexural modes, we chose to utilize bulk modes to simplify lid design since the resonant frequency of the lid needs to match the resonant frequency of the piezo in order to allow efficient transmission using flexural-mode coupling. Standard microfabrication methods can be used to build lids with acoustic windows that resonate at the frequency of the packaged piezoelectric receivers, and that would also allow for higher efficiency voltage harvesting since the piezo could be free to vibrate in fluid. Regardless, we find that using bulk-mode transmission is sufficient for amplitude-modulated ultrasonic backscatter communication. Furthermore, as seen in Fig. 2.3, bulk modes result in larger bandwidth coupling, which benefits real in-vivo applications as mass-loading from different tissue types will shift the resonance frequency. The extent and direction of this resonance frequency shift will be dependent on the acoustic impedance of the tissue type [85].

We project our packaged devices to be capable of lasting within the body for several months; this lifetime is similar to that of conventional polymer-based encapsulation tech-

niques [49, 29, 114, 65]. Although we observed complete joining of the alumina frame to its package, in some places of the weld seam, there were micro-cracks with widths up to 10 μm (Fig. 3.6), which likely served as moisture ingress points. Thus, we believe that the main moisture barrier here is not the housing but rather the PDMS and improving the seam quality would greatly increase the hermiticity and thus lifetime of the package. To improve the hermiticity of the weld seam, a thicker filler material could be used to join the pieces so that the laser welding process is more akin to a laser brazing process. The filler could be anything from glass frit to an active-braze alloy or a eutectic paste [9]. Previous work by Lichter et al. showed that diamond capsules could be hermetically laser-brazed together using gold-ABA [86]. For pure ceramic-to-ceramic bonding, custom laser welding systems utilizing non-linear optics could also be employed. Watanabe et al. demonstrated joining of glasses with drastically dissimilar thermal expansion coefficients using ultrashort (femtosecond) laser pulses without the need of a filler material [157]. Itoh and Ozeki demonstrated hermetic sealing of alumina to borosilicate glass using a similar system [68].

Finally, ceramic-to-metal welds could be utilized instead of ceramic-to-ceramic welding. This method of welding was utilized in the clinically tested Bion microstimulator [76], which sought to build a wireless RF based implantable medical device with lifetimes greater than 10 years. In this device, a tantalum electrode was laser welded to a borosilicate glass capsule using a dual CO_2 and Nd:YAG laser, resulting in a hermetic seal [129]. Thus, while in our work, we were not able to obtain a laser welded hermetic seal, we believe that weld optimization is a straightforward task.

In this work, we used PZT as our piezoelectric material due to its high elecromechanical coupling coefficient. However, the use of lead-based piezoelectrics in implantables is undesirable due to the cytotoxicity of lead. Barium titanate ($BaTiO_3$) is a promising candidate to replace lead-based piezoceramics as it has a higher electromechanical coupling coefficient than other lead-free piezoceramics such as $LiNbO_3$ and AlN [23]. Switching to $BaTiO_3$ would be 70% as efficient as PZT (Fig. 3.7), which is acceptable for our use-cases. The drawback to using $BaTiO_3$ is its low curie temperature (120 °C), which sets an even more stringent temperature budget. However, room temperature curing conductive epoxies could be used, and we do not believe that the laser welding process currently employed would depole the piezo.

Using the described packaging scheme, we were able to build slightly smaller packages with dimensions 5 mm x 4 mm x 1.6 mm. The major constraint on miniaturization is the size of the internal PCB. The IC and PZT coupon used in this work together occupy about 1 mm^2. Additional space is required for wirebonding target pads, interconnects, and empty space to accommodate the wirebonder head. As a result, internal PCBs must have dimensions on the order of millimeters. The 3D printing process has a minimum wall thickness of 120 μm, so the overall dimensions of the package would be $\sim$0.25 mm larger in each dimension than the PCB. Sub-millimeter packages are not easy to build using this packaging method but could be realized utilizing flip-chip processes and standard microfabrication techniques.

In chronic applications, an implant is likely to rotate in tissue. To reduce angular misalignment penalties, piezoelectric receivers with smaller apertures can be utilized. Angular

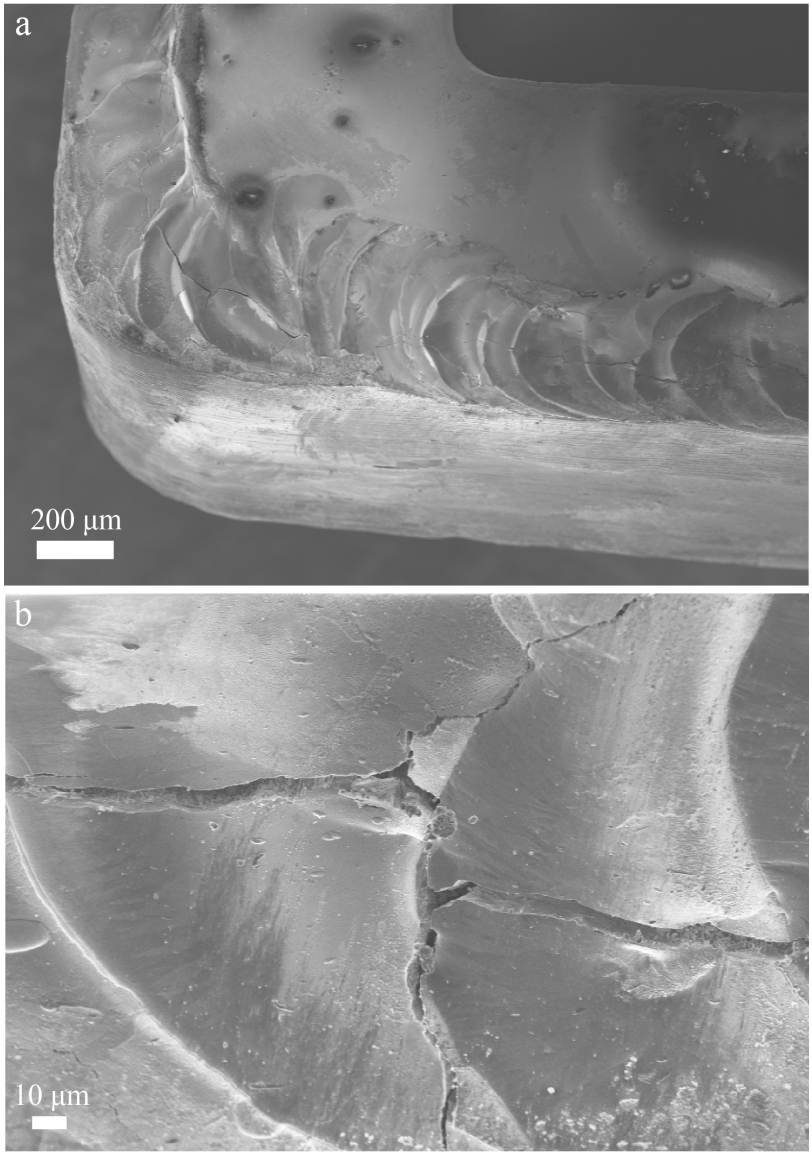

Figure 3.6: SEM images of micro-cracks in the weld seam due to the thermal stress generated by temperature gradients near the weld seam. These cracks can be as wide as 10 μm and compromise hermiticity. Various methods can be used to counter crack formation such as using a filler material to perform laser brazing [86], local preheating of the weld seam using a second laser to minimize thermal gradients [66], or using ultrashort laser pulses [95]

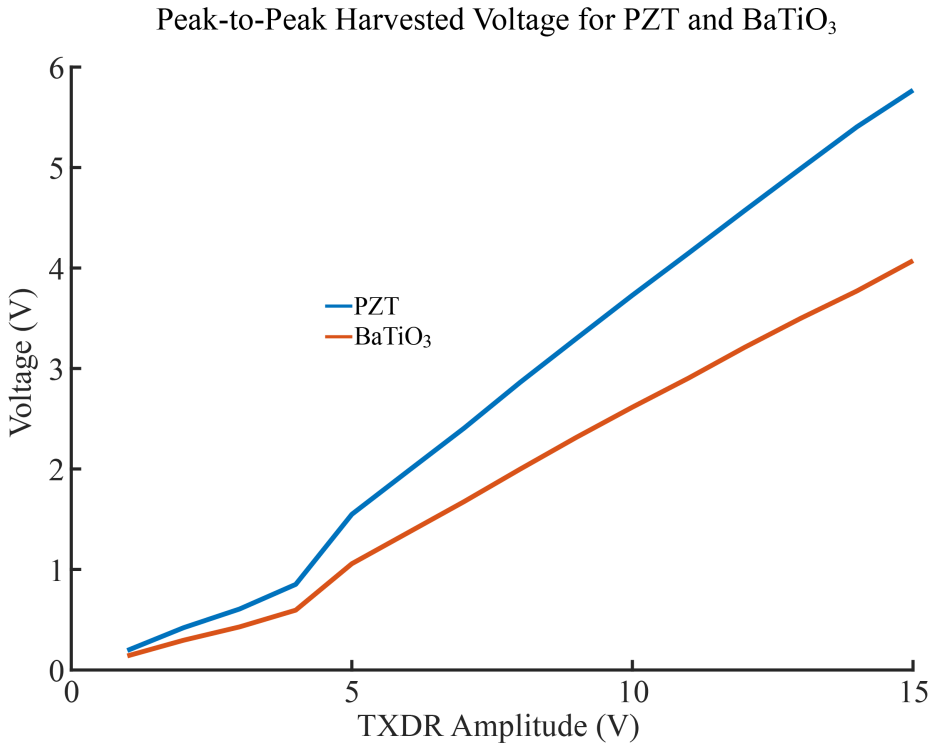

Figure 3.7: Comparison of voltage harvesting between $BaTiO_3$ and PZT. $BaTiO_3$ is a lead-free and biocompatible piezoelectric material [6]. Peak voltage harvest for $BaTiO_3$ is roughly 70% that of PZT which is sufficient for powering our passive amplitude-modulated backscatter circuit. PZT and $BaTiO_3$ samples were mounted on polyimide PCBs and tested with an 8-cycle pulse train at the resonance frequencies of the samples ($\sim$2 MHz and $\sim$2.5 MHz for PZT and $BaTiO_3$ respectively) in castor oil.

misalignment results in an uneven pressure distribution on the face of the piezo, resulting in an uneven charge distribution [30]. Thus, charge may flow across the face of the piezo, rather than building up at the terminals. However, a smaller receiver aperture would result in a more uniform pressure distribution when rotated, thus minimizing rotational misalignment penalties. As a trade-off, less power will be harvested. Assuming the thickness stays the same to preserve the operation frequency, the total volume will decrease, and thus the amount of harvested power.

3.6 Conclusion

In this chapter, we built a ceramic package for an implantable wireless electrophysiology device using the bulk-mode transmission model derived in Chapter 2. The size of the

packaged mote is roughly 4.32 mm x 6.22 mm x 1.6 mm. Communication with the mote is achieved through passive AM-ultrasonic backscatter communication in which the recorded electrical signals modulates the load across a PZT receiver. The modulation circuit consists of a single transistor and a resistor bridge, and is built into a single integrated circuit (IC) [125]. The supply voltage for the transistor is provided by the PZT receiver. The IC and the piezo are mounted and electrically connected to each other on an FR-4 PCB. The PCB is packaged within an alumina housing which has a thin titanium lid to enable ultrasonic coupling. Platinum feedthroughs are used as electrodes to feed electrical signals recorded outside the package into the modulator for wireless reconstruction.

To prevent the PZT from de-poling laser welding process was used during package sealing to keep the heat transferred to the piezo at a minimum. We demonstrated that our packaged devices can both harvest ultrasonic energy as well as communicate information via amplitude-modulated ultrasonic backscattering. While the package is not significantly more effective in protecting the electronics from a corrosive environment than traditional polymer encapsulations, this analysis and fabrication method provide guidelines for developing packaging for ultrasonically coupled implants and similar packaging strategies have been used to build hermetic capsules for IMDs [86, 152].

Ultrasonics have been steadily gaining momentum as an efficient way to couple energy into deeply implanted or mm to sub-mm scale implantable medical devices. While the demonstrated device records electrophysiological potentials, other ultrasonically coupled devices for different applications have been shown such as stimulation, temperature sensing, and oxygen sensing. Thus, this package design and assembly method demonstrate a path towards long term viability and clinical translation of ultrasonically coupled IMDs.

Chapter 4

Thin film encapsulation

4.1 Scaling down packaging

In the previous chapter we demonstrated millimeter-scale packaging in the style of the "impermeable envelope". However, for applications in information dense regions like the CNS, distributed implants should reach sizes on the order of cells. That is, on the order of 10s of microns if not less. To this aim, we contemplated a possible microfabrication process for building sub-millimeter glass capsules in which an IC and piezoceramic could be housed within. Although microfabrication is indisputably a favored manufacturing route to small implants and high densities, severe issues arise, not all of them obvious. For example, the decreasing volumes of microfabricated housings result in a higher likelihood of reaching dew point, resulting in moisture condensation. Thus, smaller packages must have higher hermeticity constraints than larger packages. The relationship between package volume and maximum leak rate can be expressed by [61]:

$$L_{water} = -\frac{V}{t} ln(1 - \frac{Q_{H_2O}}{P_{out,H_2O} - P_{in,H_2O}}) \tag{4.1}$$

Where Q_{H_2O} is the maximum allowed water partial pressure within the cavity, P_{out,H_2O} and P_{in,H_2O} are the initial partial pressures of water on the outside and inside of the housing respectively, V is the free-volume of the housing, and L_{water} is the maximum leak rate allowed to maintain hermiticity within a time period t. The maximum allowed water partial pressure

A part of this chapter is adapted from:

- "An Automated System for Reactive Accelerated Aging of Implant Materials with In-Situ Testing." Shen, K., Yau, A., Panchavati, S., and Maharbiz, M.M., 2020. (accepted at 42nd Annual International Conference of the IEEE Engineering in Medicine and Biology Society)
- "Ceramic Packaging for Neural Implants" by K. Shen and M. M. Maharbiz

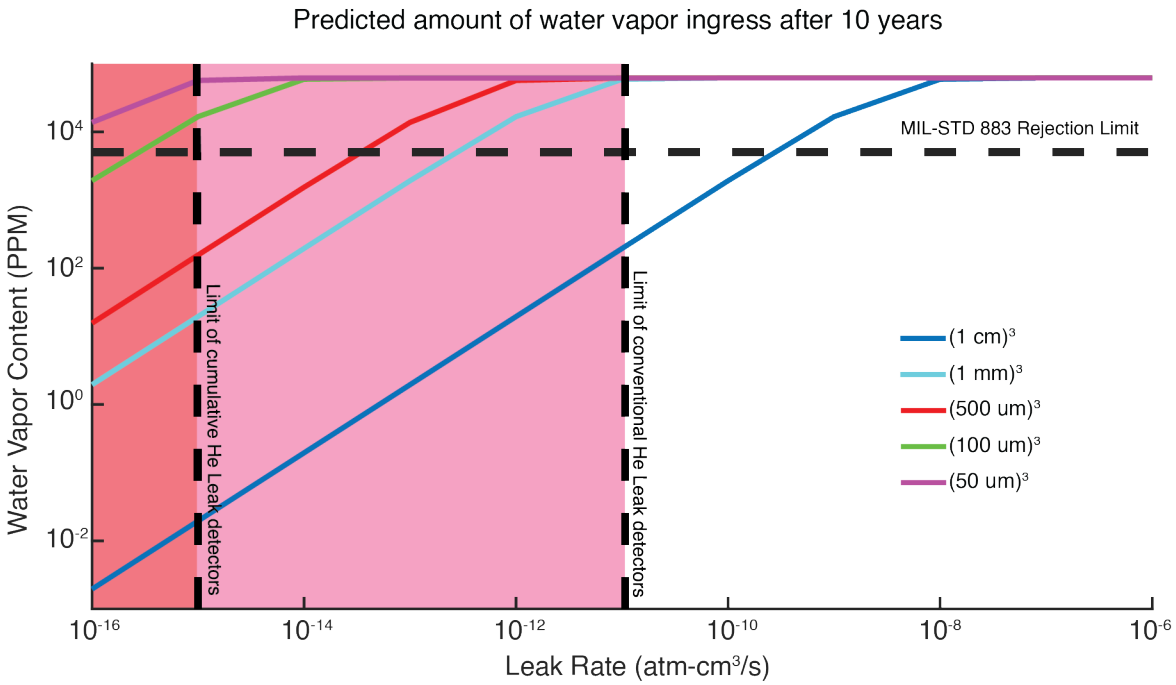

Figure 4.1: Predicted water vapor ingress after 10 years for a given leak rate and a given free volume. The maximum permissible water vapor content in a package is 5000 PPM as mandated by the MIL-STD-883 to prevent condensation. As volume decreases, the maximum allowable leak-rate to achieve a 10-year lifetime without reaching the maximum water vapor content decreases. Furthermore, the maximum leak-rate for small packages quickly becomes too low for conventional He leak rate detection and even cumulative He leak rate detection.

is usually referenced to the MIL-STD-883 recommended value of 5000 PPM, which is derived from the Clausius-Claperyon relationship as the maximum permissible water vapor pressure before condensation occurs.

This relationship between hermeticity (measured in He leak rate), housing free-volume, and moisture content is plotted in Fig. 4.1, which shows the water vapor partial pressure in PPM of a package of a given size and He leak-rate after 10 years. The manufacturing consequence of this phenomenon is that the maximum allowed leak rate for such small packages becomes too low to be detected by most He leak rate detectors currently employed, which are typically limited to 10^{-11} atm-cm^3/s. Some methods have been used to try to improve the detection floor, such as cumulative helium leak detection (CHLD). In CHLD, a specialized cryo-pump is used which is capable of pumping out all other gases besides He from the test chamber, resulting in a higher detection sensitivity. However, Guenther et al. found several problems with this method when applied to microscale packages: outgassing of He from rubber o-rings created significant background noise, and the manufacturer's requirement

of having a test-chamber volume to sample-cavity volume ratio of less than 100 was very difficult without major modifications of the commercially available CHLD instruments [61].

4.1.1 Thin films as a packaging material for IMDs

Due to the difficulty of leak testing miniaturized housings, it follows that a potential path towards long-lasting hermetic implants is to conformally coat devices with packaging material, resulting in zero free-volume within the packaging. Thin film deposition techniques such as chemical vapor deposition (CVD) and atomic layer deposition (ALD) can result in highly conformal coatings to encapsulate implants. These thin films can be on the order of microns to sub-microns thick, which means that the packaging of the device will not add a significant amount of volume to the device. Furthermore, the ability to deposit a film over the microelectronics obviates the need for separate joining processes to seal housings. This is advantageous not only for miniaturization, but also in wireless transmission, where even the small amount of metal in the braze alloy can detune an antenna. Many ceramics can be deposited in this way and have been used as encapsulation materials. Again harkening back to the classic Michigan probe, the conductors on the probe were encapsulated by a bilayer of CVD silicon nitride (SiN) and silicon dioxide (SiO_2) [99]. Xie et al. demonstrated the use of ALD alumina (Al_2O_3) in combination with parylene as a hermetic bilayer, projecting a lifetime beyond 5 years at 37 °C (Xie, et al., 2013). Weiland et al. showed that 5 μm thick diamond-like carbon thin films were effective moisture and ion-barriers, showing only a single pinhole over a 1000 mm^2 area and less than 1% change in electrical properties of an encapsulated integrated circuit (IC) [159].

The work done by Weiland et al. demonstrates another benefit of thin-film deposition technology: low temperature deposition. The high temperatures required for ceramic sintering and brazing for sealing housing are often incompatible with CMOS technology. However, thin-film deposition can often be done at much lower temperatures, with additional energy introduced to the system with plasma rather than heat. Amorphous silicon carbide (a-SiC) for example has been pursued as a coating for neural implants due to its biocompatibility and chemical inertness and can be deposited at temperatures lower than 400 °C through the use of plasma-enhanced CVD (PECVD) [34, 67]. Lei et al. demonstrated the use of PECVD a-SiC deposited at 350 °C as a dielectric coating for retinal implants in which 240 nm. SiC coated retinal prostheses were implanted in rats for up to 1 year, showing significantly less degradation than only SiN coated protheses [84]. ALD hafnium oxide (HfO_2) coatings have also been explored. Jeong et al. deposited alternating layers of 10 nm thick HfO_2 and SiO_2 at 250 °C to form a 100 nm thick coating over an RF communication IC. The encapsulated ICs were demonstrated to work while submerged in 87 °C saline for over 180 days, suggesting much longer lifetimes at physiological temperatures [70].

Another major benefit of thin film ceramic coatings is low flexural rigidity which is a property that bulk ceramic does not have and limits its use as a housing material. As an example, microns-thick silicon carbide can be fabricated into compliant high channel count microelectrocorticography (ECoG) arrays flexible enough to be wrapped entirely around the

sciatic nerve of a rat [40]. Similarly, methods for transferring sub-micron thick SiO_2 layers over flexible electronics have been developed [49]. By laminating thermally-gown SiO_2, Fang et al. demonstrated a 0.95 cm x 1.15 cm, 900-nm thick, 396 channel, capacitive sensor for electrophysiological measurement, which was flexible enough to fit to the curvature of cardiac tissue. That work has been extended to SiN, SiC, and HfO_2 [132, 131, 106].

At these thicknesses, however, degradation mechanisms such as hydrolysis begin to have non-negligible etch rates. For example, ALD Al_2O_3 is known to dissolve in water, hence the need to protect Al2O3 layers with CVD parylene or ALD titania [1, 79]. Furthermore, the material itself is not the only deciding factor for long-term stability of a thin film. The deposition method and parameters are critical to control film quality, bond-composition, morphology, among other physical properties. For example, thermal oxide films were shown by Fang et al. to have a dissolution rate in physiological conditions of roughly 0.04 nm/day, whereas a previous study by Maloney et al. showed a dissolution rate of 3.5 nm/day for PECVD silicon dioxide [49, 94]. Similarly, Hsu et al. found that PECVD a-SiC films deposited at temperatures lower than 200 °C with low hydrogen dilution and high silane-to-methane precursor flow were dramatically less stable than a-SiC films deposited at higher temperatures in silane-starved conditions, which showed nearly no degradation in saline soak tests [67]. Hermeticity testing of thin films is always essential; even small process variations can result in significant changes in film stability.

4.2 Testing thin films

Several methods exist for leak testing thin films. Like in larger "impermeable envelopes", He-leak testing can be performed. However, this may be challenging due to the small sizes of the samples. One common method is to deposit the film-under-test over a test material which is affected by moisture. For example, magnesium (Mg) is highly reactive when exposed to water, hydrolyzing rapidly; a simple method for leak test begins by depositing a thin film of the material to be tested over a square of Mg, then creating a channel over the film and filling the channel with solution [49, 131, 106]. Any pinholes in the film or impurities which can be etched away act as become leakage paths for water to ingress through the film and eventually cause the underlying Mg film to react. The film can be inspected periodically with a microscope for evidence of etching or reaction under the thin film under test. In this way, time to failure can also be recorded and different films can be compared. Optical methods can be unreliable, however; some defects may be too small to identify. A different set of methods rely on shifts in material dielectric properties due to moisture ingress. As an example, resonant inductor-capacitor circuits can be fabricated from thin films or discrete components, thin-film coated with the material to be tested, then placed in a humid environment. By appropriate design of the inductor and proper tuning of the resonant circuit, the resonator can be wirelessly interrogated and impedance spectra shifts caused by changes in the components, putatively caused by moisture ingress [164].

Lastly, for materials acting as feedthrough or electrical insulators, any test should take

into account that electrical potentials will exist across the encapsulation layer during operation. Electrical testing methods should apply these potentials during testing to accurately reproduce the implant environment. In leakage tests, this is usually done by applying a potential and measuring the resulting leakage current. Failure is determined when the leakage current rises above a set threshold current [49, 40, 64].

4.3 A system for rapid thin film testing

Given the large space of film deposition parameters, to determine the suitability of candidate thin films for chronic use, highly parallelized, accelerated aging tests should be utilized to rapidly determine appropriate films and deposition conditions, akin to high-throughput drug testing. As we discussed in the previous chapter, these accelerated aging tests rely on placing test devices or films in environments with high moisture and salt content to replicate the body environment, accompanied by high temperatures to increase the kinetics of failure modes, such as hydrolysis or diffusion [164, 49, 101]. As performed in chapter 3, reactive accelerated aging (RAA), in which ROS are added to the saline solution by hydrogen peroxide, should be utilized rather than just high-temperature saline, as they have been found to replicate the effects of biofluid with higher accuracy [82, 144, 141].

Aging systems have been previously utilized to determine device and film reliability, but often require a substantial amount of human involvement for maintenance and data collection. In particular, the high temperatures used for accelerating degradation kinetics also rapidly degrades H_2O_2 and thus, the biofluid mimic must be continuously replenished to maintain concentration. The ideal RAA system is not only capable of aging many samples, but also requires minimal human involvement over long periods of time, which means that not only should the system be able to maintain aging conditions, but also be able to perform in-situ testing. While previous work has shown automated aging tests with in-situ testing [164] or reactive species [141], the two systems have not yet been combined.

In this chapter, we demonstrate a low solution volume, low cost, automated system for RAA with in-situ film testing of up to 16 samples at a time to determine appropriate thin film encapsulation materials for chronic applications

4.3.1 System Design

Our system is designed to rapidly age and test thin films on silicon (Si) carriers. We expose a pre-determined sample area to hot phosphate buffered saline (PBS) with ROS (H_2O_2) in order to simulate body fluids and accelerate degradation processes. Due to the decomposition of H_2O_2, we must continuously perfuse new solution into the reservoir to keep the H_2O_2 concentration within a reasonable physiological range (10 – 20 mM) [144]. Human involvement in the system is primarily to restock fresh aging solution; to reduce the amount of human intervention, we designed for a low volume sample chamber, such that all solution in the chamber could be replaced with a slow flow rate.

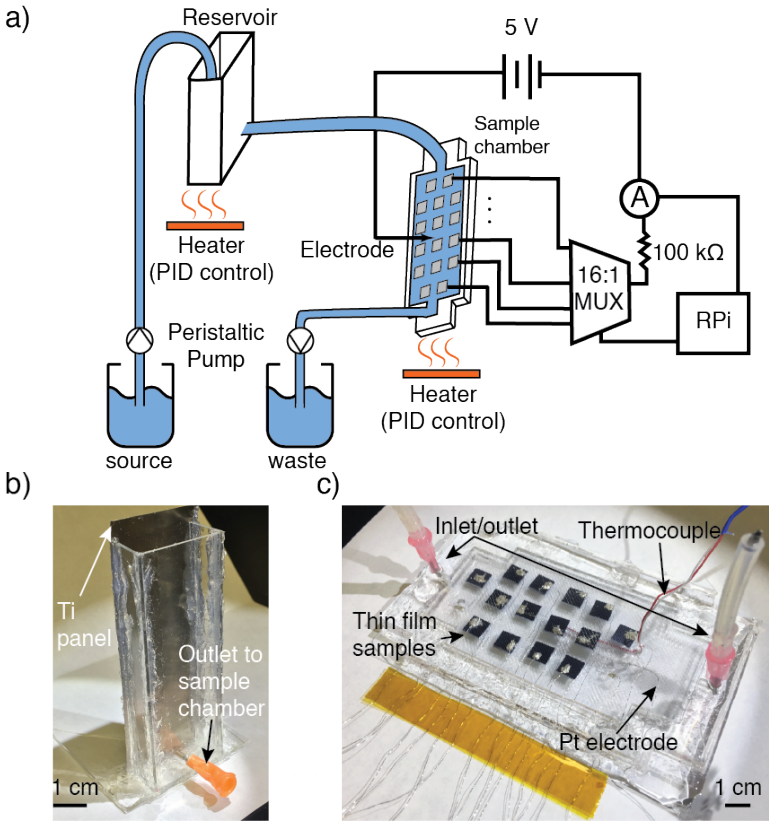

Figure 4.2: System overview. a) Schema of the full system b) Photograph of heated reservoir. The reservoir is constructed out of glass but also includes a 100 μm Ti sheet for heat conduction. c) photograph of the sample chamber.

To quantify film degradation, an in-situ current leak test is performed. A DC bias is applied across the film and current passing through the film thickness is measured [49, 41]. Given a high-quality insulating film, the leakage current is negligible. However, as the film ages, it may develop cracks and pinholes, resulting in increased leakage current.

Based on these design requirements, our system consists of source and waste containers for fresh and used aging solution respectively, a polydimethylsiloxane (PDMS) sample chamber, a glass and titanium (Ti) heating reservoir, a peristaltic pump, a 16:1 multiplexer (MUX), a digital multimeter (DMM), a DC power supply, two flexible heaters with PID controllers, and a Raspberry Pi (RPi) to collect data and communicate with the MUX and DMM (Fig. 4.2a).

As a consequence of trying to accommodate many samples while keeping the sample chamber volume low, the sample chamber has a high surface area to volume ratio, and thus heat is easily lost. To maintain the temperature of the chamber, the chamber is closed to the environment and is heated. However, heating the solution in the chamber results in bubble

nucleation. Because the sample chamber is closed, bubbles are unable to escape, resulting in air pockets in the sample chamber which can prevent samples from being exposed to solution or interfere with current leak measurements. To prevent this, we pump fresh aging solution into a heated reservoir to preheat the solution before it reaches the sample chamber (Fig. 4.2b). By preheating the solution and maintaining the temperature, bubble nucleation in the sample chamber can be avoided [105]. The reservoir is open to the environment so bubbles can escape, with 4 panels of the reservoir being made of glass and one panel made of Ti in order to provide a conduit for efficient heat transfer into the solution. Given that we introduce ROS into the chamber, Ti is a good material choice due to its chemical inertness. Solution is pushed from the reservoir into the sample chamber by gravity, and the solution is pulled out of the chamber via the pump.

Leakage current tests are performed by measuring the current between a Pt electrode in the test chamber and the backside silicon of our samples. The power supply applies a 5 V DC bias between these two nodes, and the current across the sample is measured using the DMM in series with the MUX and the ground of the power supply. A custom python script running on the RPi controls the 16-channel MUX to select the sample to be tested, communicate with the DMM, and display and save the data.

4.3.2 Methods

System Assembly

The sample chamber was cast out of PDMS using a 3D printed polylactic acid mold. A punch tool was used to create access points for the inlet/outlet, Pt electrode, and a thermocouple. A punch tool was also used to create 3 mm diameter exposure sites for the samples to be in contact with aging solution. The samples and sample chamber were cleaned with organic solvents and then plasma bonded together. Wires were attached to the Si backside of the samples with a conductive silver epoxy, and the Pt electrode was placed and sealed into the chamber using PDMS. A second PDMS chamber using the same mold as above was cast to act as a thermal insulator and bonded over the first chamber with PDMS. Next, the inlet, outlet, and thermocouple were sealed into the sample chamber using PDMS. Afterwards, the sample chamber is sealed off with PDMS to a fused silica wafer was diced to the dimensions of the chamber (Fig. 4.2c). Finally, a heater for the sample chamber was added by fixing a heater to a sheet of aluminum foil with Kapton tape, and then folding the aluminum foil around the sample chamber. The sample chamber is 7 cm by 11.5 cm by 0.4 cm and the interior cavity volume is 9 mL.

The reservoir was built out of glass microscope slides and a 100 μm Ti sheet, which were bonded together using silicone. Prior to bonding, an outlet for the reservoir was drilled into the front of the reservoir with a dental drill. The reservoir was then wrapped in aluminum foil to facilitate heat transfer to the reservoir. A heater was attached to the Ti sheet on the reservoir using Kapton tape.

Both heaters were connected to two temperature controllers each, one monitoring the reservoir/sample chamber temperature, and the other monitoring the temperature of the heater to prevent the heater from burning itself out.

All solution was transported through 1 mm ID, 4 mm OD silicone tubing. A peristaltic pump with an adjustable flow rate was used to move solution from the source to the reservoir and from the sample chamber to the waste container.

Finally, the backside Si of each sample was wired to the MUX. The positive terminal of the power supply was connected to the Pt electrode and the negative terminal of the power supply connected to the output of the MUX.

Sample preparation

To test our system, we prepared thin film samples on P-type Si test-grade wafers. Thermal oxide (tOx) samples were prepared via atmospheric wet oxidation at 1050 °C. To access the Si on the backside of the wafer, the backside oxide grown on the wafer during oxidation was etched off via CHF_3 plasma. Amorphous silicon carbide (a-SiC) samples were prepared through plasma-enhanced chemical vapor deposition. All films were diced into 7 mm squares.

Colorimetric determination of H_2O_2 concentration

Hydrogen peroxide concentration was quantified using a colorimetric assay [44]. Titanium oxysulfate solution was diluted in 2 M sulfuric acid in a 1:9 ratio. To construct a concentration standard, concentrations of H_2O_2 were prepared from 0.5 mM to 40 mM. 340 μL of H_2O_2 solution was added to 170 μL of the dilute titanium oxysulfate solution, then the whole solution was diluted by adding 2 mL of 2 M sulfuric acid, vortexed, and placed into cuvettes for spectrophotometry at 407 nm.

To determine the H_2O_2 concentration in our sample chamber, we sampled solution from the waste container. Due to the small diameter of our tubing, the solution cools off almost instantaneously, and does not continue to degrade in the waste container.

To test the degradation of H_2O_2, we placed 3 vials containing 3 mL of H_2O_2 in a convection oven and heated the vials up to 85 °C. The vials were taken out at 15 minutes, 30 minutes, and 1 hour. To compare how H_2O_2 degradation is affected by solution volume, we also tested the degradation of H_2O_2 in a single 250 mL flask heated up to 85 °C on a hot plate with a magnetic stir rod. We extracted 3 mL of solution from the flask at 2 minutes, 5 minutes, 15 minutes, 30 minutes, and 1 hour.

4.3.3 Results

Figure 4.3a shows the temperature of the sample chamber with a set point of 85 °C and a flow rate of 0.46 mL/min. The sample chamber is able to get up to temperature in roughly 15 minutes and the temperature remains stable over the course of five days (Fig. 4.3a, inset), after which the test was stopped. We also examined the H_2O_2 concentration

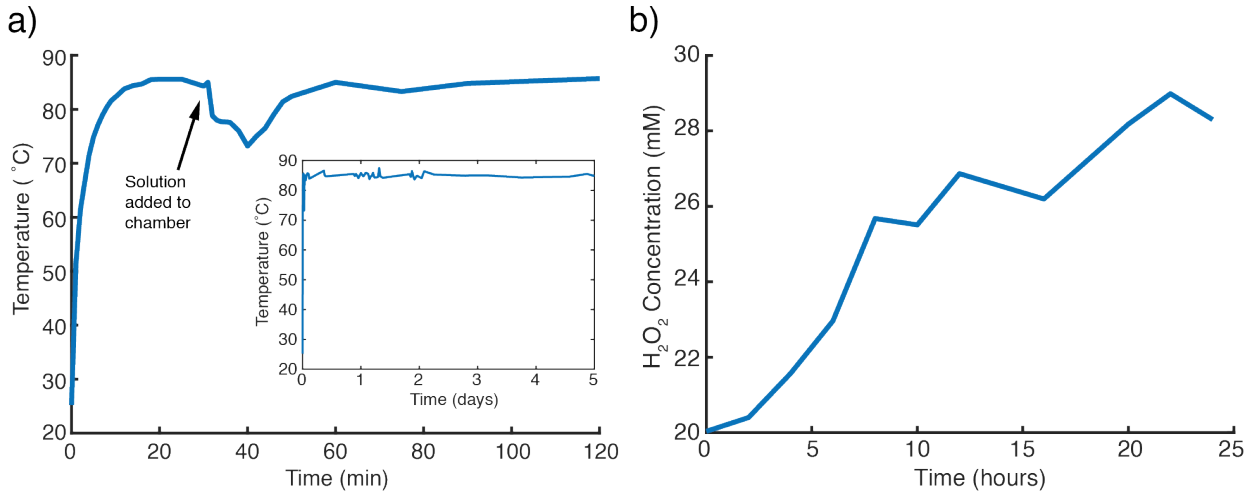

Figure 4.3: a) Temperature of sample chamber over time during ramp up and over multiple days (inset). The sample chamber reaches 85 °C in about 15 minutes. There is a dip in temperature once solution is added to the chamber, but the system recovers and can maintain temperature over several days. b) Concentration of H_2O_2 in solution at 0.46 mL/min flow rate.

under the same conditions (Fig. 4.3b), which we found increased over time, jumping from an initial condition of 20 mM H_2O_2 to nearly 30 mM over the course of 1 day

Interestingly, we observed that the H_2O_2 concentration of our samples increased from baseline as opposed to decreased due to decomposition. We tested H_2O_2 degradation in 3 mL vials at 85 °C for various time points and found that even without refreshing H_2O_2, the concentration of H_2O_2 continued to increase (Fig. 4.4). We hypothesized that the concentration increase was due to the solution evaporating faster than the H_2O_2 can degrade; due to the small volume of solution, a small amount of water evaporation could result in a significant increase in the H_2O_2 concentration. To test this hypothesis, we tested degradation in a significantly larger volume of solution. We heated a 250 mL flask of 20 mM H_2O_2 to 85 °C and periodically sampled the solution. We found that over time, the H_2O_2 concentration decreased, supporting the hypothesis that water evaporation increases H_2O_2 concentration. To further test this idea, we hypothesized that faster flow rates would result in less time for water evaporation and bring the H_2O_2 concentration closer to the original stock concentration. We tested our system with 3 different flow rates: 0.22 mL/min, 0.46 mL/min, 0.77 mL/min and measured the resulting H_2O_2 concentration (Fig. 4.5). As hypothesized, with faster flow the difference in H_2O_2 concentration decreases. With slower flow rates, there is a general increase in H_2O_2 concentration. We believe this is because of the competing reactions between H_2O_2 degradation and water evaporation – slower flow rates allow for more evaporation, but also more time for H_2O_2 degradation. It is worth noting that the degradation

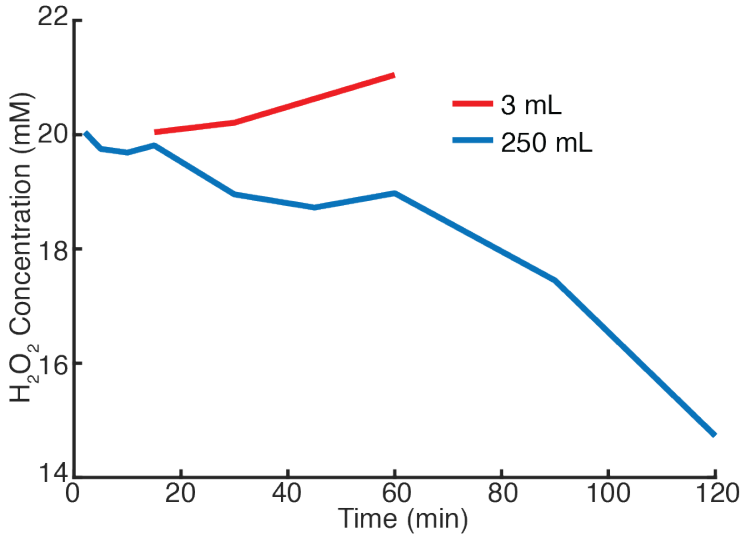

Figure 4.4: Concentration of H_2O_2 as a function of time at 85 °C for two different volumes. For large volumes of solution, H_2O_2 content decreases at elevated temperatures. For small volumes, H_2O_2 content increases due to water evaporation.

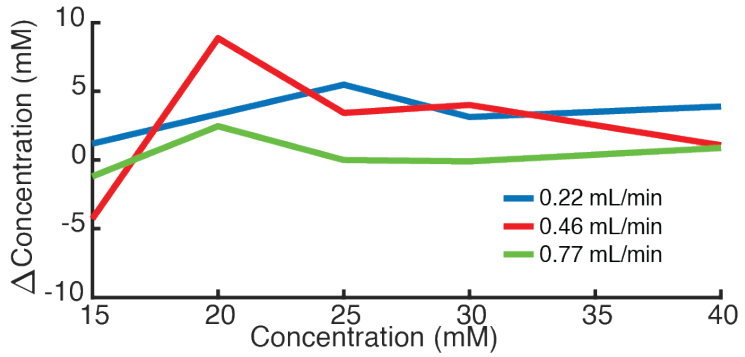

Figure 4.5: Difference in concentration between stock solution and collected solutions for the three pump speeds. 0.77 mL/min obtains a H2O2 concentration nearly unchanged from the stock.

curve of H_2O_2 obtained from the 250 mL flask does not show a classic 1/t behavior. This may be the result of the competing water evaporation and degradation processes or may indicate that there are other factors affecting the measurement. Regardless, we show that at 0.77 mL/min, the flow rate is fast enough that the H_2O_2 concentration remains roughly constant.

We tested samples of fused silica, bare P-type Si, 100 nm a-SiC, and 100 nm tOx to see if

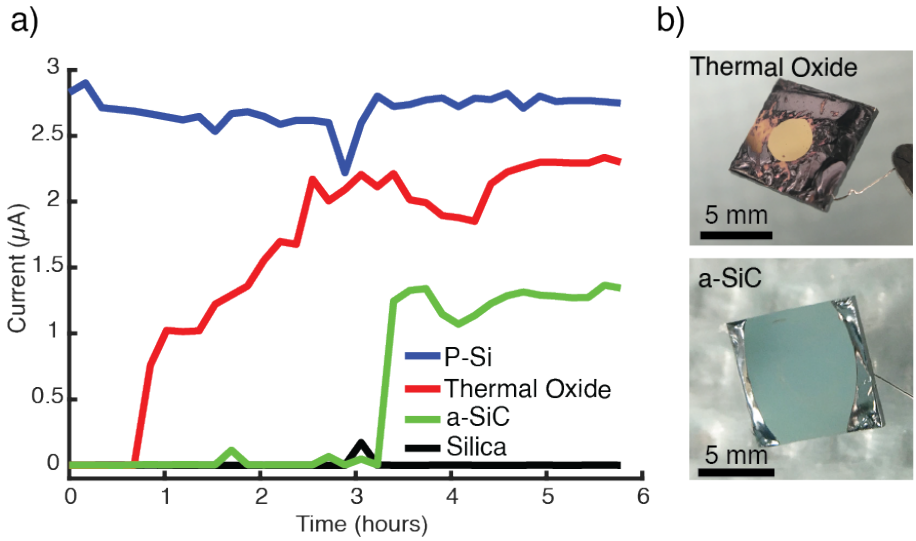

Figure 4.6: a) Current leak test showing 100 nm thermal oxide fails more quickly than 100 nm of a-SiC. P-type silicon and fused silica samples are used as controls. b) Photographs of thermal oxide and a-SiC samples post aging. The thermal oxide sample shows clear evidence of etching based on the color change. The a-SiC sample does not show obvious etching, which may imply small pinholes in the film that resulted in failure.

could detect sample failure. Sample failure was declared when the leakage current increased above 1 μA. The system conditions were approximately 93 °C PBS spiked with 20 mM H_2O_2, and a 0.77 mL/min flow rate. We found that the tOx sample failed within 1 hour, while the a-SiC film was able to withstand aging for roughly 3 hours before failing (Fig. 4.6a). Visual inspection of the samples post test showed clear discoloration of the films, confirming the degradation of the films (Fig. 4.6b). Naturally, the p-type Si sample showed high current for the entire duration of the test, while the silica film showed an open circuit for the full duration.

4.3.4 Discussion and Conclusion

We have developed a high throughput system for reactive accelerated aging that is capable of in-situ testing of thin films. The total volume of solution needed for the chamber is only 9 mL; the system can heat up to 85 °C in roughly 15 minutes and can sustain a constant H_2O_2 concentration with a flow rate of 0.77 mL/min. With a 5-gallon source container, the system only needs to be refilled approximately once every 3 weeks. We demonstrate that the system can detect failure of thin films through current leakage tests. Furthermore, our system is both low cost and highly customizable. The sample chamber geometry can easily be changed, and the area exposed to solution can be varied simply by changing the size of

the punch. Although we show 16 samples, this limit is set by the MUX; a higher channel MUX could allow for simultaneous testing of more films. For testing, we utilized a-SiC, Si, and SiO_2. Other materials can be used with this method provided it is patterned in such a way that there are Si atoms for plasma bonding the sample to the PDMS.

We show that 100 nm a-SiC outperforms 100 nm thermal oxide. This result has been validated in the past, although the lifetime of both our a-SiC and thermal oxide films were shorter than reported in previous literature [41]. Future work will utilize this system to test various a-SiC recipes to determine deposition parameters for effective and process-compatible a-SiC encapsulation for chronic implants.

In the next chapter, we will discuss a route towards thin-film encapsulation of wireless implants.

Chapter 5

Progress towards chronically implantable integrated circuits

In the previous chapter, we demonstrated a system for rapidly aging thin films to determine their suitability for chronic encapsulation. In this chapter, we describe our progress towards encapsulating singulated integrated circuits (ICs) for long-term implantation in the body.

5.1 Chronic thin-film SiC encapsulation for integrated circuits

Chronically implanted integrated circuits (ICs) can enable sophistication in implants beyond measurements, such as closed-loop modulation of physiology. However, the body is a corrosive and chemically aggressive environment in which ionic and reactive oxidative species can easily damage implanted microelectronics. Conventionally, implanted ICs are packaged in titanium or ceramic housing to reach decadal lifetime, but such packaging is not conducive to sub-millimeter scale miniaturization. Thin-film encapsulants such as parylene, SiO_2, and SiC can greatly reduce the size of hermetically packaged devices, but to date, only one study has demonstrated decadal lifetimes granted from thin-film encapsulated ICs. In that study, alternating layers of SiO_2 and HfO_2 to a thickness of 100 nm were used to show benchtop aging of encapsulated ICs for over 180 days at 87 °C, corresponding to a projected lifetime of over 10 years at 37 °C [70]. While this result is extremely promising, the in-vivo tissue response to HfO_2 has not yet been characterized. Furthermore, the failure mode of the HfO_2/SiO_2 stack was also not investigated. The authors noted that there appeared to be no physical defects such as cracks or pinholes that might illustrate film failure, which may imply the poisoning of semiconductors due to mobile-ion diffusion.

Given the extensive characterization of SiC films for implantable devices [106, 34, 67, 80], our goal is to show that microns-thick SiC films can be used as a molecular barrier to enable implantable ICs with lifetimes on the order of decades. To further miniaturize

implantable devices, we utilize flipchip bonding to reduce the size of the device backplane. An electroless gold-bumping method is described and demonstrated to facilitate bumping of already singulated ICs received from a commercial foundry. We hope that our process can enable implantable medical devices which can function for a significant portion of a patient's lifetime. This would open the door to implantable microelectronic therapeutics which would otherwise be unattractive due to the low risk-to-reward ratio inherent due to surgical implantation.

5.2 Silicon carbide as an encapsulation material

SiC has emerged as one of the main contenders for chronic hermetic encapsulation due to its chemical stability, biocompatibility, and molecular barrier properties. The silicon-carbon bond in SiC is extremely stable: silicon atoms are bound to carbon atoms throughout the material, giving SiC its high chemical resistance [92]. As a result, proper tuning of deposition parameters can result in SiC thin films that exhibit little-to-no hydrolysis in-vivo or in-vitro [34, 84, 67, 106]. Properly tuned films have also been demonstrated to be excellent molecular barriers. Diaz-Botia et al. showed that 100 nm of a-SiC outperformed 100 nm thermal-SiO_2 as a barrier to water vapor [40]. Phan et al. showed that crystalline SiC exhibited very low ion diffusivity: after 12 weeks of soaking in 96 °C phosphate buffered saline (PBS), secondary ion mass spectroscopy revealed that by 100 nm through the film, no Na^+ could be detected [106]. Additionally, the biocompatibility of SiC has been demonstrated both in-vivo and in-vitro [34, 118, 51]. Cells cultured on SiC show better adhesion, proliferation, viability, and mitochondrial health than cells cultured on Si [13, 35]. SiC implants were also shown to have a decreased immune response compared to Si implants when utilized in-vivo. Frewin et al. found reduced microglia and macrophage activation attached to implanted SiC samples in rat tissue [52]; Knaack et al. did not find significant differences between microglia and macrophage activation in a-SiC coated Si samples and uncoated Si samples, but did find reduced reactive astrocytes in a-SiC coated Si samples compared to the uncoated samples [80]. Thus, while it is unclear if SiC is definitively more biocompatible than Si, it is evident that SiC is well tolerated by tissue and should be pursued as an encapsulation material. The Cogan group at the University of Texas at Dallas has demonstrated a-SiC encapsulated ultra-microelectrode planar arrays using and Utah electrode arrays [38, 74]. Furthermore, because SiC is a semiconductor, it can be doped to become electrically conducting. Applications of electrically conductive SiC will be discussed in Chapter 6.

5.2.1 Silicon carbide deposition

Thin-film failure modes, as discussed in the previous chapter, generally result from pin-holes during deposition or impurity incorporation in the film which is etched away in the application environment. Previous work by Diaz-Botia utilizing PECVD a-SiC as an encapsulation material characterized the effect of several deposition parameters [41]. In particular,

the deposition power, plasma frequency, precursor flow[1] and chuck temperature effects are characterized. Briefly:

- Deposition rate increases with power between 100 W and 250 W[2], then saturates. However, films deposited with higher power incorporate more impurities.
- Slower precursor flow rates have both slower deposition rates and higher impurity content
- Lower chuck temperatures incorporate more impurities, but generally have higher deposition rates

Naturally, we aimed to deposit films with as high purity as possible to reduce the possibility of dissolved pinholes during aging, while keeping the deposition temperature and duration low to prevent theramlly damaging the IC. Given that lower chuck temperatures were reported as having higher deposition rates, we considered using thicker SiC (~ 10 μm) deposited over multiple runs such that impurities in the film could not be etched away to form a direct path.

To test this, we performed PECVD a-SiC deposition on 6" p-type test wafers. We varied temperature, power, and process pressure, as we imagined that a lower pressure might increase the mean-free path of molecules in the system and aid in reducing impurity content. The tested recipes are shown in table 5.1. As a control, the 350C_STD recipe was replicated from Diaz-Botia et al. as its long-term stability in PBS had already been demonstrated [40]. To determine impurity content, we utilized fourier-transform infrared spectroscopy (FTIR). To obtain deposition rates, we ran each recipe for 10 minutes, then cleaved the wafer and measured the film thickness via cross-sectional SEM.

The full FTIR spectra of all samples is shown in Figure 5.1. We note that the relative C-H content and Si-H content between recipes is nearly identical, implying that by minimizing C-H content, we also can minimize Si-H content and vice-versa. From Fig. 5.2, we see that the 200C_STD recipe has the highest impurity content. Furthermore, the 350C_STD recipe has the second lowest impurity content. This relationship between the two recipes is in agreement with previous work [40]. We note that lower power and lower pressure does indeed reduce impurity content. Interestingly, we find that the lowest impurity content of recipes we tested were the 300C_LoPOW and 300C_LoPRES recipes, which also have the lowest deposition rates at roughly 37 nm/min corresponding to roughly 27 minutes per 1 μm on film. Diaz-Botia et al. demonstrated that 1 μm of a-SiC grown using the 350C_STD recipe was stable for over 62 days at 96 °C in saline (with the experiment ending prior to failure), implying that a-SiC films with low impurity content can be sufficient molecular barriers even at a thickness of 1 μm. Thus, the identification of a lower temperature recipe with even lower impurity content than the 350C_STD recipe is very encouraging.

[1]The precursors here were SiH_4 and CH_4. We use the same precursors in this work

[2]Here, the power refers to the RF power used in deposition for the Oxford PlasmaLab System 100 in the Marvell Nanofabrication Laboratory

Recipe Name	Chuck Temperature	Power	Pressure	Deposition Rate
350C_STD	350 °C	250 W	1.4 T	41.5 nm/min
300C_STD	300 °C	250 W	1.4 T	47.6 nm/min
300C_LoPOW	300 °C	100 W	1.4 T	37 nm/min
300C_LoPRES	300 °C	250 W	1.0 T	36.6 nm/min
250C_STD	250 °C	250 W	1.4 T	61.0 nm/min
250C_LoPOW	250 °C	100 W	1.4 T	41.3 nm/min
250C_LoPRES	250 °C	250 W	1.0 T	47.4 nm/min
200C_STD	200 °C	250 W	1.4 T	64.7 nm/min
200C_LoPOW	200 °C	100 W	1.4 T	52.6 nm/min
200C_LoPRES	200 °C	250 W	1.0 T	55.0 nm/min

Table 5.1: PECVD a-SiC recipes. Generator frequency was 81 MHz, SiH_4 flow: 7.5 sccm, CH_4 flow: 60 sccm, Ar flow: 500 sccm

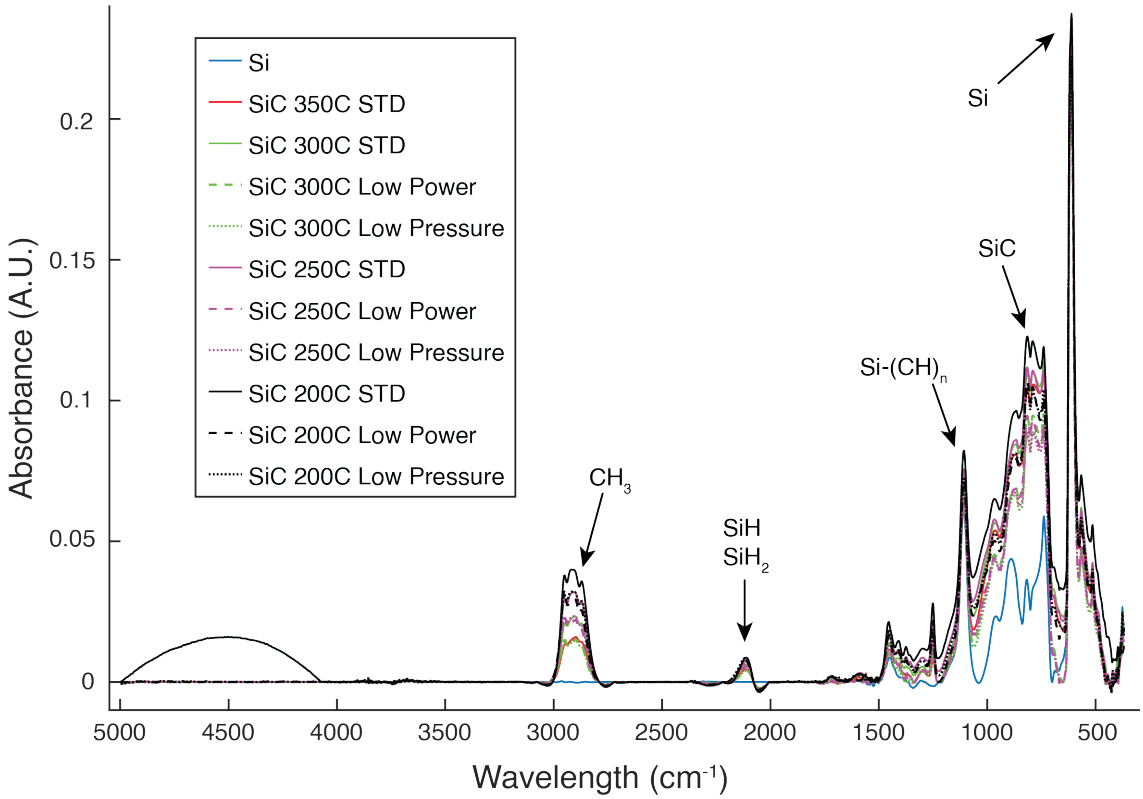

Figure 5.1: Full FTIR spectra of PECVD SiC recipes. We point out a few bands of interest: Si-Si (660 cm^{-1}), Si-C (790 cm^{-1}), Si-$(CH)_n$ (1100 cm^{-1}), Si-$H_{n,(n=1,2)}$ (2000-2200 cm^{-1}), C-H_2 (2890 cm^{-1}), C-H_3 (2960 cm^{-1}).

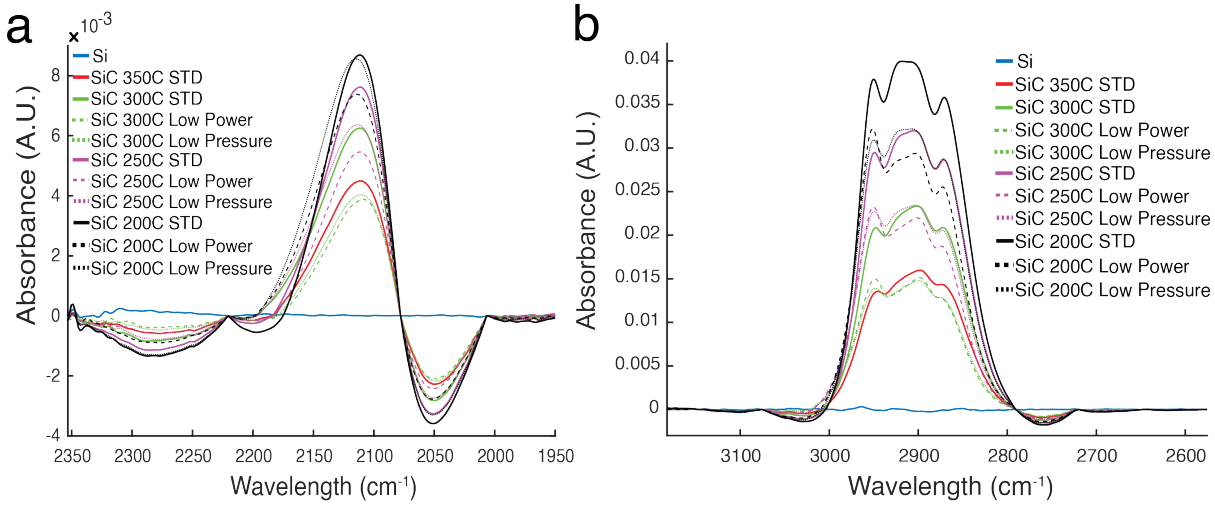

Figure 5.2: Impurity content of the tested PECVD recipes. Interestingly, Si-H (left) and C-H (right) impurity content increased or decreased together with the different recipes. As expected, the 200 °C recipes have the highest impurity content. We find that by reducing the power or the pressure, the impurity content decreases. As a consequence, we find that the 300 °C films have even less impurity content than the 350C_STD recipe, which was previously demonstrated to be stable for over 2 months in 96 °C PBS.

5.3 RFID as a readout for IC passivation

To determine if our encapsulation can protect ICs, we naturally require some feedback from the IC. In Chapter 3, we demonstrated this by removing the device from the RAA bath and measuring its IV characteristics (through ultrasonic backscatter amplitude) daily. While this works, it is very laborious, particularly when there are multiple devices, since our system cannot test devices in parallel. Similar to the idea presented in Chapter 4, we aim to develop a testing method that can be automated at scale.

While any chronic claim for a specific IC must be validated with that IC, as long as a candidate thin-film can protect a given IC for some duration of time, that length of time can be taken as an upper-bound and give some confidence to the encapsulation for generic ICs. To this end, we sought to simplify the testing protocol by using passive radio-frequency identification (RFID) ICs which could be interrogated at a distance, again through backscatter modulation. We imagine an RAA system in which multiple SiC-encapsulated RFID tags (IC + antenna) could be placed inside a heated saline bath with added ROS. Transmit coils would be placed outside the bath and automatically interrogate the tags and record the response. Each IC would have a unique ID, and upon query, would return a "dead-or-alive" signal. In this way, a large number of tags could be tested simultaneously.

f_r	10 pF	100 pF
13.56 MHz	13.8 μH	1.38 μH
f_r	80 pF	330 pF
125 kHz	20.3 mH	4.9 mH

Table 5.2: Ideal antenna inductances for typical on-chip tuning capacitances.

5.3.1 Antenna Design

There are three main frequency bands used by RFID tags: low-frequency (LF, 125 kHz), high-frequency (HF, 13.56 MHz), and ultra-high frequency (UHF, 900 MHz). The attenuation of EM signals in aqueous media increases with frequency; thus, low-frequency or high-frequency RFID were preferable to ultra-high frequency RFID[3]. While this relationship between EM attenuation and frequency would make low-frequency RFID seem like the most attractive choice, the trade-off of a low-frequency system implies a larger antenna which is non-ideal.

The resonance frequency of an RFID system can be computed by:

$$L_{ant}C_{tun}(\omega_{res})^2 = 1 \tag{5.1}$$

Where L_{ant} is the inductance of the antenna, C_{tun} is the tuning capacitance, and ω_{res} is the angular resonance frequency.

To make the simplest and smallest tag possible, we wanted to avoid needing any more components other than the RFID IC and the receive antenna. Thus, we were limited to the on-chip capacitance. Typical values for on-chip tuning capacitance for 125 kHz RFID chips ranged between 80 pF and 330 pF; typical values for 13.56 MHz RFID chips ranged between 10 pF and 100 pF, resulting in the following inductance ranges:

With a well-defined range of inductances, we can now explore antenna geometries to decide on the appropriate frequency range.

Planar circle antenna

The ideal inductance given by a circular antenna is:

$$L_{ant,circ} = \mu_0 N^{1.9} r \ln\left(\frac{r}{r_0}\right) \tag{5.2}$$

Where μ_0 is the vacuum permeability, N is the number of turns, r is the radius of the antenna, and r_0 is the width of the antenna track.

[3]At this frequency, the wavelength of the EM wave is roughly 30 cm. We found our UHF RFID reader had a read distance limit of around 20 cm, so in our case, even if we were to use UHF RF, we would still be in the inductive powering regime.

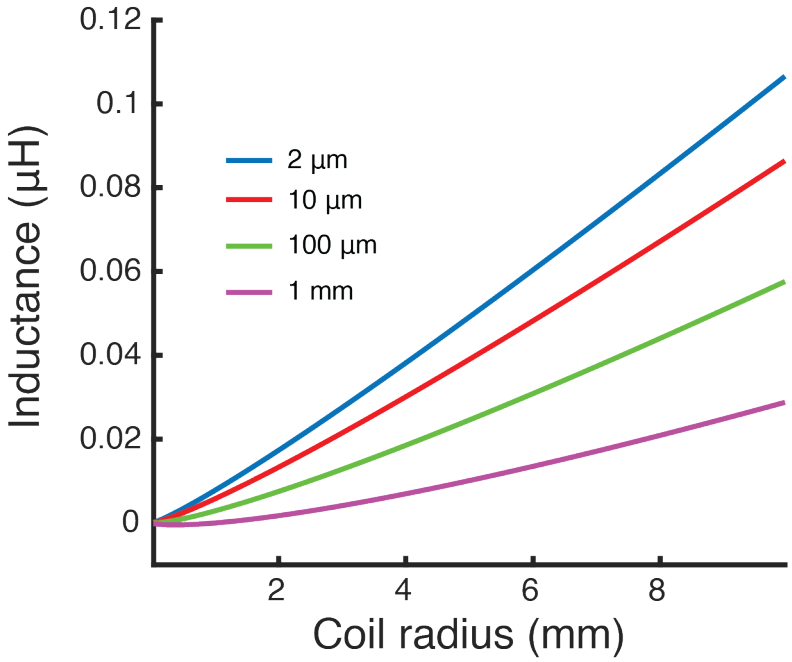

Figure 5.3: Ideal inductances for a single-loop circle antenna as a function of coil thickness and radius

Though this is the simplest architecture: a planar circle antenna can only have one loop, so $N = 1$. Plotting this for a variety of coil widths and radii shows that for a single loop, even with a 1 cm radii antenna, with the minimum loop width possible, we can only get an inductance of roughly 100 nH, which is far too low even for the HF antenna (Fig. 5.3).

Spiral antenna

We next examine the planar spiral antenna. The inductance of a planar spiral antenna can be calculated as:

$$L_{ant,spiral} = 31.33\mu_0 N^2 \frac{a^2}{8a + 11c} \tag{5.3}$$

Where

$$a = \frac{r_{in} + r_{out}}{2}, c = r_{out} - r_{in}$$

and μ_0 and N are the vacuum permeability and number of turns respectively.

Here, the turns are in-plane, so we can add an arbitrary number of turns, although it increases the overall size of our antenna. To see what the minimum antenna size can be, we choose the gap between coil arms to be 2 μm, which is the minimum gap easily patterned using conventional lithography In figure 5.5a we plot the ideal inductances as a function of turns and inductances. Additionally, we plot the total size of the antenna in figure 5.5b.

With a planar spiral coil, we find that we can build HF coils as small as 100 μm in diameter and LF coils as small as 1 mm in diameter[4].

Squared antenna

Finally, we example the planar "squared" antenna, which is similar to the spiral antenna, but is a series of nested square loops rather than circular loops. The ideal inductance is calculated as:

$$L_{ant,squared} = 2.34\mu_0 N^2 \frac{d}{1 + (2.75)p} \tag{5.4}$$

Where

$$d = \frac{d_{out} + d_{in}}{2}, p = \frac{d_{out} - d_{in}}{d_{out} + d_{in}}$$

and again, μ_0 and N are the vacuum permeability and number of turns respectively.

Once again, we plot the inductance as a function of turns and trace width (Fig. 5.5a). We also plot the total size of the coil as a function of turns and trace width (Fig. 5.5b). Here we again see that there exist regimes in which we can achieve the proper inductances, with similar sizes to circular spiral antennas.

Out-of-plane loop antenna

Let us revisit the circular-loop antenna, but allow it to be orthogonal to the chip so that we can increase the number of turns. Recalling equation 5.2, the inductance of our antenna increases with diminishing wire radius and increases with the number of turns. Thus, a thin wire can accommodate many turns without a significant increase in length. Assuming the thinnest wire we can attain and reliably work with is 25 μm gold wirebonding wire, we can replot equation 5.2 as a function of turns and loop radius.

We see that for inductances suitable for HF RFID, we easily reach the desired inductance within approximately 150 turns, even for an antenna with a very small loop radius. In the case of a 1 mm loop radius, only 29 turns are required, which, assuming the coil arms are thinly passivated (< 5 μm), would end up with a coil only 900 μm long. Thus, an out-of-plane loop antenna can give us high inductances while maintaining a small form factor.

Quality factor

In the previous sections we established that spiral loop antennas and spiral square antennas could both be used to create planar antennas for LF and HF RFID. However, we did not take quality factor (Q) into consideration, which describes how much energy the receive coil can harvest. The quality factor can be calculated by:

$$Q = \frac{2\pi f_{res} L}{R} \tag{5.5}$$

[4]We have not considered quality factor yet. For now, we are just trying to establish what geometries may work

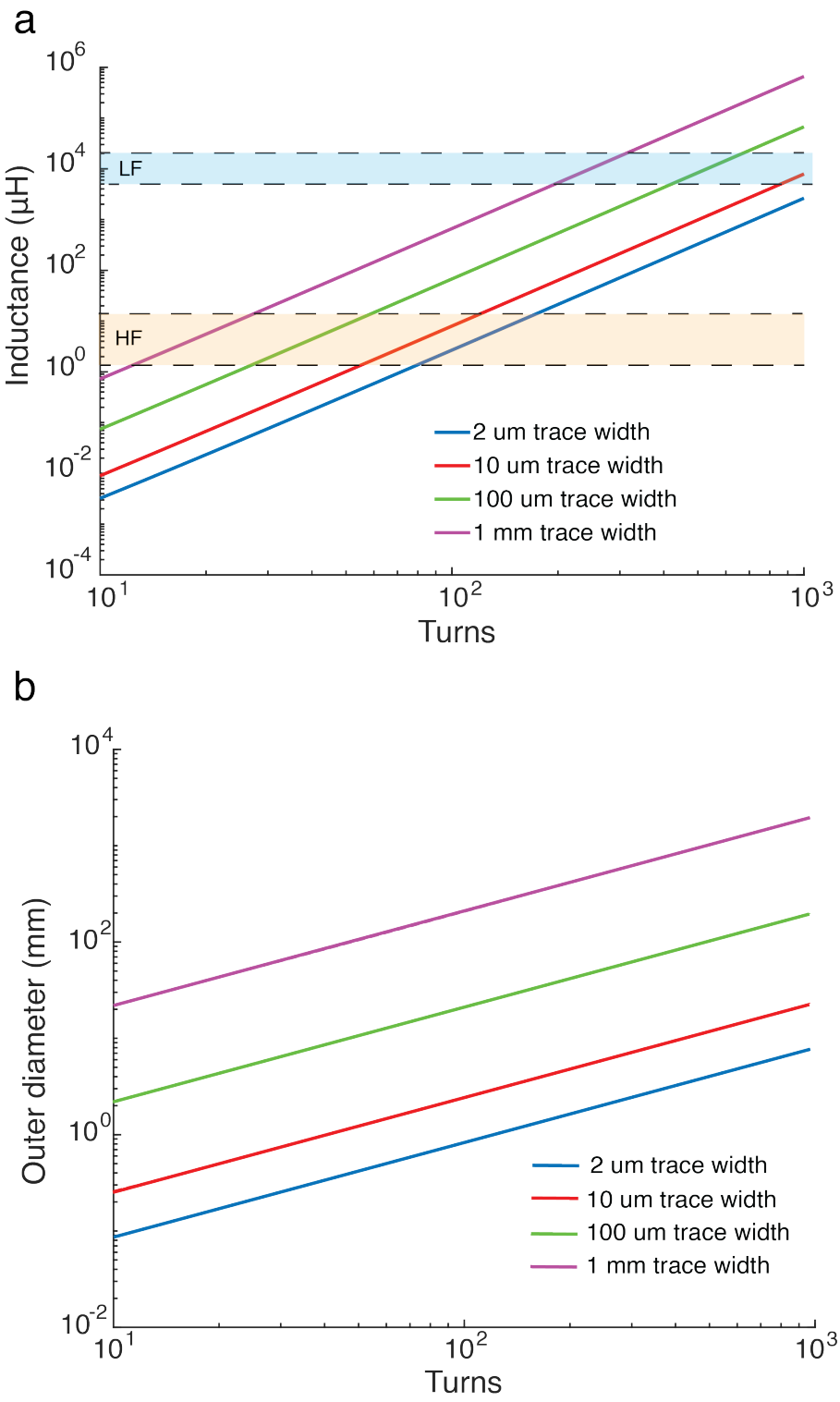

Figure 5.4: Spiral circular antenna a) inductances and b) outer diameters for a given number of turns and coil width.

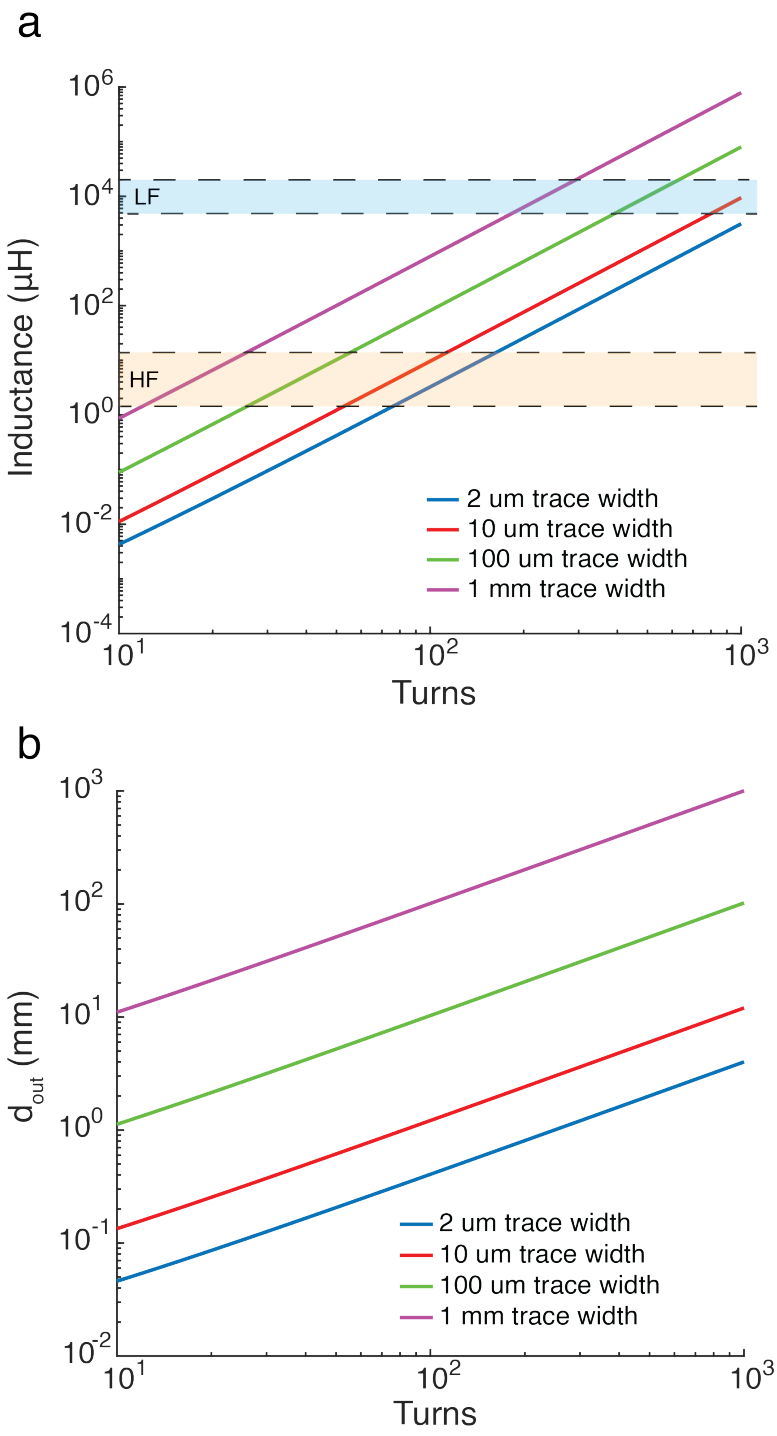

Figure 5.5: Spiral squared antenna a) inductances and b) outer diameters for a given number of turns and coil width.

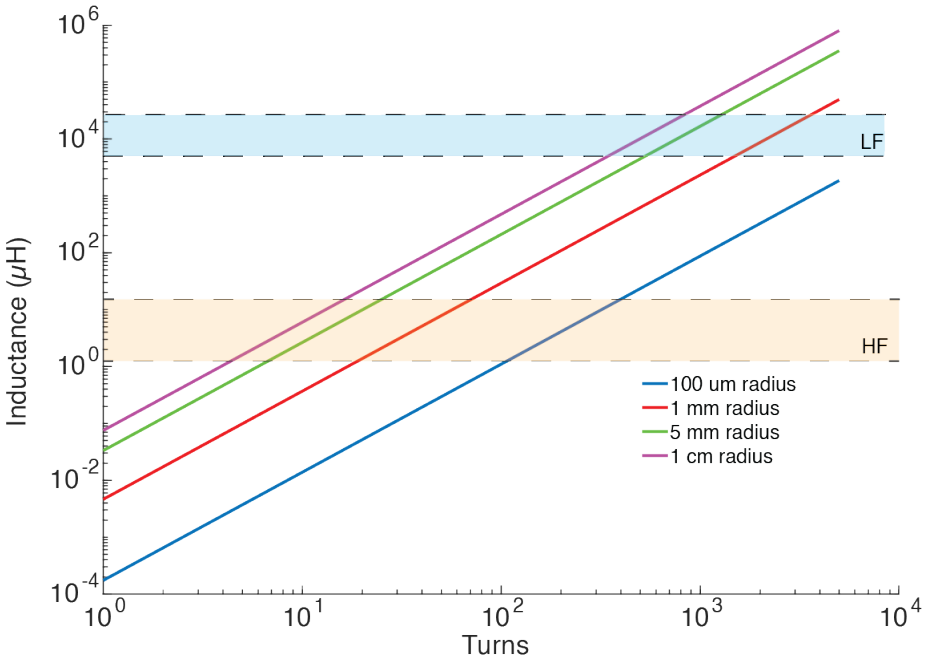

Figure 5.6: Inductances for circular loop antennas as a function of number of turns and coil radius. To get to inductances for HF RFID, we require between 10s and 100s of turns, whereas for LF RFID we require 100s to 100s of turns depending on loop radius. For this type of antenna, because we are able to extend into a third dimension, having a large number of turns does not necessarily increase the overall size of the coil significantly. For example, if coil wire is 10s of microns thick, 100s of turns only extends the coil into millimeter lengths.

where f_{res} is the resonance frequency of the coil, L is the inductance of the coil, and R is the resistance of the coil. The resistance of the coil is calculated by the well-known $R = \frac{\rho l}{A}$ where ρ is the resistivity of the coil material, l is the total length of the conductor, and A is the cross-sectional area of the coil.

As can be seen in equation 5.5, there exists a trade off between quality factor and antenna size. To obtain high inductances with smaller coils, we require more turns, which increases the total path length of the coil and increases the resistance. To illustrate this, let us consider lithographically patterned spiral antennas. The coil length, as a function of coil width, gap between coil arms, number of turns, and internal diameter is given for a circular spiral antenna as:

$$l_{spiral,circ} \approx \pi N(d_{in} + (w+g)(N-1)) \tag{5.6}$$

and for a square spiral antennas as:

$$l_{spiral,square} = 4Nd_{in} + 4N^2w + (4N^2 - 4N - 1)g \tag{5.7}$$

Circular Spiral Antenna							
d_{in} (μm)	w (mm)	g (μm)	N	d_{out} (mm)	l_{total} (cm)	R (Ω)	Q
4	0.1	2	35	7.34	38	63.8	3.67
4	1	2	16	34.1	80	13.4	17.5
4	1.5	2	14	45	92.5	11.2	21
Square Spiral Antenna							
d_{in} (μm)	w (mm)	g (μm)	N	d_{out} (mm)	l_{total} (cm)	R (Ω)	Q
4	0.1	2	19	10	72.5	24.4	9.64
4	1	2	15	16	90	15.1	15.5
4	1.5	2	13	21	101	11.3	20.8

Table 5.3: Calculated quality factors for spiral antenna geometries. Design parameters assume conventional lithographic patterning and 1μm of thin-film copper as a coil material. Target inductance is roughly 2.7 μH, which is appropriate for HF RFID. From these results, we see that Q and size are correlated.

Assuming a copper coil 1 μm thick ($\rho_{Cu} = 1.38 \cdot 10^{-8}$ Ω-m), we tabulate the quality factors for various antenna geometries in Table 5.3.

5.3.2 Antenna Fabrication

Based on these results, we decided to utilize HF RFID to minimize antenna size without significantly compromising transmission efficiency through aqueous media. We obtained HF RFID ICs with an on-chip tuning capacitance of roughly 50 pF. To achieve a resonance frequency of 13.56 MHz, a roughly 2.7 μH antenna is required. We built prototypes of both in-plane antennas as well as out-of-plane loop antennas. To test the antennas, we attached an IC to a PCB and wirebonded contacts between the antenna terminals of the IC and the PCB. Copper clips were soldered into the PCB vias so that antennas could quickly be swapped out. We found that the PCB set up did not add a significant amount of parasitic capacitance relative to the 50 pF tuning capacitance of the chip.

In-plane spiral antennas

A major challenge for in-plane spiral antennas is that the antenna terminals are far from each other. To close this distance, we considered a 3-mask microfabrication process in which the antenna layer is patterned on a glass wafer and then passivated with a layer of SiO_2. Vias to the terminals would could then be opened in the passivation layer, and interconnects bridging the antenna terminals and the IC footprint could then be sputtered over the SiO_2 passivation layer. However, for expediency, we decided to perform proof-of-concept tests using a commercially fabricated coil utilizing photochemical machining (PCM) to create

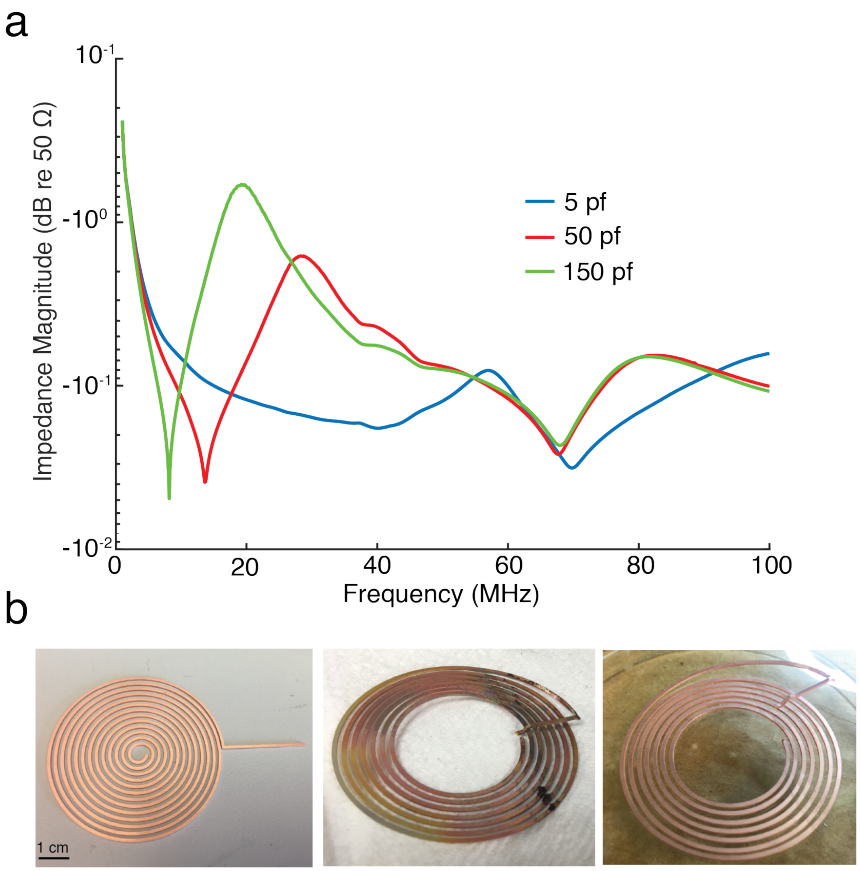

Figure 5.7: Copper circular planar spiral coils made via photochemical machining. a) Impedance spectra of the coils using a discrete capacitor. As expected, we see that larger discrete cap values decreases the resonance frequency. With a 50 pF discrete capacitor, we are able to get a resonance frequency around 13.56 MHz for HF RFID. b) Left: the copper coil as obtained by PCM. Center: the coil after tuning, forming, and annealing. Note the discoloration due to oxidation in the anneal step. Right: the coil after copper oxide strip in glacial acetic acid.

copper in-plane spiral antennas. Here, we envisioned creating circular spiral antennas with a "stem" extending from the exterior terminal so that the terminal could be folded across the antenna to meet the interior terminal.

We designed three version of the antennas out of 0.625 mm thick copper. The coils varied in their track width, between 0.5 mm, 1 mm, and 1.5 mm. The spacing between coil arms for all coils was 800 μm. The coils were designed to have slightly more inductance than required so that they could be trimmed as needed to the proper inductance.

Figure 5.7a shows the measured impedance spectra of a spiral antenna coil with discrete

capacitors of various values. We see that with a 50 pF discrete capacitor (same as the tuning capacitance of the chip) we get the proper resonance frequency around 13.56 MHz. As expected, by varying the value of the discrete capacitor, we are able to push the resonance frequency higher or lower.

To prepare the coil for flip-chip bonding, we carefully folded the stem with a pair of pliers, and utilized an anisotropic conductive film (ACF) thermocompression bonder to apply pressure and heat to flatten and planarize the stem terminal relative to the external terminal. Heating the coil was require to partially anneal it, so that the residual stress of the coil did not restore the stem to its original position. Painter's tape and a glass slide were used to hold the coil in the correct shape during the thermocompression and annealing. To remove the oxide incurred by annealing in an ambient environment, post-anneal, we cleaned tape residue off the coil by sonicating the coil in acetone for 5 minutes, followed by an IPA and DI water rinse[5]. We then etched away the copper oxide by soaking the coil for 1 hour in glaical acetic acid (Fig. 5.7b). Finally, to prepare the coil for bonding, we attached the coils to a 6" dummy wafer with photoresist[6], and 300 nm of Au is evaporated onto the coils with a 10 nm Ti adhesion layer. Finally, the coils are removed from the wafer and soaked in acetone overnight to remove any photoresist residue.

Out-of-plane loop antennas

To reduce antenna size, we also built both solenoid and toroidal loop antennas with both air-cores as well as magnetic-cores. As a first pass, we utilized fluoropolymer-coated 75 μm Ag wire so that the coil arms could be pushed tightly against each other without shorting. For air-core solenoids and toroids, we used the end of a glass pipette and plastic tubing of various diameters to wrap the wire around. For magnetic-core solenoids and toroids, we purchased NiZn ferrites. While other magnetic cores could be used, ferrite cores can withstand high temperature processing and NiZn cores are less lossy than MnZn cores at frequencies above 10 MHz.

After constructing each antenna, we tested their efficacy by measuring their impedance spectra and measuring their maximum read distance in air. We tabulate some of our results comparing antenna design and read distance in Table 5.4.

In figure 5.8 we show some examples of these antennas and provide their impedance spectrum. We show that using a ferrite core, we are able to build an antenna with a 1 mm diameter and 5 mm long. We show the read distance of this antenna in air is 7 mm, which is comparable to a much larger antenna with an air core.

Finally, to ensure that our 1 mm x 5 mm antenna will work an aqueous environment, we built a small chamber out of PDMS, and filled it with PBS. The antenna was placed in the reservoir and connected to a PCB with a wirebonded IC. The chamber was then placed over

[5]This step can be skipped if desired, but we found that the tape residue could mask the copper oxide and caused the copper oxide etch to require an overnight soak rather than a 1 hour soak

[6]The photoresist is first spun, then the coils are placed on the photoresist prior to bake. Once the coils are placed on the wafer, the photoresist is hard baked

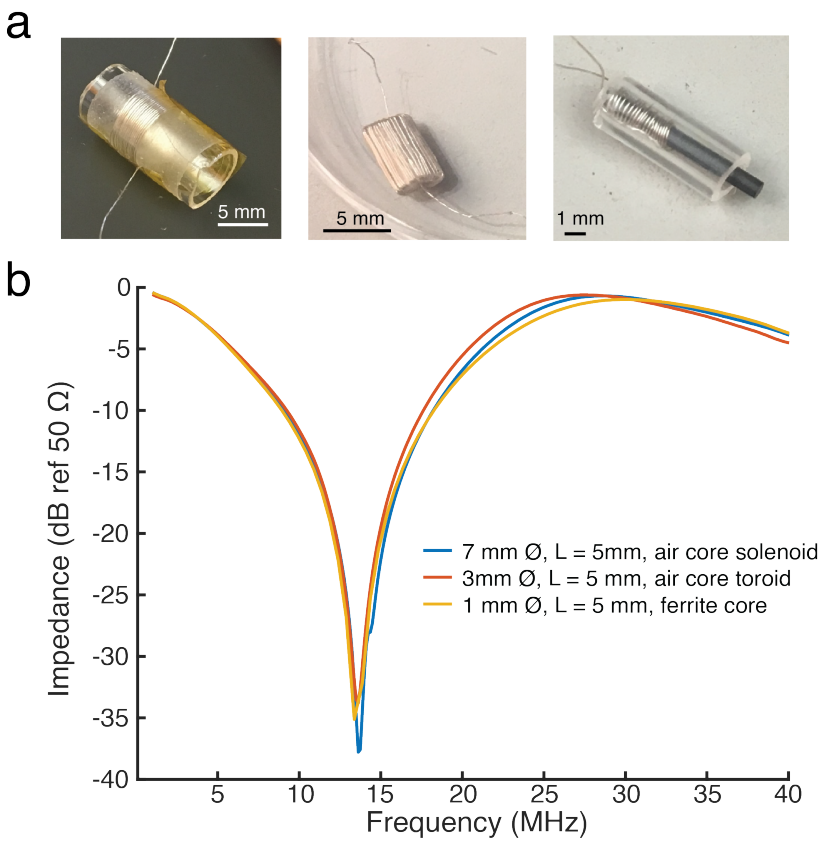

Figure 5.8: Solenoid and toroid coils. a) Example coils. From left to right: a 7 mm diameter air-core solenoid, a 4 mm diameter air-core toroid, a 1 mm diameter ferrite core solenoid. As can be seen, the toroid coil requires a significant number of turns, whereas the solenoid coils require less than 30 each. A piece of tubing is slid over the 1 mm x 5 mm coil to keep its shape, otherwise the coil springs out. b) Impedance spectra of the three coil in a). As expected, the larger air-core solenoid coil has a lower impedance than the smaller solenoid or the toroid.

Type	Core	Dimensions	Read Distance
Toroid	Air	4 mm ⊘ x 5 mm	3 mm
Toroid	NiZn Ferrite	10 mm ⊘ x 3 mm	< 1 mm
Solenoid	Air	7 mm ⊘ x 5 mm	1.2 cm
Solenoid	NiZn ferrite	4 mm ⊘ x 3 mm	1 cm
Solenoid	NiZn ferrite	1 mm ⊘ x 5 mm	7 mm

Table 5.4: Read distances for select circular antenna designs. In general, we find that solenoid coils have better read distance than toroidal coils and coils with ferrite cores can be made significantly smaller than their air-core counterparts without significantly affecting their read distance.

an interrogator. The chamber floor was 1 mm thick so that the receive and transmit coils were as close as possible. The impedance spectra of the submerged antenna and discrete chip is shown in figure 5.9.

The impedance of the antenna in PBS is slightly lower than that in air, but not significantly so. Upon interrogation, we were successfully able to read the ID of the chip and the ID of the chip in PBS was the same as that in air. Based on these results, we felt confident that the 1 mm x 5 mm antenna would be appropriate for our RFID tags.

5.3.3 IC Temperature Compatibility

We sought to experimentally verify the temperature budget of the IC in use in order guide our process development. To do this, we placed ICs into alumina leadless chip carriers (LCC) with conductive Ag epoxy and wirebonded the IC pads to the internal pads of the LCC. We confirmed that the IC was working by attaching a 6 mm diameter air-core solenoid antenna to the package and interrogating it. Next, we heat-treated the IC at various temperatures and various times, then re-interrogated the IC with the same solenoid antenna to confirm if the chip still operated.

From the results in Table 5.5, we see that the chip appears to be capable of surviving up to 300 °C processes for several hours. For ICs that survived heat treatment, we did not note a significant change in impedance spectra. Further testing should be done to confirm that the heat-treated samples do not suffer from reduced read range and what the maximum duration an IC can tolerate for a given temperature. Nevertheless, these results are encouraging, as they suggest that these ICs can handle process temperatures up to 300 °C, which allows for the deposition of low-impurity content SiC.

5.3.4 Flip chip integration

As discussed in chapter 3, wirebonding limits the minimum footprint for IC integration due to the need for target pads and the space required between the target pads and the

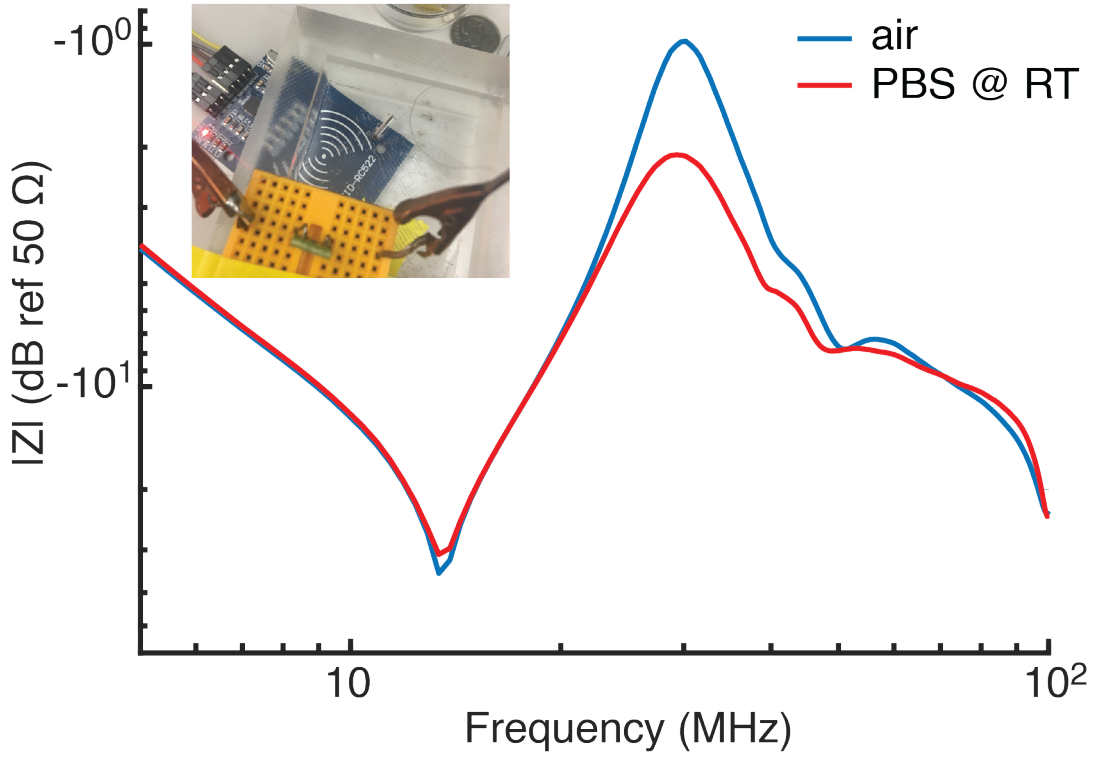

Figure 5.9: Coil tests in PBS. We submerged our 1 mm x 5 mm ferrite-core solenoid coil in a PDMS reservoir filled with PBS to test its ability to read in an aqeuous environment. To improve coupling as much as possible, the reservoir thickness was only 1 mm (inset). We were able to successfully read the chip in solution. We found the impedance spectra of the antenna was only slightly decreased by submersion in PBS.

IC for the wirebonder head. Furthermore, the wirebonds themselves can add parasitics and require a "glob top" polymer encapsulation (generally epoxy) for mechanical stability. Flip chip bonding, on the other hand, reduces the footprint requirements to simply the size of the chip. In this method, metal bumps are formed over the chip pads and then can be joined to a metallized substrate by soldering, Au-Au thermocompression bonding, eutectic bonding, or any other conductive bonding technique.

From the standpoint of building a medical implantable, we chose to develop a flipchip bonding process using Au-Au thermocompression due to the well established biocompatibility of Au. To develop our flipchip bonding process, we created dummy targets by blanket evaporating 300 nm Au over a Si wafer using a 10 nm Ti adhesion layer. We used a 0.5 mm x 0.5 mm square pick-up tool on the flipchip bonder to pick up the chip and place it on the sample. We varied bonding temperature, duration, and applied force. To qualitatively evaluate the fitness of the bond, we sheared the chip from the sample post-bonding and

Temperature	Time	Method	Read
150 °C	30 min	Oven	Yes
200 °C	1 hour	Oven	Yes
200 °C	2 hours	Oven	Yes
200 °C	3 hours	Oven	Yes
250 °C	2 hours	Hot plate	Yes
250 °C	4 hours	Hot plate	Yes
300 °C	30 minutes	Hot plate	Yes
300 °C	2 hours	Hot plate	Yes
330 °C	1 hour	Benchtop Furnace	No

Table 5.5: Temperature stress test for HF RFID IC. Due to the temperature range, several different heating sources were used. The "read" column refers to whether the IC could still respond with its address when interrogated post-heat treatment.

inspected the mating surfaces.

Figure 5.10 show the results of our flipchip bonding tests. Figure 5.10a shows that the chip cracks after exceeding 15 N of force, which set an upper-bound on force. The upper-bound on temperature is 300 °C, as determined by the temperature budget experiments performed in section 5.3.3. We determined that bonding at 275 °C with 15 N of force for 10 minutes resulted in successful bonds and performed flip chip bonding tests on both our planar copper coils and bare gold wire.

5.3.5 Low-cost multiplexed RFID interrogator

To build our interrogator, we used an Arduino Uno microcontroller with RFID reader, real-time clock, and SD card modules (Fig. 5.11). Briefly, the operation of the interrogator is as follows: first, a .txt file is created, opened, and the current date is pulled from the real-time clock module. Next, the interrogator sequentially powers each RFID reader to interrogate the nearest tag. If a tag is found, the tag reports its identity, and the identity of the tag is then written to the open text file on the SD card. An indicator LED then turns on to indicate the presence of the tag and the next RFID reader is then toggled on. If a tag is not found, the RFID reader without a tag is noted as missing in the text document and the indicator LED is turned off. The interrogator then turns off and wakes up again after a predetermined time. This loop continues indefinitely until the Arduino is powered off. Arduino code is available in Appendix B.

Due to the limited number of I/O pins on the Arduino UNO, we were able to connect a maximum of four RFID readers to a single Arduino. However, expanding the number the available I/O pins on Arduino is a straighforward task with many commercial options (such as the Microchip MCP23S17). Additionally, the total cost for all the components is less than

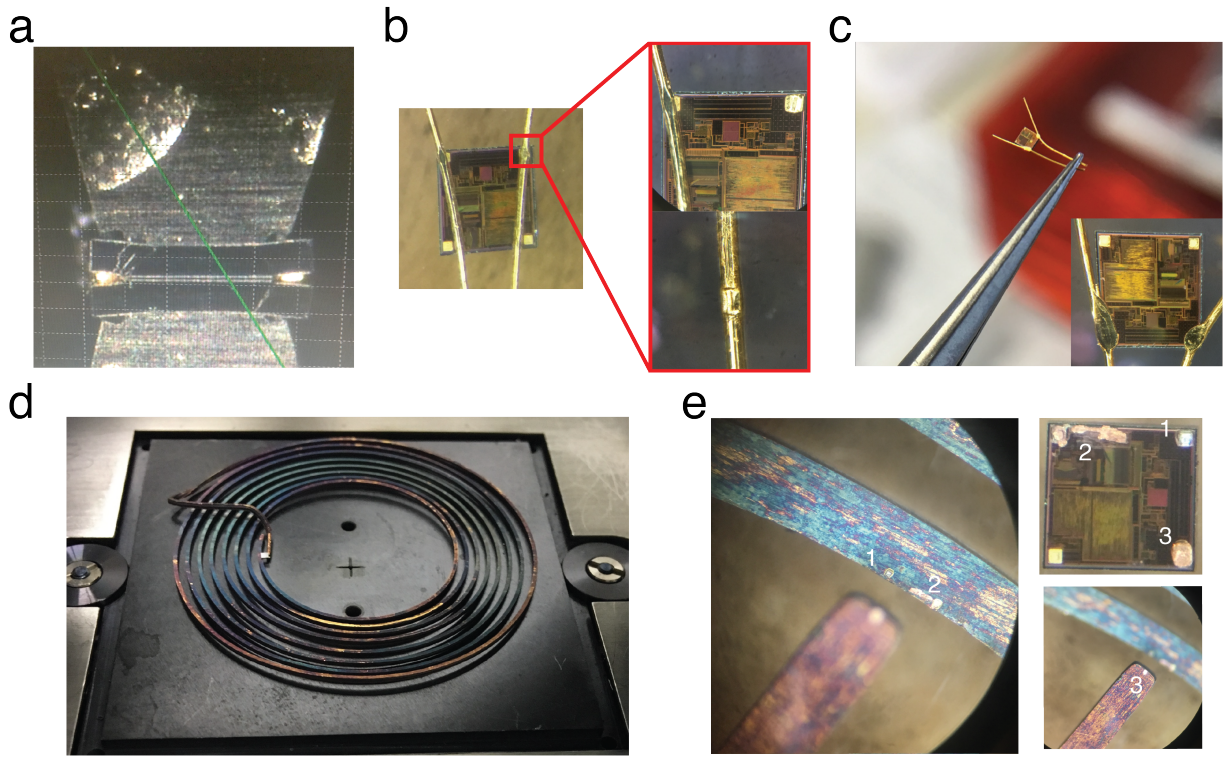

Figure 5.10: Flip chip processing. a) A side profile of the IC cracking during bonding due to excessive force (20 N). b) An example of a chip with one successful bond (left) and one unsuccessful bond (right). The unsuccessful bond has not deformed as much as the successful bond. Furthermore, when sheared apart, it is clear that no bonding has occurred since the wire simply has deformed to accommodate the pad. c) proper bonding to 75 μm gold wire. Inspection of the bond joints indicates that the god reflowed significantly during bonding, indicating successful Au-Au thermocompression bonding. d) Example of an IC flip chip bonded to a spiral planar coil. Note that even though the coil had been coated with Ti/Au, discoloration of the coil seems to inddicate oxidation of the underlying Ti or Cu. e) Photos of the a planar spiral coil post IC removal. Proper bonding has taken place, as parts of the mating surfaces can be seen on the chip and the coil. The location indicated by "1" shows the entire pad metallization of the IC has delaminated off the IC and is stuck on the coil. In "2" we see the gold coating of the coil has been pulled off the coil and is stuck on the chip. We see a similar behavior in "3". The image on the bottom right is simply the image on the left in a different focal plane to better show the surface of the coil.

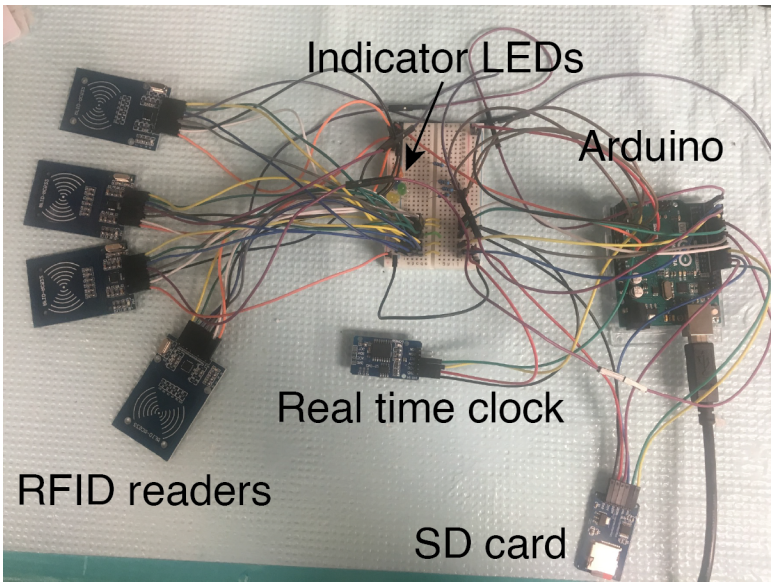

Figure 5.11: Arduino based interrogator. Up to four RFID readers can be attached to the Arduino at once. The real time clock module is used to keep track of the date. The Arduino sequentially queries each reader in search of an RFID tag. If a tag is found, it responds with its ID, and an indicator LED lights up. Else, the light is toggled off. The ID of the tag is written to a text-file saved on the SD card.

40 dollars, so building multiple interrogators is a reasonable path to scale up device testing.

5.4 Future Work

Due to the 2020 COVID-19 epidemic, this project unfortunately remains unfinished. While there are still a number of tasks left to be solved, with the framework established above, the tasks are fairly straightforward.

First, while we have surmised a-SiC film stability as a function of impurity content, this claim must be rigorously tested. In particular, a relationship between film content, film thickness, and biostability must be determined. Additionally, we are interested if sequential a-SiC depositions can provide greater biostability than a single a-SiC deposition for a given thickness (i.e. a single 5 μm deposition versus 5 1μm depositions) by decorrelating impurities. This could enable lower temperature a-SiC deposition, since the a-SiC encapsulation step is currently the highest temperature step. Fortunately, the relationship between all these factors and film stability can be simultaneously tested by the system described in Chapter 4.

Next, the full assembly of the SiC encapsulated RFID tag must be done. We have developed a process flow for both building the antenna as well as bonding the antenna to the

IC, but we have not yet built the full tag. The biggest challenge is the material restrictions imposed by the PECVD chambers. In this work, two PECVD tools were available to us: one chamber for a-SiC deposition and strict materials restrictions; and a second chamber which does not support SiC deposition, but does support a variety of other silicon-based dielectrics such as SiO_2 and Si_xN_y. No polymers are allowed in either chambers due to the potential outgassing which could contaminate them. Exposed metals are also not allowed in the a-SiC PECVD chamber, but are permissible if buried. The other chamber, however, does allow for exposed metals. As a consequence of these restrictions, the fluorocarbon insulated wire we were using previously is not compatible with the PECVD process. To circumvent this, we suggest first winding the antenna with bare wire loosely, such that the coil arms are not shorting together. Next, we a thin layer (1μm) of SiO_2 can be deposited via PECVD to insulate the coil arms, and the coil can be compressed to reduce the size of the coil without shorting. Note that the inductance will increase with turn density, so the SiO_2 on the ends of the coil should be stripped way and the antenna retuned. Once the coil has been compressed and re-tuned, a second thicker SiO_2 deposition ($> 3\mu$m) can be made to "glue" the coil to the ferrite and hold its shape. Once again, the ends of the coil should be stripped of their encapsulation and the IC can then be flipchip bonded to the antenna using the process described in section 5.3.4. One final SiO_2 layer should be deposited to bury all exposed metals; in this case a thin SiO_2 layer ($< 1\mu$m) is sufficient. Finally, the SiO_2 coated tag can then be coated in a-SiC. To ensure full coating of the tag, the tag both the final SiO_2 deposition and a-SiC deposition should be done on both sides of the tag. A pocket wafer can be used to facilitate transfer of the tag in and out of the PECVD chambers. Alternatively, Jeong et al. utilized a wire mesh bag to conformally coat their ICs and a similar approach could be taken for this work [70].

Finally, the RAA system must be finished, but this is straightforward as the interrogator has already been implemented and read through PBS has been verified. A system similar to that presented in Chapter 4 can be used to maintain bath properties. The magnetic permeability of the ferrite may change slightly at elevated temperatures and the RFID reader module and IC are not designed to operate above 85 °C. This sets an upper-bound on the bath temperature and heat sources must be some distance from the interrogator. If desired, anti-collision protocols on the transmitter side could be implemented to increase the number of tags that a single RFID reader can communicate with.

5.5 Conclusion

In this chapter, we described efforts to identify an IC-compatible a-SiC recipe for chronic encapsulation. We also detailed design considerations and assembly processes to build a test system for a-SiC encapsulated HF RFID implants. Although the work remains uncompleted for now, we highlight and outline remaining tasks and steps to finish them. Development and verification of a long-lived IC-compatible a-SiC process would greatly facilitate clinical translation of wireless microscale IMDs of any type.

Chapter 6

Future Directions and Conclusion

Ceramic materials have great potential in the packaging of neural implants due to their biocompatibility, corrosion resistance, RF transparency, and tunable dielectric properties. Although bulk ceramic can be difficult to shape and can be prone to cracking, thin-film ceramics are not as susceptible to these issues. Metals and polymers will continue to have a central place in the packaging of IMDs but there is no doubt that both bulk and thin-film ceramics will play a critical role in packaging for contemporary and future devices. The use of alumina feedthroughs will remain an essential component of non-miniaturized IMDs, as they currently are in cochlear implants, deep-brain-stimulation systems, and more. Microfabricated implants will also benefit from ceramic materials as the search for a thin-film hermetic encapsulation material continues. Before we conclude, we will discuss one more unique application of ceramics.

6.1 Seamless Ceramic Interfaces

It is well known that many packaging failure modes occur at interfaces of dissimilar materials; though Joshi-Imre et al. demonstrated that a-SiC encapsulated Utah electrode arrays did not show evidence of dissolution or cracking in the encapsulation layer (in contrast to parylene), delamination of the a-SiC was one failure mode of the implanted arrays [74]. Unfortunately, heterogenous interfaces are unavoidable if feedthroughs are required. This failure point has been long recognized. For example, horizontal interconnects with vertical feedthroughs have been used to try to enhance hermiticity by increasing the length of the leakage path [62]. However, as conductor density increases within feedthroughs, ensuring hermiticity becomes more difficult as a single leak will result in a compromised device. Furthermore, miniaturization of devices will inevitably result in shorter leakage paths, increasing the risk of water vapor ingress.

A part of this chapter is adapted from an unpublished manuscript: "Ceramic Packaging for Neural Implants" by K. Shen and M. M. Maharbiz

Ceramic materials can provide a unique solution to this issue, in that some ceramics can be doped to vary the material from insulator to conductor. This raises the possibility that a feedthrough can be made of the same material, doped differently. Both penetrating and surface neural probes have been fabricated in all-SiC processes. Diaz-Botia et al.'s thin film SiC ECoGs utilized amorphous SiC as both the substrate and the encapsulation layer with n-SiC recording sites and demonstrated electrical recordings of compound action potentials in the rat sciatic nerve [41]. While complete device aging was not demonstrated in that work, the a-SiC thin film itself was aged in a benchtop reactive accelerated aging test and shown to be a superior encapsulation material to thermally grown SiO_2. The Saddow group at the University of Southern Florida has also been exploring all-SiC neural probes using crystalline SiC [10, 11]. In that body of work, n-type crystalline SiC substrates were used and p-type crystalline SiC interconnects were created to form reverse-biased diodes between interconnects for electrical isolation; a-SiC layer was used for encapsulation. While in-vivo results have not yet been demonstrated with these devices, the use of a homogenous material for all parts of the implant should greatly improve reliability.

Diamond is another ceramic material that can exist in both insulating and conductive forms as PCD and nitrogen-doped ultra nano-crystalline diamond (N-UNCD), respectively. Ganesan et al. have utilized this property to create all-diamond feedthrough arrays for retinal prostheses by starting with a PCD substrate and then growing N-UNCD electrodes on top of it [53, 134]. These feedthroughs have been demonstrated as hermetic and biocompatible. However, the chemical inertness of diamond makes it very difficult to etch, and laser machining was used to pattern both the PCD and the N-UNCD, making scalability difficult. Nevertheless, there is much promise in the general principle of seamless neural interfaces, enabled by ceramic materials.

6.2 Conclusion

In this dissertation, we examined the role of ceramics in IMD packaging. In **Chapter 1** we motivated the development of novel ceramic packaging paradigms for long-lived miniaturized wireless IMDs and summarized classical methods and applications of ceramics in medical devices. In **Chapter 2**, we introduced ultrasonic wireless power transfer as a highly efficient modality for millimeter-scale wireless implants. We developed models for ultrasonic propagation allowing us to identify structures which permit use of ultrasonic power transfer for ceramic and metal housing with high efficiency. In **Chapter 3**, we utilize the transmission models developed in Chapter 2 to design, assemble, and characterize an alumina-titanium package for an ultrasonically-coupled, battery-less, IMD for electrophysiological sensing. We succeed in our intention to demonstrate wireless powering and communication through the package via ultrasound, although we note that our package design does not significantly enhance lifetime over polymeric packaging due to micro-cracks induced by laser welding. In **Chapter 4**, we discuss limitations of microscale "impermeable envelope" style packaging and motivate the use of thin-film encapsulation. We then build a system to rapidly evaluate

the suitability of thin films for chronic encapsulation, in which we confirm the improved stability of a-SiC thin films over thermally grown oxide thin films. Finally, in **Chapter 5** we describe our efforts and outline a path towards developing and testing chronic a-SiC thin films for packaging ICs, which could enable clinical translation of highly sophisticated and miniaturized wireless IMDs.

Taken together, this body of work reveals the many exciting applications of ceramics as an encapsulation material for chronic implants and looks towards emerging applications enabled by modern processing techniques. Although a great deal of work remains to be done, we are optimistic about the development of long-lived implantable microsystems for bioelectronic medicine.

6.2.1 Specific Contributions of this thesis

This dissertation describes the work completed in the following publications:

- Shen, K. and Maharbiz, M.M., 2019, March. Ceramic Packages for Acoustically Coupled Neural Implants. In 2019 9th International IEEE/EMBS Conference on Neural Engineering (NER) (pp. 847-850). IEEE

- Shen, K. and Maharbiz, M.M., 2019. Design of Ceramic Packages for Ultrasonically Coupled Implantable Medical Devices. IEEE Transactions on Biomedical Engineering.

In these works, I derived transmission models for bulk and flexural mode ultrasound propagation. I designed and developed custom packages and an assembly method to package an ultrasonically-coupled implant for electrophysiology using backscatter communication. I designed and performed experiments to characterize power harvesting, communication, and longevity. I also wrote code to analyze the data (see appendix).

- "An Automated System for Reactive Accelerated Aging of Implant Materials with In-Situ Testing." Shen, K., Yau, A., Panchavati, S., and Maharbiz, M.M., 2020. (accepted at 42nd Annual International Conference of the IEEE Engineering in Medicine and Biology Society

In this work, I designed and built a system for reactive accelerated aging. I designed and performed experiments to characterize the temperature and H_2O_2 concentration of the system. I prepared test samples, performed experiments, and analyzed data to verify the validity of the system.

Bibliography

[1] AI Abdulagatov et al. "Al2O3 and TiO2 atomic layer deposition on copper for water corrosion resistance". In: *ACS applied materials & interfaces* 3.12 (2011), pp. 4593–4601.

[2] Simeon Agathopoulos et al. "Interactions at zirconia-Au-Ti interfaces at high temperatures". In: (2002).

[3] RV Allen and WE Borbidge. "Solid state metal-ceramic bonding of platinum to alumina". In: *Journal of Materials Science* 18.9 (1983), pp. 2835–2843.

[4] E Ajith Amerasekera and Farid N Najm. *Failure mechanisms in semiconductor devices*. Wiley New York, 1997, p. 270.

[5] Nicholas V Apollo et al. "Brazing techniques for the fabrication of biocompatible carbon-based electronic devices". In: *Carbon* 107 (2016), pp. 180–189.

[6] Jordan P Ball et al. "Biocompatible evaluation of barium titanate foamed ceramic structures for orthopedic applications". In: *Journal of Biomedical Materials Research Part A* 102.7 (2014), pp. 2089–2095.

[7] James C Barrese et al. "Failure mode analysis of silicon-based intracortical microelectrode arrays in non-human primates". In: *Journal of neural engineering* 10.6 (2013), p. 066014.

[8] Hamid Basaeri, David B Christensen, and Shad Roundy. "A review of acoustic power transfer for bio-medical implants". In: *Smart Materials and Structures* 25.12 (2016), p. 123001.

[9] Ingo Bauer et al. "Laser microjoining of dissimilar and biocompatible materials". In: *Photon Processing in Microelectronics and Photonics III*. Vol. 5339. International Society for Optics and Photonics. 2004, pp. 454–465.

[10] Evans K Bernardin et al. "Demonstration of a robust all-silicon-carbide intracortical neural interface". In: *Micromachines* 9.8 (2018), p. 412.

[11] Mohammad Beygi et al. "Fabrication of a Monolithic Implantable Neural Interface from Cubic Silicon Carbide". In: *Micromachines* 10.7 (2019), p. 430.

[12] Caroline K Bjune et al. "Package architecture and component design for an implanted neural stimulator with closed loop control". In: *2015 37th Annual International Conference of the IEEE Engineering in Medicine and Biology Society (EMBC)*. IEEE. 2015, pp. 7825–7830.

[13] Gabriele Bonaventura et al. "Biocompatibility between Silicon or Silicon carbide surface and neural Stem cells". In: *Scientific reports* 9.1 (2019), pp. 1–13.

[14] Lyudmila V Borovikova et al. "Vagus nerve stimulation attenuates the systemic inflammatory response to endotoxin". In: *Nature* 405.6785 (2000), pp. 458–462.

[15] David A Borton et al. "An implantable wireless neural interface for recording cortical circuit dynamics in moving primates". In: *Journal of neural engineering* 10.2 (2013), p. 026010.

[16] JLHR Bosch and J Groen. "Sacral nerve neuromodulation in the treatment of patients with refractory motor urge incontinence: long-term results of a prospective longitudinal study". In: *The Journal of urology* 163.4 (2000), pp. 1219–1222.

[17] Lyn Bowman and James D Meindl. "The packaging of implantable integrated sensors". In: *IEEE Transactions on Biomedical Engineering* 2 (1986), pp. 248–255.

[18] Leonid Brekhovskikh. *Waves in layered media*. Vol. 16. Elsevier, 2012, pp. 15–26.

[19] György Buzsáki. "Large-scale recording of neuronal ensembles". In: *Nature neuroscience* 7.5 (2004), pp. 446–451.

[20] J Cavuoto. "The market for neurotechnology: 2018–2022". In: *Neurotech Report* 1 (2018).

[21] Kichul Cha, Kenneth Horch, and Richard A Normann. "Simulation of a phosphene-based visual field: visual acuity in a pixelized vision system". In: *Annals of biomedical engineering* 20.4 (1992), pp. 439–449.

[22] Edward F Chang. "Towards large-scale, human-based, mesoscopic neurotechnologies". In: *Neuron* 86.1 (2015), pp. 68–78.

[23] Ting Chia Chang et al. "Design of tunable ultrasonic receivers for efficient powering of implantable medical devices with reconfigurable power loads". In: *IEEE transactions on ultrasonics, ferroelectrics, and frequency control* 63.10 (2016), pp. 1554–1562.

[24] Jayant Charthad et al. "A mm-sized implantable medical device (IMD) with ultrasonic power transfer and a hybrid bi-directional data link". In: *IEEE Journal of solid-state circuits* 50.8 (2015), pp. 1741–1753.

[25] Jun Chen et al. "Temperature dependence of piezoelectric properties of high-TC Bi (Mg 1/2 Ti 1/2) O 3–PbTiO 3". In: *Journal of Applied Physics* 106.3 (2009), p. 034109.

[26] Ritchie Chen, Andres Canales, and Polina Anikeeva. "Neural recording and modulation technologies". In: *Nature Reviews Materials* 2.2 (2017), pp. 1–16.

[27] Zhangwei Chen et al. "3D printing of ceramics: A review". In: *Journal of the European Ceramic Society* 39.4 (2019), pp. 661–687.

[28] Zhao Cheng et al. "Radiation efficiency of submerged rectangular plates". In: *Applied Acoustics* 73.2 (2012), pp. 150–157.

[29] Daniel J Chew et al. "A microchannel neuroprosthesis for bladder control after spinal cord injury in rat". In: *Science translational medicine* 5.210 (2013), 210ra155–210ra155.

[30] David B Christensen and Shad Roundy. "Non-dimensional analysis of depth, orientation, and alignment in acoustic power transfer systems". In: *Smart Materials and Structures* 27.12 (2018), p. 125013.

[31] MB Christensen et al. "The foreign body response to the Utah Slant Electrode Array in the cat sciatic nerve". In: *Acta biomaterialia* 10.11 (2014), pp. 4650–4660.

[32] Christian and Paul JA Kenis. "Fabrication of ceramic microscale structures". In: *Journal of the American Ceramic Society* 90.9 (2007), pp. 2779–2783.

[33] Jason E Chung et al. "High-density, long-lasting, and multi-region electrophysiological recordings using polymer electrode arrays". In: *Neuron* 101.1 (2019), pp. 21–31.

[34] Stuart F Cogan et al. "Plasma-enhanced chemical vapor deposited silicon carbide as an implantable dielectric coating". In: *Journal of Biomedical Materials Research Part A: An Official Journal of The Society for Biomaterials, The Japanese Society for Biomaterials, and The Australian Society for Biomaterials and the Korean Society for Biomaterials* 67.3 (2003), pp. 856–867.

[35] Camilla Coletti et al. "Biocompatibility and wettability of crystalline SiC and Si surfaces". In: *2007 29th Annual International Conference of the IEEE Engineering in Medicine and Biology Society*. IEEE. 2007, pp. 5849–5852.

[36] RN Correia, JV Emiliano, and P Moretto. "Microstructure of diffusional zirconia–titanium and zirconia–(Ti–6 wt% Al–4 wt% V) alloy joints". In: *Journal of materials science* 33.1 (1998), pp. 215–221.

[37] A De Paris, M Robin, and Gilbert Fantozzi. "Welding of ceramics SiO2-Al2O3 by laser beam". In: *Le Journal de Physique IV* 1.C7 (1991), pp. C7–127.

[38] Felix Deku et al. "Amorphous silicon carbide ultramicroelectrode arrays for neural stimulation and recording". In: *Journal of neural engineering* 15.1 (2018), p. 016007.

[39] Alexey Denisov and Eric Yeatman. "Ultrasonic vs. inductive power delivery for miniature biomedical implants". In: *2010 International Conference on Body Sensor Networks*. IEEE. 2010, pp. 84–89.

[40] C A Diaz-Botia et al. "A silicon carbide array for electrocorticography and peripheral nerve recording". In: *Journal of Neural Engineering* 14.5 (2017), p. 056006.

[41] Camilo Andres Diaz-Botia. *Silicon Carbide Technologies for Interfacing with the Nervous System*. University of California, Berkeley, 2017.

[42] PEK Donaldson and E Sayer. "A technology for implantable hermetic packages. Part 1: Design and materials". In: *Medical and Biological Engineering and Computing* 19.4 (1981), p. 398.

[43] Peter EK Donaldson. "The encapsulation of microelectronic devices for long-term surgical implantation". In: *IEEE Transactions on Biomedical Engineering* 4 (1976), pp. 281–285.

[44] George Eisenberg. "Colorimetric determination of hydrogen peroxide". In: *Industrial & Engineering Chemistry Analytical Edition* 15.5 (1943), pp. 327–328.

[45] Dean S Elterman. "The novel Axonics® rechargeable sacral neuromodulation system: Procedural and technical impressions from an initial North American experience". In: *Neurourology and urodynamics* 37.S2 (2018), S1–S8.

[46] Horst Exner and Anne-Maria Nagel. "Laser welding of functional and constructional ceramics for Microelectronics". In: *Laser Applications in Microelectronic and Optoelectronic Manufacturing IV*. Vol. 3618. International Society for Optics and Photonics. 1999, pp. 262–268.

[47] Frank J Fahy. "Vibration of containing structures by sound in the contained fluid". In: *Journal of Sound and Vibration* 10.3 (1969), pp. 490–512.

[48] Kristoffer Famm et al. "Drug discovery: a jump-start for electroceuticals". In: *Nature* 496.7444 (2013), p. 159.

[49] Hui Fang et al. "Ultrathin, transferred layers of thermally grown silicon dioxide as biofluid barriers for biointegrated flexible electronic systems". In: *Proceedings of the National Academy of Sciences* 113.42 (2016), pp. 11682–11687.

[50] MG Fontana and ND Greene. *Corrosion engineering, materials science and engineering*. 1978.

[51] Christopher L Frewin et al. "Silicon Carbide as a Robust Neural Interface". In: *ECS Transactions* 75.12 (2016), p. 39.

[52] Christopher L Frewin et al. "Single-crystal cubic silicon carbide: An in vivo biocompatible semiconductor for brain machine interface devices". In: *2011 Annual International Conference of the IEEE Engineering in Medicine and Biology Society*. IEEE. 2011, pp. 2957–2960.

[53] Kumaravelu Ganesan et al. "An all-diamond, hermetic electrical feedthrough array for a retinal prosthesis". In: *Biomaterials* 35.3 (2014), pp. 908–915.

[54] Jan Gedopt and Erwin Delarbre. "Pulsed Nd: YAG laser welding of titanium ear implants". In: *First International Symposium on Laser Precision Microfabrication*. Vol. 4088. International Society for Optics and Photonics. 2000, pp. 264–267.

[55] Mohammad Meraj Ghanbari et al. "17.5 A 0.8 mm 3 Ultrasonic Implantable Wireless Neural Recording System With Linear AM Backscattering". In: *2019 IEEE International Solid-State Circuits Conference-(ISSCC)*. IEEE. 2019, pp. 284–286.

[56] Jeremy L Gilbert, Christine A Buckley, and Joshua J Jacobs. "In vivo corrosion of modular hip prosthesis components in mixed and similar metal combinations. The effect of crevice, stress, motion, and alloy coupling". In: *Journal of biomedical materials research* 27.12 (1993), pp. 1533–1544.

[57] Emma C Gill et al. "High-density feedthrough technology for hermetic biomedical micropackaging". In: *MRS Online Proceedings Library Archive* 1572 (2013).

[58] Rylie A Green et al. "Integrated electrode and high density feedthrough system for chip-scale implantable devices". In: *Biomaterials* 34.26 (2013), pp. 6109–6118.

[59] Hal Greenhouse. *Hermeticity of electronic packages*. Elsevier, 2000.

[60] Warren M Grill and J Thomas Mortimer. "Neural and connective tissue response to long-term implantation of multiple contact nerve cuff electrodes". In: *Journal of Biomedical Materials Research: An Official Journal of The Society for Biomaterials, The Japanese Society for Biomaterials, and The Australian Society for Biomaterials and the Korean Society for Biomaterials* 50.2 (2000), pp. 215–226.

[61] Thomas Guenther et al. "Practical aspects and limitations of hermeticity testing of micro-encapsulations using cumulative helium leak detection for miniaturized implantable medical devices". In: *IEEE Transactions on Components, Packaging and Manufacturing Technology* (2020).

[62] Thomas Guenther et al. "Pt-Al2O3 interfaces in cofired ceramics for use in miniaturized neuroprosthetic implants". In: *Journal of Biomedical Materials Research Part B: Applied Biomaterials* 102.3 (2014), pp. 500–507.

[63] Mario I Gutierrez et al. "Novel cranial implants of yttria-stabilized zirconia as acoustic windows for ultrasonic brain therapy". In: *Advanced healthcare materials* 6.21 (2017), p. 1700214.

[64] AJ Haemmerli et al. "Ultra-thin atomic layer deposition films for corrosion resistance". In: *2013 Transducers & Eurosensors XXVII: The 17th International Conference on Solid-State Sensors, Actuators and Microsystems (TRANSDUCERS & EUROSENSORS XXVII)*. IEEE. 2013, pp. 1931–1934.

[65] PA Hammond and DRS Cumming. "Encapsulation of a liquid-sensing microchip using SU-8 photoresist". In: *Microelectronic engineering* 73 (2004), pp. 893–897.

[66] J Harris, R Akarapu, and Albert Eliot Segall. "Welding of Alumina Using a Pulsed Dual-Beam CO2 Laser". In: *Journal of manufacturing science and engineering* 133.1 (2011).

[67] Jui-Mei Hsu et al. "Characterization of a-SiCx: H thin films as an encapsulation material for integrated silicon based neural interface devices". In: *Thin solid films* 516.1 (2007), pp. 34–41.

[68] Kazuyoshi Itoh and Yasuyuki Ozeki. "Novel processes in laser microfabrication and microjoining". In: *International Congress on Applications of Lasers & Electro-Optics*. Vol. 2010. 1. LIA. 2010, pp. 1064–1068.

[69] R Jose James et al. "A novel packaging technology for miniaturization of active long-term implantable medical devices enabling new medical applications". In: *2016 6th Electronic System-Integration Technology Conference (ESTC)*. IEEE. 2016, pp. 1–6.

[70] Joonsoo Jeong et al. "Conformal hermetic sealing of wireless microelectronic implantable chiplets by multilayered atomic layer deposition (ALD)". In: *Advanced Functional Materials* 29.5 (2019), p. 1806440.

[71] Guangqiang Jiang and David D Zhou. "Technology advances and challenges in hermetic packaging for implantable medical devices". In: *Implantable Neural Prostheses 2*. Springer, 2009, pp. 27–61.

[72] Guangqiang Jiang et al. "Zirconia to Ti-6Al-4V braze joint for implantable biomedical device". In: *Journal of Biomedical Materials Research Part B: Applied Biomaterials: An Official Journal of The Society for Biomaterials, The Japanese Society for Biomaterials, and The Australian Society for Biomaterials and the Korean Society for Biomaterials* 72.2 (2005), pp. 316–321.

[73] Benjamin C Johnson et al. "StimDust: A 6.5 mm 3, wireless ultrasonic peripheral nerve stimulator with 82% peak chip efficiency". In: *2018 IEEE Custom Integrated Circuits Conference (CICC)*. IEEE. 2018, pp. 1–4.

[74] Alexandra Joshi-Imre et al. "Chronic recording and electrochemical performance of amorphous silicon carbide-coated Utah electrode arrays implanted in rat motor cortex". In: *Journal of neural engineering* 16.4 (2019), p. 046006.

[75] James J Jun et al. "Fully integrated silicon probes for high-density recording of neural activity". In: *Nature* 551.7679 (2017), pp. 232–236.

[76] Michael J Kane et al. "BION microstimulators: A case study in the engineering of an electronic implantable medical device". In: *Medical engineering & physics* 33.1 (2011), pp. 7–16.

[77] Shawn K Kelly et al. "A hermetic wireless subretinal neurostimulator for vision prostheses". In: *IEEE transactions on biomedical engineering* 58.11 (2011), pp. 3197–3205.

[78] Glyn F Kennell and Richard W Evitts. "Crevice corrosion cathodic reactions and crevice scaling laws". In: *Electrochimica Acta* 54.20 (2009), pp. 4696–4703.

[79] Lae Ho Kim et al. "Al2O3/TiO2 nanolaminate thin film encapsulation for organic thin film transistors via plasma-enhanced atomic layer deposition". In: *ACS applied materials & interfaces* 6.9 (2014), pp. 6731–6738.

[80] Gretchen L Knaack et al. "In vivo characterization of amorphous silicon carbide as a biomaterial for chronic neural interfaces". In: *Frontiers in neuroscience* 10 (2016), p. 301.

[81] Takashi DY Kozai et al. "Brain tissue responses to neural implants impact signal sensitivity and intervention strategies". In: *ACS chemical neuroscience* 6.1 (2015), pp. 48–67.

[82] Cary A Kuliasha and Jack W Judy. "In Vitro Reactive-Accelerated-Aging (RAA) Assessment of Tissue-Engineered Electronic Nerve Interfaces (TEENI)". In: *2018 40th Annual International Conference of the IEEE Engineering in Medicine and Biology Society (EMBC)*. IEEE. 2018, pp. 5061–5064.

[83] Michael Langenmair et al. "Low temperature approach for high density electrical feedthroughs for neural implants using maskless fabrication techniques". In: *2018 40th Annual International Conference of the IEEE Engineering in Medicine and Biology Society (EMBC)*. IEEE. 2018, pp. 2933–2936.

[84] Xin Lei et al. "SiC protective coating for photovoltaic retinal prosthesis". In: *Journal of neural engineering* 13.4 (2016), p. 046016.

[85] Tao Li, Roma Y Gianchandani, and Yogesh B Gianchandani. "Micromachined bulk PZT tissue contrast sensor for fine needle aspiration biopsy". In: *Lab on a Chip* 7.2 (2007), pp. 179–185.

[86] Samantha G Lichter et al. "Hermetic diamond capsules for biomedical implants enabled by gold active braze alloys". In: *Biomaterials* 53 (2015), pp. 464–474.

[87] Gustav Lind, Cecilia Eriksson Linsmeier, and Jens Schouenborg. "The density difference between tissue and neural probes is a key factor for glial scarring". In: *Scientific reports* 3 (2013), p. 2942.

[88] Bilong Liu, Yan Jiang, and Daoqing Chang. "Sound transmission of a spherical sound wave through a finite plate". In: *Journal of Sound and Vibration* 410 (2017), pp. 209–216.

[89] Gerald E Loeb et al. "Mechanical loading of rigid intramuscular implants". In: *Biomedical microdevices* 9.6 (2007), pp. 901–910.

[90] NS Lomas and SI Hayek. "Vibration and acoustic radiation of elastically supported rectangular plates". In: *Journal of Sound and Vibration* 52.1 (1977), pp. 1–25.

[91] NH Lovell et al. "A retinal neuroprosthesis design based on simultaneous current injection". In: *2005 3rd IEEE/EMBS Special Topic Conference on Microtechnology in Medicine and Biology*. IEEE. 2005, pp. 98–101.

[92] Roya Maboudian et al. "Advances in silicon carbide science and technology at the micro-and nanoscales". In: *Journal of Vacuum Science & Technology A: Vacuum, Surfaces, and Films* 31.5 (2013), p. 050805.

[93] Gideon Maidanik. "Response of ribbed panels to reverberant acoustic fields". In: *the Journal of the Acoustical Society of America* 34.6 (1962), pp. 809–826.

[94] John M Maloney, Sara A Lipka, and Samuel P Baldwin. "In vivo biostability of CVD silicon oxide and silicon nitride films". In: *MRS Online Proceedings Library Archive* 872 (2005).

[95] Isamu Miyamoto, Kristian Cvecek, and Michael Schmidt. "Crack-free conditions in welding of glass by ultrashort laser pulse". In: *Optics express* 21.12 (2013), pp. 14291–14302.

[96] Isamu Miyamoto et al. "Internal modification of glass by ultrashort laser pulse and its application to microwelding". In: *Applied Physics A* 114.1 (2014), pp. 187–208.

[97] Karen A Moxon et al. "Ceramic-based multisite electrode arrays for chronic single-neuron recording". In: *IEEE Transactions on biomedical engineering* 51.4 (2004), pp. 647–656.

[98] SML Nai et al. "Silicon-to-silicon wafer bonding with gold as intermediate layer". In: *Proceedings of the 5th Electronics Packaging Technology Conference (EPTC 2003).* IEEE. 2003, pp. 119–124.

[99] Khalil Najafi, KD Wise, and Tohru Mochizuki. "A high-yield IC-compatible multichannel recording array". In: *IEEE Transactions on Electron Devices* 32.7 (1985), pp. 1206–1211.

[100] B Arda Ozilgen and Michel M Maharbiz. "Ultrasonic thermal dust: A method to monitor deep tissue temperature profiles". In: *2017 39th Annual International Conference of the IEEE Engineering in Medicine and Biology Society (EMBC).* IEEE. 2017, pp. 865–868.

[101] Kay Palopoli-Trojani et al. "In vitro assessment of long-term reliability of low-cost μECoG arrays". In: *2016 38th Annual International Conference of the IEEE Engineering in Medicine and Biology Society (EMBC).* IEEE. 2016, pp. 4503–4506.

[102] Erin Patrick et al. "Corrosion of tungsten microelectrodes used in neural recording applications". In: *Journal of neuroscience methods* 198.2 (2011), pp. 158–171.

[103] Esteban Peña et al. "Skin erosion over implants in deep brain stimulation patients". In: *Stereotactic and functional neurosurgery* 86.2 (2008), pp. 120–126.

[104] EH Penilla et al. "Ultrafast laser welding of ceramics". In: *Science* 365.6455 (2019), pp. 803–808.

[105] Iago Pereiro et al. "Nip the bubble in the bud: a guide to avoid gas nucleation in microfluidics". In: *Lab on a Chip* 19.14 (2019), pp. 2296–2314.

[106] Hoang-Phuong Phan et al. "Long-Lived, Transferred Crystalline Silicon Carbide Nanomembranes for Implantable Flexible Electronics". In: *ACS nano* 13.10 (2019), pp. 11572–11581.

[107] C Piconi and G Maccauro. "Zirconia as a ceramic biomaterial". In: *Biomaterials* 20.1 (1999), pp. 1–25.

[108] David K Piech et al. "A wireless millimetre-scale implantable neural stimulator with ultrasonically powered bidirectional communication". In: *Nature Biomedical Engineering* 4.2 (2020), pp. 207–222.

[109] Vadim S Polikov, Patrick A Tresco, and William M Reichert. "Response of brain tissue to chronically implanted neural electrodes". In: *Journal of neuroscience methods* 148.1 (2005), pp. 1–18.

[110] Ada SY Poon. "Miniaturized Biomedical Implantable Devices1". In: *Edited by Evgeny Katz* (2014).

[111] Kelsey A Potter et al. "Stab injury and device implantation within the brain results in inversely multiphasic neuroinflammatory and neurodegenerative responses". In: *Journal of neural engineering* 9.4 (2012), p. 046020.

[112] Bogdan C Raducanu et al. "Time multiplexed active neural probe with 1356 parallel recording sites". In: *Sensors* 17.10 (2017), p. 2388.

[113] C Riviere, M Robin, and Gilbert Fantozzi. "Comparison between two techniques in laser welding of ceramics". In: *Le Journal de Physique IV* 4.C4 (1994), pp. C4–135.

[114] Mario Romero-Ortega et al. "Chronic and low charge injection wireless intraneural stimulation in vivo". In: *2015 37th Annual International Conference of the IEEE Engineering in Medicine and Biology Society (EMBC)*. IEEE. 2015, pp. 1013–1016.

[115] E Romero et al. "Neural morphological effects of long-term implantation of the self-sizing spiral cuff nerve electrode". In: *Medical and Biological Engineering and Computing* 39.1 (2001), pp. 90–100.

[116] AG Rouse et al. "A chronic generalized bi-directional brain–machine interface". In: *Journal of neural engineering* 8.3 (2011), p. 036018.

[117] Andrew J Ruys. *Alumina Ceramics: Biomedical and Clinical Applications*. Woodhead Publishing, 2018.

[118] Stephen E Saddow et al. "Single-crystal silicon carbide: A biocompatible and hemocompatible semiconductor for advanced biomedical applications". In: *Materials Science Forum*. Vol. 679. Trans Tech Publ. 2011, pp. 824–830.

[119] Joseph W Salatino et al. "Glial responses to implanted electrodes in the brain". In: *Nature biomedical engineering* 1.11 (2017), pp. 862–877.

[120] ML Santella and JJ Pak. "Brazing titanium-vapor-coated zirconia". In: *WELDING JOURNAL-NEW YORK-* 72 (1993), 165–s.

[121] M Schuettler and T Stieglitz. "Microassembly and micropackaging of implantable systems". In: *Implantable Sensor Systems for Medical Applications*. Elsevier, 2013, pp. 108–149.

[122] Martin Schuettler et al. "A device for vacuum drying, inert gas backfilling and solder sealing of hermetic implant packages". In: *2010 Annual International Conference of the IEEE Engineering in Medicine and Biology*. IEEE. 2010, pp. 1577–1580.

[123] Martin Schuettler et al. "Fabrication and test of a hermetic miniature implant package with 360 electrical feedthroughs". In: *2010 Annual International Conference of the IEEE Engineering in Medicine and Biology*. IEEE. 2010, pp. 1585–1588.

[124] Dongjin Seo et al. "Neural dust: An ultrasonic, low power solution for chronic brain-machine interfaces". In: *arXiv preprint arXiv:1307.2196* (2013).

[125] Dongjin Seo et al. "Wireless recording in the peripheral nervous system with ultrasonic neural dust". In: *Neuron* 91.3 (2016), pp. 529–539.

[126] John P Seymour and Daryl R Kipke. "Neural probe design for reduced tissue encapsulation in CNS". In: *Biomaterials* 28.25 (2007), pp. 3594–3607.

[127] KG Shah et al. *HIGH-DENSITY, BIO-COMPATIBLE, AND HERMETIC ELECTRICAL FEEDTHROUGHS USING EXTRUDED METAL VIAS*. Tech. rep. Lawrence Livermore National Lab.(LLNL), Livermore, CA (United States), 2012.

[128] Mohammad S Siddiqui and W Kinzy Jones. "Vacuum Brazing of Alumina to Titanium for Implantable Feedthroughs Using Pure Gold as the Braze Metal". In: *International Journal of Materials Science and Engineering* 2.1 (2014), pp. 56–62.

[129] J Singh, RA Peck, and GE Loeb. "Development of BION/spl trade/technology for functional electrical stimulation: hermetic packaging". In: *2001 Conference Proceedings of the 23rd Annual International Conference of the IEEE Engineering in Medicine and Biology Society*. Vol. 2. IEEE. 2001, pp. 1313–1316.

[130] Konstantin V Slavin, Hrachya Nersesyan, and Christian Wess. "Peripheral neurostimulation for treatment of intractable occipital neuralgia". In: *Neurosurgery* 58.1 (2006), pp. 112–119.

[131] Enming Song et al. "Thin, transferred layers of silicon dioxide and silicon nitride as water and ion barriers for implantable flexible electronic systems". In: *Advanced Electronic Materials* 3.8 (2017), p. 1700077.

[132] Enming Song et al. "Transferred, ultrathin oxide bilayers as biofluid barriers for flexible electronic implants". In: *Advanced Functional Materials* 28.12 (2018), p. 1702284.

[133] Soner Sonmezoglu and Michel M Maharbiz. "34.4 A 4.5 mm 3 Deep-Tissue Ultrasonic Implantable Luminescence Oxygen Sensor". In: *2020 IEEE International Solid-State Circuits Conference-(ISSCC)*. IEEE. 2020, pp. 454–456.

[134] Melanie EM Stamp et al. "3D Diamond Electrode Array for High-Acuity Stimulation in Neural Tissue". In: *ACS Applied Bio Materials* 3.3 (2020), pp. 1544–1552.

[135] JA Steel and RJM Craik. "Statistical energy analysis of structure-borne sound transmission by finite element methods". In: *Journal of Sound and Vibration* 178.4 (1994), pp. 553–561.

[136] Ian H Stevenson and Konrad P Kording. "How advances in neural recording affect data analysis". In: *Nature neuroscience* 14.2 (2011), p. 139.

[137] Thomas Stieglitz. "Manufacturing, assembling and packaging of miniaturized implants for neural prostheses and brain-machine interfaces". In: *Smart Sensors, Actuators, and MEMS IV*. Vol. 7362. International Society for Optics and Photonics. 2009, p. 73620C.

[138] Thomas Stieglitz. "Manufacturing, assembling and packaging of miniaturized neural implants". In: *Microsystem technologies* 16.5 (2010), pp. 723–734.

[139] Kaylene C Stocking, Alberto L Vazquez, and Takashi DY Kozai. "Intracortical neural stimulation with untethered, ultrasmall carbon fiber electrodes mediated by the photoelectric effect". In: *IEEE Transactions on Biomedical Engineering* 66.8 (2019), pp. 2402–2412.

[140] Timo Stöver and Thomas Lenarz. "Biomaterials in cochlear implants". In: *GMS current topics in otorhinolaryngology, head and neck surgery* 8 (2009).

[141] Matthew G Street, Cristin G Welle, and Pavel A Takmakov. "Automated reactive accelerated aging for rapid in vitro evaluation of neural implant performance". In: *Review of Scientific Instruments* 89.9 (2018), p. 094301.

[142] Felice T Sun and Martha J Morrell. "Closed-loop neurostimulation: the clinical experience". In: *Neurotherapeutics* 11.3 (2014), pp. 553–563.

[143] DH Szarowski et al. "Brain responses to micro-machined silicon devices". In: *Brain research* 983.1-2 (2003), pp. 23–35.

[144] Pavel Takmakov et al. "Rapid evaluation of the durability of cortical neural implants using accelerated aging with reactive oxygen species". In: *Journal of neural engineering* 12.2 (2015), p. 026003.

[145] Kevin J Tracey. "The inflammatory reflex". In: *Nature* 420.6917 (2002), pp. 853–859.

[146] Richard Traeger. "Nonhermeticity of polymeric lid sealants". In: *IEEE Transactions on parts, Hybrids, and packaging* 13.2 (1977), pp. 147–152.

[147] Nahum Travitzky et al. "Additive manufacturing of ceramic-based materials". In: *Advanced Engineering Materials* 16.6 (2014), pp. 729–754.

[148] Rao R Tummala. "Ceramic and glass-ceramic packaging in the 1990s". In: *Journal of the American Ceramic Society* 74.5 (1991), pp. 895–908.

[149] JN Turner et al. "Cerebral astrocyte response to micromachined silicon implants". In: *Experimental neurology* 156.1 (1999), pp. 33–49.

[150] A Vanhoestenberghe and N Donaldson. "Corrosion of silicon integrated circuits and lifetime predictions in implantable electronic devices". In: *Journal of neural engineering* 10.3 (2013), p. 031002.

[151] Anne Vanhoestenberghe and Nick Donaldson. "The limits of hermeticity test methods for micropackages". In: *Artificial organs* 35.3 (2011), pp. 242–244.

[152] A Vanhoestenberghe et al. "Hermetic encapsulation of an implantable vision prosthesis-Combining implant fabrication philosophies". In: *13th International FES Society Conference*. 2008, pp. 187–9.

[153] Jonathan Viventi et al. "Flexible, foldable, actively multiplexed, high-density electrode array for mapping brain activity in vivo". In: *Nature neuroscience* 14.12 (2011), p. 1599.

[154] AS Vlasov and TA Karabanova. "Ceramics and medicine". In: *Glass and ceramics* 50.9-10 (1993), pp. 398–401.

[155] Jeffrey A Von Arx, Scott T Mazar, and Abhi Chavan. *Method and apparatus of acoustic communication for implantable medical device*. US Patent 7,489,967. Feb. 2009.

[156] CE Wallace. "Radiation resistance of a rectangular panel". In: *The Journal of the Acoustical Society of America* 51.3B (1972), pp. 946–952.

[157] Wataru Watanabe, Yan Li, and Kazuyoshi Itoh. "Ultrafast laser micro-processing of transparent material". In: *Optics & Laser Technology* 78 (2016), pp. 52–61.

[158] Wataru Watanabe et al. "Space-selective laser joining of dissimilar transparent materials using femtosecond laser pulses". In: *Applied physics letters* 89.2 (2006), p. 021106.

[159] James D Weiland et al. "Chip-scale packaging for bioelectronic implants". In: *2013 6th International IEEE/EMBS Conference on Neural Engineering (NER)*. IEEE. 2013, pp. 931–936.

[160] Steven M Wellman et al. "Revealing spatial and temporal patterns of cell death, glial proliferation, and blood-brain barrier dysfunction around implanted intracortical neural interfaces". In: *Frontiers in neuroscience* 13 (2019), p. 493.

[161] Reiner Witte, Hans-Joachim Herfurth, and Stefan Heinemann. "Laser joining of glass with silicon". In: *Photon Processing in Microelectronics and Photonics*. Vol. 4637. International Society for Optics and Photonics. 2002, pp. 487–495.

[162] Qiang Wu et al. "Glass frit as a hermetic joining layer in laser based joining of miniature devices". In: *IEEE Transactions on components and packaging technologies* 33.2 (2010), pp. 470–477.

[163] Ni Xiansheng et al. "The use of Taguchi method to optimize the laser welding of sealing neuro-stimulator". In: *Optics and Lasers in Engineering* 49.3 (2011), pp. 297–304.

[164] Pyungwoo Yeon et al. "Automated High-Throughput Hermetic Failure Monitoring System for Millimeter-Sized Wireless Implantable Medical Devices". In: *2019 20th International Conference on Solid-State Sensors, Actuators and Microsystems & Eurosensors XXXIII (TRANSDUCERS & EUROSENSORS XXXIII)*. IEEE. 2019, pp. 2235–2238.

[165] W Yeong et al. "State-of-the-art review on selective laser melting of ceramics". In: *High value manufacturing: advanced research in virtual and rapid prototyping* 1 (2013), pp. 65–70.

[166] Ming Yin et al. "A 100-channel hermetically sealed implantable device for chronic wireless neurosensing applications". In: *IEEE transactions on biomedical circuits and systems* 7.2 (2013), pp. 115–128.

[167] Andy Zhou et al. "A wireless and artefact-free 128-channel neuromodulation device for closed-loop stimulation and recording in non-human primates". In: *Nature biomedical engineering* 3.1 (2019), pp. 15–26.

[168] Felix Zimmermann et al. "Ultrastable bonding of glass with femtosecond laser bursts". In: *Applied Optics* 52.6 (2013), pp. 1149–1154.

Appendix A

MATLAB code for collecting and creating backscatter calibration curves

MATLAB code used in Chapter 3 to construct a calibration curve relating backscatter amplitude to sensed physiological voltage. A high-speed digitizer pulls backscatter waveforms in real time from a SuperTex HV7361DB1 TRX evaluation board while changing the applied input voltage on the modulator. This code was developed for a Keysight 33522A arbitrary waveform generator and an NI-5133 high-speed digitizer, but can be adapted for other devices. The main function **ndCalibCurve** uses the helper function **fn_TemporalAlign** and **fn_crossing**, to align all digitized waveforms. The outputs of this function show the amount of modulation per input voltage (modArray), the average waveform for a given input voltage (waveformAvgCell), and most importantly, the calibration curve slope which can be used for reconstruction. Finally, all raw waveforms are stored in waveformCell.

A.1 ndCalibCurve.m

```
%ND Calibration Curve Generator
%Konlin Shen
%Created: 2/23/18
%Last Updated: 3/27/18

function [modArray, waveformAvgCell, calibslope, waveformCell] = ndCalibCurve
%% Open up communication with waveform generator and digitizer

%waveform generator
hwInfo = instrhwinfo('gpib', 'agilent');
fgenObj = eval(hwInfo.ObjectConstructorName{1});
fopen(fgenObj);
```

```
%digitizer
ictObj = icdevice('niScope.mdd', 'DAQ::Dev1');
connect(ictObj);

%% Set up digitizer properties on Channel 0
%vertical properties
range = 5;
offset = 0;
coupling = 1;
probeAttenuation = 1;

invoke(ictObj.Configurationfunctionsvertical, 'configurevertical',...
    '0', range, offset, coupling, probeAttenuation, true);

%horizontal properties
sampRate = 80e6; %80 Msamples/sec
numPts = 4e3; %collect 4 kB worth of data
refPos = 2;
numRecords = 1; %this records once per fetch?
enforceRealTime = true;

invoke(ictObj.Configurationfunctionshorizontal,...
    'configurehorizontaltiming', sampRate, numPts, refPos,...
    numRecords, enforceRealTime);

%trigger set up
level = 1; %1V level trigger
slope = 1; %positive going edge
holdoff = 0; %HAS TO BE ZERO FOR NI USB 5133
delay = 0; %wait 6.25 us before recording to remove artifact
triggerCoupling = 1; %DC coupling

invoke(ictObj.Configurationfunctionstrigger, 'configuretriggeredge',...
    '1', level, slope, triggerCoupling, holdoff, delay);

%waveform information
waveformInfo.absoluteInitialX = 0;
waveformInfo.relativeInitialX = 0;
waveformInfo.xIncrement = 0;
waveformInfo.actualSamples = 0;
waveformInfo.offset = 0;
waveformInfo.gain = 0;
```

```
waveformInfo.reserved1 = 0;
waveformInfo.reserved2 = 0;

%fetch properties
timeOut = 10;
waveformArray= zeros(1, numPts);
%% Make function generator output DC signal

fprintf(fgenObj, 'SOUR2:APPL:DC DEF, DEF, 0 V');

%% Make filter
order = 255;
% NOTE: number of taps is order + 1;
%NOTE: number of taps must be even, so order must be odd.
%Also: order should be less than length of vector

f_lowerCutoff = 0.3e6;
f_upperCutoff = 4e6;

f_normalized_lower_cutoff = 2.*f_lowerCutoff./sampRate;
f_normalized_upper_cutoff = 2.*f_upperCutoff./sampRate;
firCoefsRawBandPass = fir1(order,...
[f_normalized_lower_cutoff f_normalized_upper_cutoff], 'bandpass');

%% Create loop for cycling through DC values
DCs = 0.303:0.001:0.740;
modArray = [];
numAvg = 100;
window = 1575:1:2300;
for j = 1:length(DCs)
    waveformTemp = zeros(1, 3000);
    dcString = sprintf('SOUR2:APPL:DC DEF, DEF, %f', DCs(j));
    fprintf(fgenObj, dcString);
    for k = 1:numAvg
        invoke(ictObj.Acquisition, 'initiateacquisition');
        [waveformArray, waveformInfo] = invoke(ictObj.Acquisition,...
            'fetch', '0', timeOut,...
            numPts, waveformArray, waveformInfo);
        filteredWF = filtfilt(firCoefsRawBandPass, 1, waveformArray);
        ySampleTemporalBandpassFilter =
            squeeze(filteredWF(1:length(waveformArray)));
        xAligned = fn_TemporalAlign(ySampleTemporalBandpassFilter);
```

```
        xAlignedResample = (1:length(xAligned));
        yTemporalAlignResample=
            spline(xAligned,ySampleTemporalBandpassFilter,xAlignedResample);

        plot(xAlignedResample(1:3000), yTemporalAlignResample(1:3000),...
            'color', rand(1,3));

        waveformCell{j}{k}.waveform = yTemporalAlignResample(1:3000);
        %plot(filteredWF, 'color', rand(1,3));
        waveformTemp = waveformTemp + yTemporalAlignResample(1:3000);
    end
    waveformAvgCell{j}.waveform = waveformTemp/numAvg;
    waveformAvgCell{j}.DC = DCs(j);

    diff = waveformAvgCell{j}.waveform - waveformAvgCell{1}.waveform;
    rectifiedDiff = abs(diff(window));
    integratedMod = cumtrapz(rectifiedDiff);

    waveformAvgCell{j}.mod = integratedMod(end);
    modArray = [modArray, integratedMod(end)];
end

normalizedModArray = modArray/modArray(end);

calibCurve=@(c,v) c*v;
options = optimset('MaxFunEvals',1000000, 'MaxIter', 1000000,...
    'FunValCheck', 'off', 'TolX', 1e-15, 'TolFun', 1.000e-15);

[calibslope,resnorm,residual,exitflag,output]=
    lsqcurvefit(calibCurve,0.5,DCs,normalizedModArray,[],[], options);


figure; plot(DCs, normalizedModArray);
hold on;
plot(DCs, calibCurve(calibslope, DCs), 'r--');
disconnect(ictObj);
fclose(fgenObj);
end
```

A.2 Helper functions

fn_TemporalAlign was written by David Piech. **fn_crossing.m** is publicly available, courtesy of Steffen Brueckner.

A.2.1 fn_TemporalAlign.m

```
function [dataXAligned] = fn_TemporalAlign(inputData)


thresholdRelativeToMax = .05;

%take the length of the vector we input
arraySize = length(inputData);

%make an x axis going from 1 to the length of the input
x = 1:arraySize;

Y = inputData;

% spline interpolation
interpOverSample = 10;
xx = 0.5:(1/interpOverSample):(arraySize+0.5);
yy = spline(x, Y, xx);


% find first crossing at some percentage of the max value
threshold = thresholdRelativeToMax.*max(inputData);
[ind,t0] = fn_crossing(yy, xx, threshold);

if numel(t0) >= 1
    temporalOffset = t0(1);
else
    temporalOffset = 0;
end

dataXAligned = squeeze(x - temporalOffset);
```

A.2.2 fn_crossing.m

```
function [ind,t0,s0,t0close,s0close] = crossing(S,t,level,imeth)
% CROSSING find the crossings of a given level of a signal
```

```
%   ind = CROSSING(S) returns an index vector ind, the signal
%   S crosses zero at ind or at between ind and ind+1
%   [ind,t0] = CROSSING(S,t) additionally returns a time
%   vector t0 of the zero crossings of the signal S. The crossing
%   times are linearly interpolated between the given times t
%   [ind,t0] = CROSSING(S,t,level) returns the crossings of the
%   given level instead of the zero crossings
%   ind = CROSSING(S,[],level) as above but without time interpolation
%   [ind,t0] = CROSSING(S,t,level,par) allows additional parameters
%   par = {'none'|'linear'}.
% With interpolation turned off (par = 'none') this function always
% returns the value left of the zero (the data point thats nearest
%   to the zero AND smaller than the zero crossing).
%
% [ind,t0,s0] = ... also returns the data vector corresponding to
% the t0 values.
%
% [ind,t0,s0,t0close,s0close] additionally returns the data points
% closest to a zero crossing in the arrays t0close and s0close.
%
% This version has been revised incorporating the good and valuable
% bugfixes given by users on Matlabcentral. Special thanks to
% Howard Fishman, Christian Rothleitner, Jonathan Kellogg, and
% Zach Lewis for their input.

% Steffen Brueckner, 2002-09-25
% Steffen Brueckner, 2007-08-27 revised version

% Copyright (c) Steffen Brueckner, 2002-2007
% brueckner@sbrs.net

% check the number of input arguments
%error(nargchk(1,4,nargin));  %  commented out by DKP
%error(narginchk(1,4));
%  modified by DKP to update to newest edition of matlab

% check the time vector input for consistency
if nargin < 2 || isempty(t)
% if no time vector is given, use the index vector as time
    t = 1:length(S);
elseif length(t) ~= length(S)
% if S and t are not of the same length, throw an error
```

```
    error('t and S must be of identical length!');
end

% check the level input
if nargin < 3
% set standard value 0, if level is not given
    level = 0;
end

% check interpolation method input
if nargin < 4
    imeth = 'linear';
end

% make row vectors
t = t(:)';
S = S(:)';

% always search for zeros. So if we want the crossing of
% any other threshold value "level", we subtract it from
% the values and search for zeros.
S   = S - level;

% first look for exact zeros
ind0 = find( S == 0 );

% then look for zero crossings between data points
S1 = S(1:end-1) .* S(2:end);
ind1 = find( S1 < 0 );

% bring exact zeros and "in-between" zeros together
ind = sort([ind0 ind1]);

% and pick the associated time values
t0 = t(ind);
s0 = S(ind);

if strcmp(imeth,'linear')
    % linear interpolation of crossing
    for ii=1:length(t0)
        if abs(S(ind(ii))) > eps(S(ind(ii)))
            % interpolate only when data point is not already zero
```

```
            NUM = (t(ind(ii)+1) - t(ind(ii)));
            DEN = (S(ind(ii)+1) - S(ind(ii)));
            DELTA =  NUM / DEN;
            t0(ii) = t0(ii) - S(ind(ii)) * DELTA;
            % I'm a bad person, so I simply set the value to zero
            % instead of calculating the perfect number ;)
            s0(ii) = 0;
        end
    end
end

% Addition:
% Some people like to get the data points closest to the zero crossing,
% so we return these as well
[CC,II] = min(abs([S(ind-1) ; S(ind) ; S(ind+1)]),[],1);
ind2 = ind + (II-2); %update indices

t0close = t(ind2);
s0close = S(ind2);

%Copyright (c) 2016, Steffen Brueckner
%All rights reserved.
%
%Redistribution and use in source and binary forms, with or without
%modification, are permitted provided that the following conditions are
%met:
%
%    * Redistributions of source code must retain the above copyright
%      notice, this list of conditions and the following disclaimer.
%    * Redistributions in binary form must reproduce the above copyright
%      notice, this list of conditions and the following disclaimer in
%      the documentation and/or other materials provided with the
%      distribution
%
%THIS SOFTWARE IS PROVIDED BY THE COPYRIGHT HOLDERS AND CONTRIBUTORS "AS IS"
%AND ANY EXPRESS OR IMPLIED WARRANTIES, INCLUDING, BUT NOT LIMITED TO, THE
%IMPLIED WARRANTIES OF MERCHANTABILITY AND FITNESS FOR A PARTICULAR PURPOSE
%ARE DISCLAIMED. IN NO EVENT SHALL THE COPYRIGHT OWNER OR CONTRIBUTORS BE
%LIABLE FOR ANY DIRECT, INDIRECT, INCIDENTAL, SPECIAL, EXEMPLARY, OR
%CONSEQUENTIAL DAMAGES (INCLUDING, BUT NOT LIMITED TO, PROCUREMENT OF
%SUBSTITUTE GOODS OR SERVICES; LOSS OF USE, DATA, OR PROFITS; OR BUSINESS
%INTERRUPTION) HOWEVER CAUSED AND ON ANY THEORY OF LIABILITY, WHETHER IN
```

```
%CONTRACT, STRICT LIABILITY, OR TORT (INCLUDING NEGLIGENCE OR OTHERWISE)
%ARISING IN ANY WAY OUT OF THE USE OF THIS SOFTWARE, EVEN IF ADVISED OF THE
%POSSIBILITY OF SUCH DAMAGE.
```

Appendix B

Arduino-based Interrogator Code

This code sequentially turns on four RFID readers, checks for RFID tags, and writes the results to a text file stored on an SD card. The components were as follows:

- Arduino UNO
- Sunfounder RC522 RFID Reader Module
- HiLetgo DS3231 AT24C32 Real Time Clock Module
- WINGONEER MicroSD Card Reader Module

```
 /*
Test bed for simultaneous RFID read and SD card write
No serial monitor (so that pin 0 and pin 1 can be used)
SD card test code from Limor Fried and Tom Igoe
RFID library comes from SunFounder

RFID Pinouts
SDA (SS/CS) -- Pin 10
SCK -- Pin 13
MOSI -- Pin 11
MISO -- Pin 7
IRQ -- Pin 8
GND -- GND
RST -- Pin 9
Vcc -- 3.3V

SD card pinouts
SS/CS -- Pin 4
MOSI -- Pin 11
CLK -- Pin 13
```

```
   MISO -- Pin 12
   GND -- GND

   Konlin Shen
   Date created: 02/05/20
   Last modified: 02/05/20
*/

//include SD card and RFID libraries:
#include <rfid1.h>
#include "SdFat.h"
#include <SPI.h>
#include <RTClib.h>

SdFat SD;

RFID1 rfid;

RTC_DS3231 rtc;

//set up variables using SD utility library functions:

#define SD_CS_PIN SS

//Create file to store the data
File myFile;

//Variable to hold tag UID
uchar serNum[5];
char uid[8];
String filename;

void setup() {

  SPI.begin();

  Serial.print("\nInitializing SD card...");

  if (!SD.begin(SD_CS_PIN)) {
    return;
  }
  Serial.println("initialization done.");
```

```
  if(!rtc.begin()){
    while(1);
  }
  else{
    rtc.adjust(DateTime(F(__DATE__), F(__TIME__)));
  }
  if(!rtc.lostPower()){
  }

  DateTime now = rtc.now();
  String prefix=String(now.year())+String(now.month())+String(now.day());
  filename = prefix + ".txt";

  int iterator = 1;

  while(SD.exists(filename.c_str())){
    filename = prefix + "-" + String(iterator) + ".txt";
    iterator = iterator + 1;
  }

  pinMode(14, OUTPUT);
  pinMode(15, OUTPUT);
  pinMode(16, OUTPUT);
  pinMode(17, OUTPUT);

  digitalWrite(14, LOW);
  digitalWrite(15, LOW);
  digitalWrite(16, LOW);
  digitalWrite(17, LOW);
}

void loop() {
  uchar status;
  uchar str[MAX_LEN];

  myFile = SD.open(filename, FILE_WRITE);

  if (myFile) {
     DateTime now = rtc.now();
     myFile.print(now.year(), DEC);
     myFile.print('/');
```

```
    myFile.print(now.month(), DEC);
    myFile.print('/');
    myFile.print(now.day(), DEC);
    myFile.print(' ');
    myFile.print(now.hour(), DEC);
    myFile.print(':');
    myFile.print(now.minute(), DEC);
    myFile.print('\t');

    myFile.close();
  }

  for (int i = 0; i < 4; i++){
    if (i == 0){
      rfid.begin(8, 6, 2, 7, 4, 9);
    }
    if (i == 1){
      rfid.begin(8, 6, 2, 3, 4, 9);
    }
    if (i == 2){
      rfid.begin(8, 6, 2, 5, 4, 9);
    }
    if (i == 3){
      rfid.begin(8, 6, 2, 0, 4, 9);
    }
    //rfid.begin(IRQ_PIN,SCK_PIN,MOSI_PIN,MISO_PIN,NSS_PIN,RST_PIN)
    delay(1000);
    rfid.init();

    status = rfid.request(PICC_REQIDL, str);
    if (status != MI_OK)
    {
       if (i == 0){
         digitalWrite(16, LOW);
       }
       if (i == 1){
         digitalWrite(17, LOW);
       }
       if(i == 2){
          digitalWrite(15, LOW);
       }
       if (i == 3){
```

```
        digitalWrite(14, LOW);
      }

      myFile = SD.open(filename, FILE_WRITE);

      if (myFile) {
       Serial.println("File opened ok");
       Serial.println("Writing to card");

       myFile.print("No card found");

       if (i != 3){
         myFile.print(", ");
       }
       else{
         myFile.print("\n");
       }
       myFile.close();
     }
     else {
     }
  }
  status = rfid.anticoll(str);

  if (status == MI_OK)
  {
     if (i == 0){
       digitalWrite(16, HIGH);
     }
     if (i == 1){
       digitalWrite(17, HIGH);
     }
     if (i == 2){
       digitalWrite(15, HIGH);
     }
     if (i == 3){
       digitalWrite(14, HIGH);
     }
     memcpy(serNum, str, 5);

     myFile = SD.open(filename, FILE_WRITE);
```

```
        if (myFile) {
         for(int j = 0; j < 4; j++){
           myFile.print(0x0F & (serNum[j]>>4), HEX);
           myFile.print(0x0F & serNum[j], HEX);
         }

         if (i != 3){
           myFile.print(", ");
         }
         else {
           myFile.print("\n");
         }
         myFile.close();
       }
       else {
       }
     }
     delay(3000);
   }
   delay(1000);
}
```